

University of St Andrews



Full metadata for this thesis is available in
St Andrews Research Repository
at:

<http://research-repository.st-andrews.ac.uk/>

This thesis is protected by original copyright

Three-dimensional Equilibrium Solutions to the Magnetohydrodynamic Equations and their Application to Solar Coronal Structures

Gordon James Duncan Petrie



Thesis submitted for the degree of Doctor of Philosophy
of the University of St Andrews

September 11, 2000



TL

D684

Declaration

1. I, Gordon James Duncan Petrie, hereby certify that this thesis, which is approximately 45,000 words in length, has been written by me, that it is a record of work carried out by me and that it has not been submitted in any previous application for a higher degree.

date ...11th...September...2000... signature of candidate

2. I was admitted as a research student in October 1997 and as a candidate for the degree of PhD in October 1998; the higher study for which this is a record was carried out in the University of St Andrews between 1997 and 2000.

date ...11th...September...2000... signature of candidate .

3. I hereby certify that the candidate has fulfilled the conditions of the Resolution and Regulations appropriate to the degree of PhD in the University of St Andrews and that the candidate is qualified to submit the thesis in application for that degree.

date ...11/9/2000... signature of supervisor

4. In submitting this thesis to the University of St Andrews I understand that I am giving permission for it to be made available for use in accordance with the regulations of the University Library for the time being in force, subject to any copyright vested in the work not being affected thereby. I also understand that the title and abstract will be published and that a copy of the work may be made and supplied to any bona fide library or research worker.

date ...11th...September...2000... signature of candidate .

Abstract

We present in this thesis three-dimensional self-consistent solutions of the MHD equations which we then apply in giving simple models of magnetic structures in the solar atmosphere. Two classes of solution are presented.

One class, steady-state equilibria with field-aligned incompressible flow, is calculated for the first time. These solutions are calculated by a transformation method which allows the construction of steady state MHD solutions with subalfvénic flow from known solutions of static MHD and of steady state MHD solutions with superalfvénic flow from known solutions of steady state hydrodynamics. For the first time this transformation method is applied to three-dimensional solutions of the steady state MHD equations. We discuss possible applications of particular solutions to flow phenomena in the solar atmosphere such as the Evershed flow in sunspots and flows in coronal arcades.

For the second class of solutions, a special class of linear self-consistent three-dimensional solutions of the magnetohydrostatic (MHS) equations for which the current density is a combination of a linear force-free part and a part with non-force-free components, we succeed in deriving a Green's function method. This allows the construction of MHS solutions of this class with arbitrary photospheric boundary conditions for B_z . These solutions can be used to extrapolate coronal magnetic fields from known longitudinal photospheric field data and provide a self-consistent description of magnetic field, plasma pressure, plasma density and plasma temperature. The method therefore allows a better comparison of models with observations of solar coronal structures. We will demonstrate how the method works by giving an illustrative example.

We continue this work by applying the Green's function method to several sets of observed line-of-sight photospheric magnetic field data and thereby calculating self-consistent plasma structures in the solar atmosphere. As far as possible we compare these calculated structures to near-simultaneous emission patterns.

We conclude the thesis with a discussion recapping some strengths and weaknesses of the solutions and exploring some possibilities for extending the work.

Acknowledgements

“If you can keep your head while everybody around you is losing theirs then clearly you haven’t grasped the situation.” Gordon Smith on *Sportscene* discussing Ebbe Skovdahl.

It is a pleasure for me to thank

- Dr. Thomas Neukirch for his unfailing and inspirational supervision,
- the Solar Theory Group at St Andrews for taking me as a research student in the first place and for providing a stimulating environment to work in,
- Prof. Alan Hood for discussions relating to Chapter 2,
- Drs. Daniel Brown and Duncan Mackay for giving me access to data used in Chapter 4,
- PPARC for financial support.

Finally I would like to thank my family for their love and support.

Contents

1	Introduction	4
1.1	The Solar Atmosphere	5
1.2	Magnetic Structures	6
1.3	The MHD Approximation	16
1.4	The MHD Equations	18
1.5	The Magnetohydrostatic and Steady MHD Approximations	22
1.5.1	Magnetohydrostatics	23
1.5.2	Steady MHD	24
1.6	MHS and Steady MHD Equilibria: The General Picture and this Thesis	25
1.7	Outline of Thesis	29
2	Self-consistent steady state solutions with field-aligned incompressible flow	31
2.1	Introduction	31
2.2	Euler Potentials	35
2.3	Transformation Method	37
2.4	Non-symmetric Static MHD Solutions	42
2.4.1	Solutions in Cartesian Coordinates	42

2.4.2	Solutions in Cylindrical Coordinates	44
2.5	Non-symmetric solutions with steady flow	46
2.5.1	Background	46
2.5.2	Solutions in Cartesian coordinates	50
2.5.3	Solutions in cylindrical coordinates	60
2.6	Discussion and Conclusion	68
3	The Green's Function Method for a Special Class of Linear 3D Static Equilibria	71
3.1	Introduction	71
3.2	The Solution Class	76
3.3	Introduction to Green's Functions	81
3.4	Green's Function Method	83
3.5	Special Cases	87
3.5.1	Force-Free Case	87
3.5.2	Case $\xi(z) = \text{constant}$	88
3.5.3	Case $\xi(z) = ae^{-\kappa z}$	89
3.6	Discussion	91
4	Magneto-hydrostatic Green's Function Method: Applications	94
4.1	Introduction	94
4.2	Illustrative Example: $\xi(z) = \text{constant}$	96
4.3	Applying the Method to Observational Data	109
4.4	Observations	111
4.5	Green's Function Method Application: Solar Coronal Bright Point	112

4.6	Magnetohydrostatic Green's Function Method Application: Formation of a Solar Coronal Filament	123
4.6.1	Introduction	123
4.6.2	Model for July 22 1979	127
4.6.3	Model for July 25 1979	131
4.6.4	Discussion	136
4.7	Green's Function Method Application: Sigmoid-like Structure	137
4.8	Intense flux tube	146
4.9	Discussion	151
5	Conclusion	153
A	Extensions to the Transformation Method	156
A.1	Transforming from static 3D MHD without gravity to 3D MHD with steady field-aligned incompressible flow and gravity	156
A.2	Transforming from static 3D MHD with gravity to 3D MHD with steady incompressible field-aligned flow and gravity	157
B	Textbook Green's Function Method for the Linear Force-free Case	159

Chapter 1

Introduction

The Sun affects us on the Earth more than any other astronomical object. It is also believed to have the same basic physical structure and properties as any other ordinary star. Stars are basic inhabitants of the wider universe and their properties have always been a major topic of astronomical research. Solar research is then motivated both by the Sun's overwhelming influence on the Earth and by curiosity surrounding stars in general.

Solar research has in recent years been boosted by a series of advances in solar observational astronomy. The work at ground-based solar observatories has been reinforced by the introduction of instruments operating from satellites such as Skylab, Yohkoh, SoHO and TRACE offering data at higher spatial and temporal resolution than previously possible, and with fewer interruptions. The resulting proliferation of images of the solar atmosphere has left theorists with much to explain. In particular the highly structured and dynamic nature of the solar atmosphere has proved to be difficult to model. The present thesis aims to contribute to the effort to do this.

This century it has gradually become apparent that much of the structure observed on the solar surface is caused by the sun's magnetic field. Magnetohydrodynamics (MHD) describes the macroscopic behaviour of electrically conducting fluids and of plasmas in particular. The intention behind this work is to derive new solutions to the MHD equations and to apply them to modelling in a simple manner certain complex structures on the solar surface caused by interaction between the solar plasma and

magnetic field.

This work does not directly treat time-dependent dynamics, but magnetohydrostatic (MHS) and steady-state MHD equilibria. This approach can be justified not only by the necessity of such assumptions for making analytical progress, but also by the fact that solar atmosphere plasma motion is dominated by the magnetic field to the extent that plasma is often confined by strong magnetic fields for times which are long compared to typical flow decay times so that dynamical effects are weak, giving rise to quasi-static magnetic field configurations (see Section 1.5).

Analytical work in MHD has in the past enjoyed much success in modelling the extremely complicated physical processes on the Sun such as magnetic reconnection, MHD waves and coronal loops. In analytical work it is often necessary to make some quite drastic physical assumptions to make a problem tractable. While we may assume some special form for a solution to simplify our task we are not suggesting that nature would ever choose such a configuration. If the physical essence of an event or a feature is captured in a simple solution then powerful results giving insight into the more complicated observed system may be obtained.

We begin by introducing the solar atmosphere and describing some of its simple properties in Section 1.1 and by introducing some of its features in Section 1.2. We give a justification for describing the solar atmosphere with MHD in Section 1.3, before in Section 1.4 giving the MHD equations. We follow this in Section 1.5 with a brief introduction to MHS and steady MHD, and in Section 1.6 with a discussion of the MHD equilibria already known to us and where our work fits in among them. We complete the introduction by outlining the rest of the thesis.

1.1 The Solar Atmosphere

While the solar atmosphere is complicated by a great variety of three-dimensional structure which motivates this thesis, it has an underlying one-dimensional structure consisting of three regions, each characterised by distinctive physical properties: the photosphere, the chromosphere and the corona. The lowest layer in altitude is an

extremely thin layer of plasma called the photosphere which is opaque and dense and emits most of the solar radiation. This is the visible surface of the Sun that we are most familiar with. It is not a solid surface but is much denser than the atmosphere above. In our simple models of the solar atmosphere we will treat the photosphere as the lower boundary. Above it lies the less dense and more transparent irregular layer called the chromosphere. This is named after the Greek word “chromos” for colour because of its reddish $H\alpha$ emission. Next is the transition region which separates the corona from the much cooler chromosphere. Heat flows down from the corona into the chromosphere producing this thin region where the temperature changes rapidly. Above this the corona extends from the top of a narrow transition region. The corona is the Sun’s outer atmosphere.

The depth of the photosphere is 500km and the height of the transition region from the chromosphere to the corona is 2 - 10Mm. The density at the photosphere is $10^{23}m^{-3}$, in the transition region $10^{15}m^{-3}$, in the lower corona $5 \times 10^{14}m^{-3}$ and at 1AU, 10^7m^{-3} . Unlike the density which decreases rapidly with height above the solar surface, the temperature, after falling from about 6600K at the bottom of the photosphere to a minimum value of about 4300K at the top of the photosphere, rises slowly through the lower chromosphere from about 6000K to about 2×10^4K , and then dramatically through the transition region to a few million degrees in the corona. Thereafter the temperature falls slowly in the outer corona, which is expanding outwards as the solar wind, to a value of 10^5K at 1AU.

1.2 Magnetic Structures

Any emission image of the solar atmosphere shows that its overall one-dimensional structure is greatly distorted by a variety of three-dimensional features. Figure 1.1 is a typical image of the solar corona showing its highly structured nature. This three-dimensionality as well as some dynamical properties of the structures are of central relevance to our thesis. The following magnetic features are to a greater or lesser extent considered in this thesis and are introduced in this section: coronal loops, sunspots, X-ray bright points, prominences and sigmoids.

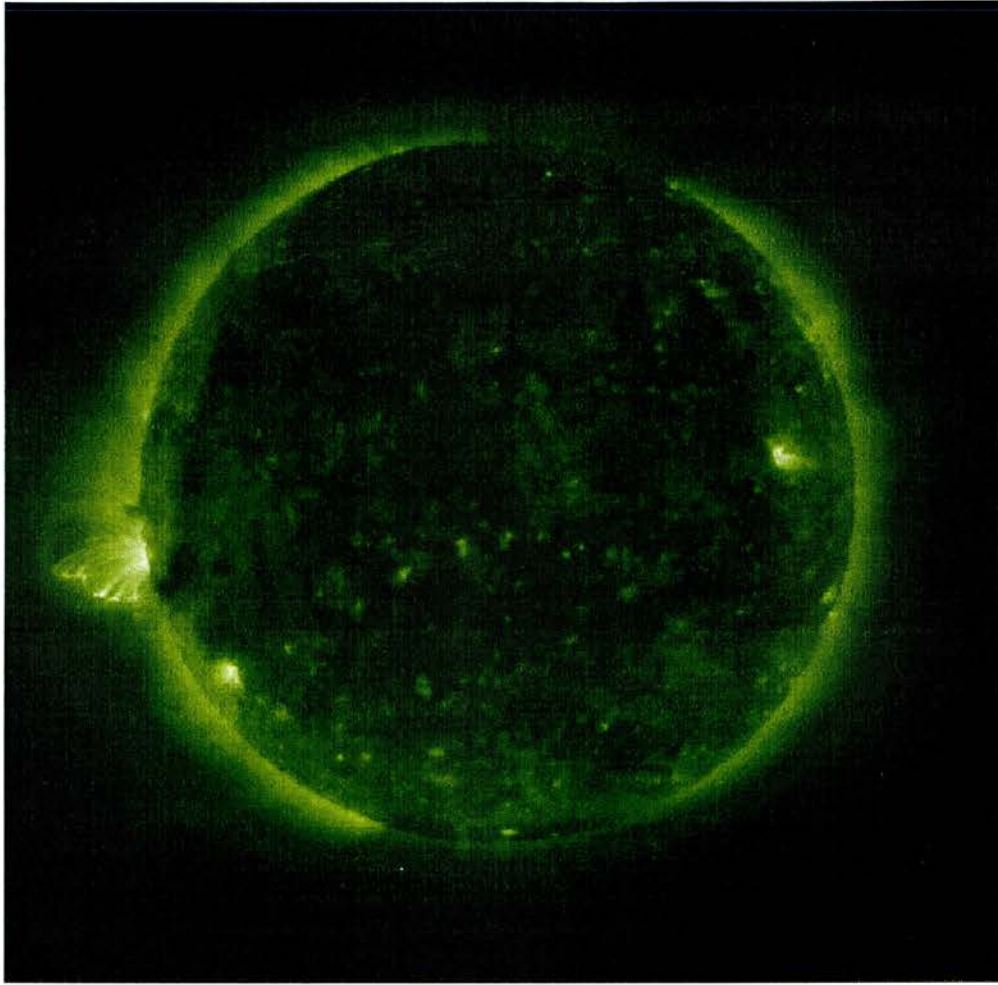


Figure 1.1: An image of the solar corona from the EIT instrument on the SoHO satellite. The three-dimensional structure of the solar atmosphere is clearly illustrated by this image.

Although highly complicated and varied small-scale structure is observed, most active regions are simpler on large scales with the flux well organised into islands of opposite polarity, but occasionally a magnetically complex region forms as new flux emerges with a different orientation or as a new region appears within an existing one.

A significant part of the energy emission from the solar corona is concentrated along well-defined curved paths called loops. An example of a coronal loop is shown in Figure 1.2, left. Coronal loops are a feature of active regions and it is believed that they spread themselves out to dominate the lower corona, particularly in and over active regions.

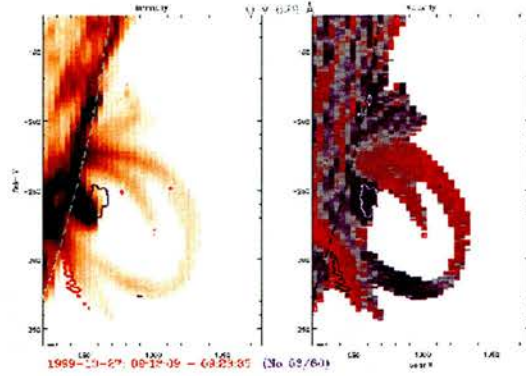


Figure 1.2: A coronal loop system (left) with three-dimensional structure visible. Also shown is the velocity field structure (right) indicated by red and blue Doppler shifts. The plasma flow could be interpreted to be unidirectional and field-aligned.

The footpoints of loops are found to be located on sunspots (see later) or on a single sunspot and an area of opposite magnetic polarity. The loops are believed to trace out closed lines of force of the magnetic field which protrude up from beneath the photosphere and expand to fill the whole of the coronal volume above an active region. Hence a picture of a loop system gives us some insight into the three-dimensional structure of the magnetic field. Observations (see Bray et al., 1991) show that coronal loops, depending on their temperature, can be divided into two distinct categories, the properties of the two types differing radically. Loops of temperature more than about 10^6K are called hot loops while the rest are called cool loops. The range of temperature of the “cool loops” category is about 10^6K down to about 2^4K . With the exception of temperature all loops seem to have similar properties and are regarded as manifestations of the same physical phenomena. However, hot loops are thicker, longer, higher and longer-lived than cool loops. Hot and cool loops are not co-spatial although they may lie close together. Hot EUV emission is confined largely to active regions and to active region loops. The enhanced EUV emission of a loop indicates that its density is higher than that of its surroundings. Unlike the cool loops where $\text{H}\alpha$ observations have been available for many years, very little data on the dynamics of hot loops has been obtained. For cool loops it has been known for a long time that three types of motion are possible: a flow down both legs starting at the apex of the loop, a flow up one leg and down the other, and a mainly horizontal “back-and-forth”

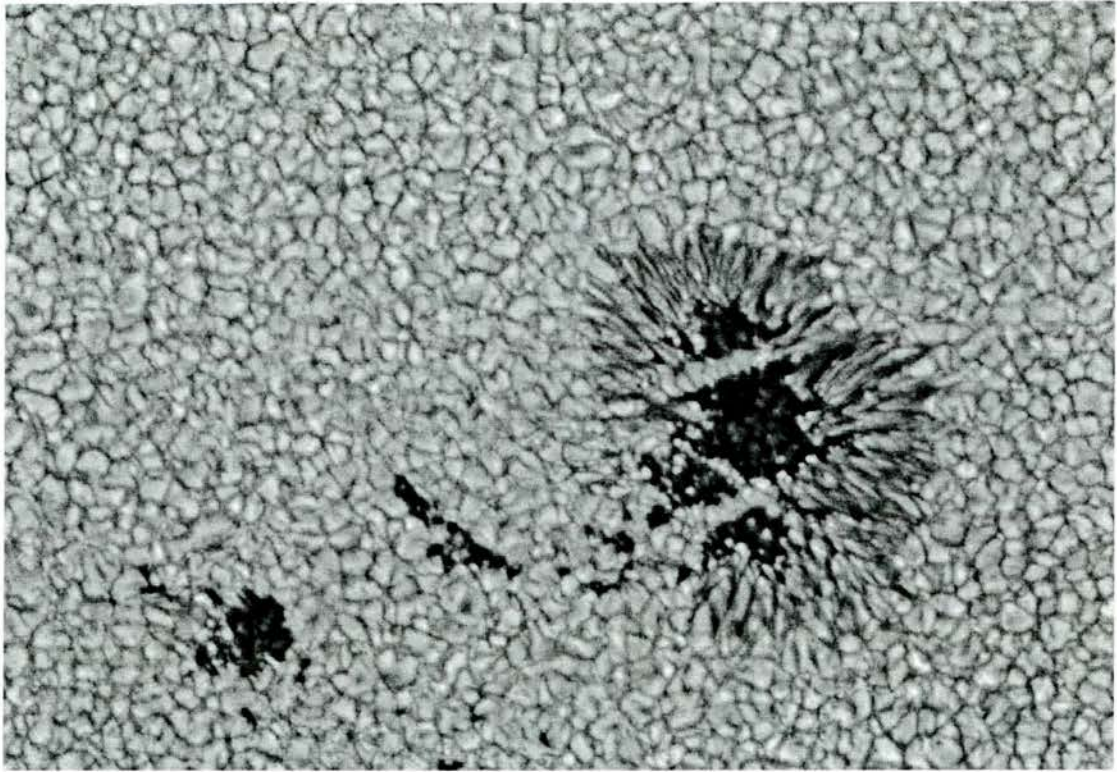


Figure 1.3: A sunspot with umbra (dark central region) and penumbra (dark and bright streaked surrounding region) visible.

motion of the whole loop oscillation. The majority of observed velocities lie in the range 20 - 150km/s. It has been remarked that flows in the unidirectional category are a commonly-observed characteristic of new and complex active regions. The right panel of Figure 1.2 can be interpreted as showing evidence of unidirectional flow in the loop of the left panel, although a downward flow from the apex down both legs is also possible. The motion along a loop may continue for up to several hours. This is roughly the same interval over which loop systems are said to last. The motions in a loop may be strongly supersonic with non-gravitational forces acting on the loop material. The pressure and temperature in the core of a loop are always lower than the surrounding sheath but they can be either higher or lower than the ambient coronal values. The most prominent active region loops are about 10^5 km long and 10^4 km wide and have cool cores with temperature about 2×10^5 K.

In the photosphere the most intense concentrations of magnetic flux appear as sunspots

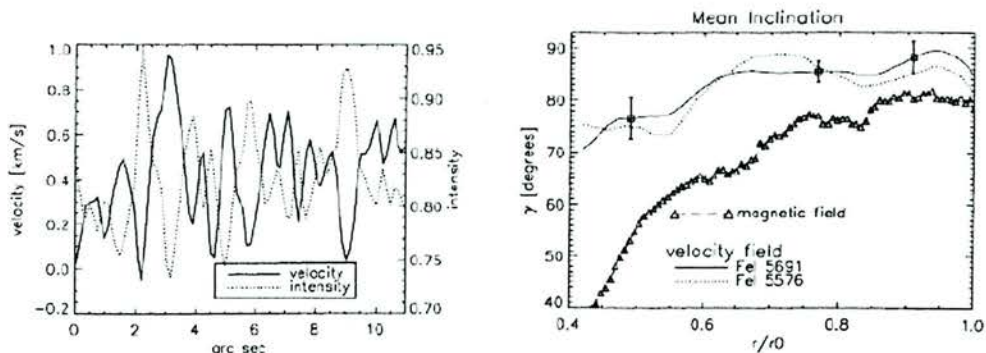


Figure 1.4: Left: velocity (solid line) and intensity (dotted line) measured across the dark and bright fibrils of a sunspot penumbra. This graph indicates a strong correlation between the penumbral (Evershed) flow and the dark fibrils. Right: mean inclination of the magnetic field and velocity field vectors with radius. Pictures from Rimmele (1995a).

(see Figure 1.3). They are formed by the emergence of flux and decay away with the slow dispersal of an active region, but the region may remain active for weeks or months after the spot has disappeared. The long, thin, dark streaks of Figure 1.3 are called fibrils and probably follow magnetic field lines. Individual fibrils have width 700 – 2200km, arc length 11000km and lifetimes of 10 – 20 minutes, although their overall pattern remains constant for hours.

Sunspots develop from pores, which are darker than their surroundings and have no penumbra (see below). They have diameters of about 700 – 4000km, about 50% of photospheric brightness and field strengths in excess of 1500G. Often they only last for hours or days but sometimes one develops into a small sunspot. The sunspot grows over 3 – 10 days as more flux is added to it by moving magnetic features the same polarity as the sunspot, apparent in white light as pores. Spots are typically formed in pairs, one of each polarity. Most spots disappear a few days after forming but some large ones last much longer, slowly decaying over a few months.

The central dark area is called the umbra, which has a diameter of $10^4 - 2 \times 10^4$ km, or about 40% of the spot diameter. In the umbra the magnetic field strength and the temperature are fairly uniform and the intensity in visible light is 5 – 15% of the

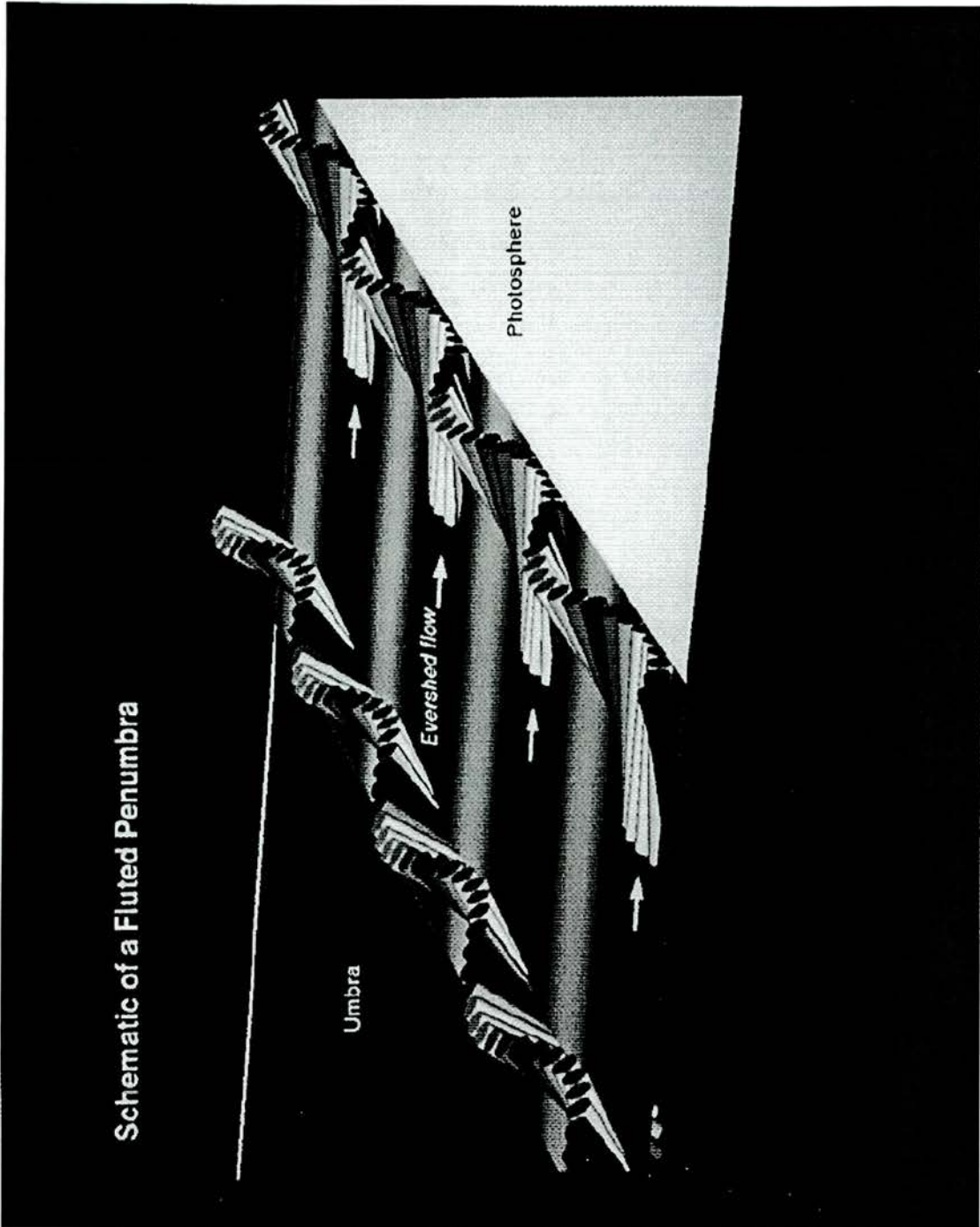


Figure 1.5: Schematic representation of a fluted penumbra. Sets of field lines near the inner and outer penumbral boundaries are represented by cylinders. Their red and blue colours indicate current flow towards and away from the umbra respectively. The bright and dark stripes indicate the bright and dark penumbral fibrils. The arrows indicate the location of the Evershed flow. Picture from Title et al. (1993).

photospheric intensity. The magnetic field in the centre of the umbra is vertical with magnetic field strength of about 2000 – 3000G or possibly even 4000G, decreasing gradually to 1000 – 1500G near the penumbral boundary.

The umbra is surrounded by the penumbra, which consists of black and white radial fibrils that are 5000 – 7000km long and 300 – 400km in width. Individual fibrils last 30 minutes to 6 hours compared to days or months for the spot as a whole. The intensity of a bright fibril is 95% of the photospheric brightness while the dark fibril intensity is 60%. Measurements of the transverse field imply that magnetic field lines fan out as one moves out from the spot, the lines becoming more inclined with respect to the vertical (see Figure 1.4, right). Nearly all magnetic flux from the spot probably returns to the photosphere through many small magnetic features located at supergranule boundaries.

At the beginning of the century Evershed (1909) discovered radial motions on the photosphere, outwards from the penumbra. In well-established spots the flow is continuous with flow speeds of 6 – 7km/s along the dark penumbral fibrils, comparable with the sound speed but less than the local Alfvén speed. The radial outflow appears to reach a maximum near the outer boundary of the penumbra. The possible existence of vertical and azimuthal components is controversial. Higher up in the atmosphere the Evershed flow becomes slower and eventually reverses its direction at chromospheric levels. The Evershed flow also extends over a fairly large region surrounding the sunspot - it is observed along superpenumbral fibrils, which are loops about 5×10^4 km high, with flow speeds of about 20km/s or as high as 50km/s.

It is the three-dimensional structure of the penumbra that is of particular interest to us in this thesis. Recent high-resolution observations of sunspots indicate that the penumbral magnetic field is not rotationally symmetric but is highly fluted. The magnetic field in the dark fibrils is close to horizontal while the field in the bright fibrils is more inclined from the photosphere. The Evershed flow is intimately related to the fluted magnetic field structure. The bright fibrils are correlated to the more steeply-rising field lines restricting the Evershed flow to the dark fibrils as illustrated by Figure 1.4 (left). Figure 1.4 (right) shows the near-horizontal nature of the flow compared to the average magnetic field line inclination. A graphical illustration of the situation is given in Figure 1.5. More details of the penumbral magnetic and velocity

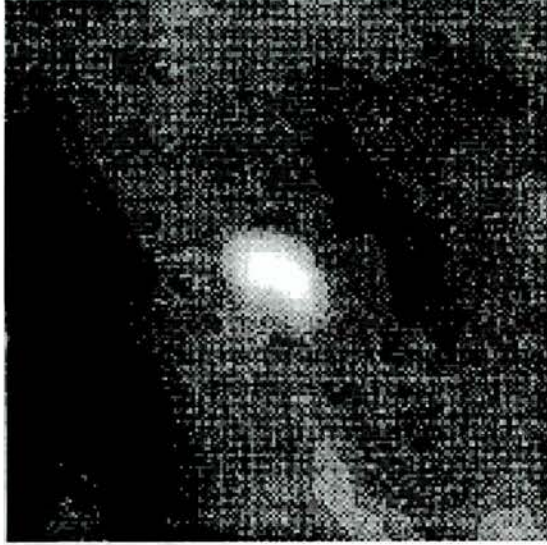


Figure 1.6: A solar coronal X-ray bright point.

field structure are given Section 2.5.1.

In siphon models of plasma flow the flow is assumed to continue through the chromosphere and photosphere and into the subsurface regions where it is maintained. It has been suggested that the mechanism responsible for Evershed flows is a siphon flow maintained by a pressure difference between the footpoints. This model has also been developed for loops. While loops with flow are certainly observed, little work has been done on modelling loops which are not isolated. When a model loop is perfectly symmetric the governing equations are symmetric but, surprisingly, models of steady subsonic flows antisymmetric about the apex of a loop are possible without any pressure difference between the footpoints of the loop (this will also be true for our loop-like solutions in Chapter 2).

Coronal X-ray bright points have average diameter around 2×10^5 km and bright cores of 4000km to 7000km. Their activity in the corona is related to small bipolar areas of emerging flux and they appear to consist of several loops about 12000km long and 2500km wide. Bright points are associated with much of the magnetic flux emerging through the solar surface. An example of a bright point is shown in Figure 1.6.

A filament is a cool, dense structure suspended above the solar surface by loops of magnetic field and observed as dark in $H\alpha$. Example of filaments are shown in Figure

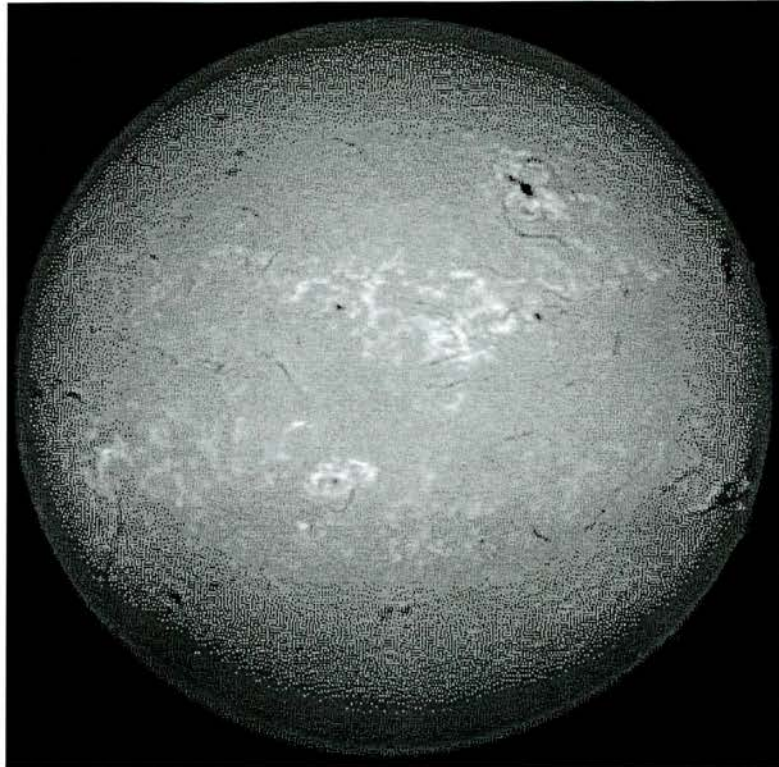


Figure 1.7: Example of filaments are visible in absorption in this full-disk $H\alpha$ image as dark structures against the bright emission of the photosphere.

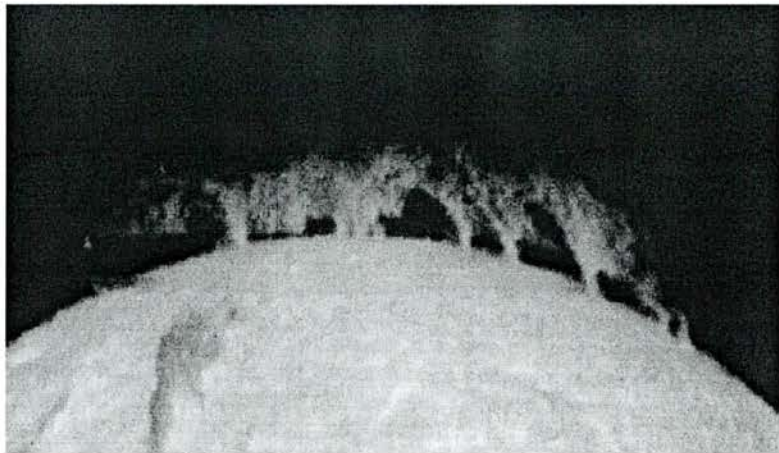


Figure 1.8: An example of a prominence. A prominence is a filament (see Figure 1.7) observed at the limb of the Sun.

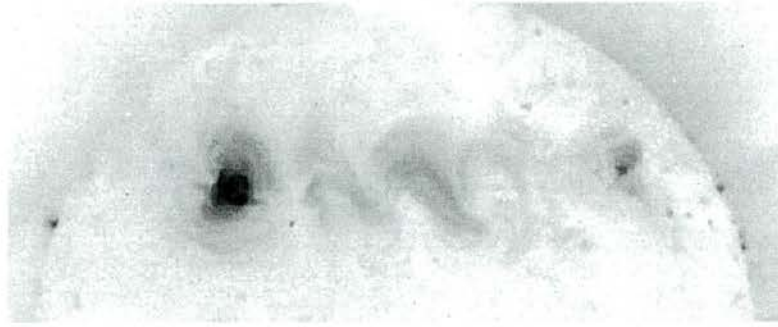


Figure 1.9: Two sigmoid structures with their distinctive S-shape.

1.7. The formation of a filament takes a few hours or a day and occurs either between two neighbouring active regions, at the boundary of an active region or in a remnant region but always at a polarity inversion line. Prominences are located in the corona but have temperatures about a hundred times lower and density about a hundred to a thousand times greater than coronal values. In eclipse or coronagraph pictures they appear bright at the limb but in $H\alpha$ photographs of the disc they appear as long and dark filaments. Prominences and filaments are the same thing except that prominences are seen projecting out above the limb of the Sun. An example of a prominence is shown in Figure 1.8. There are two basic types of prominence: quiescent and active. While an active prominence is a short-lived and violent structure lasting only minutes or hours and often associated with a flare, a quiescent prominence is a very stable structure which may last for many months. It is a huge almost-vertical sheet of dense, cool plasma standing in the hotter rarer coronal plasma. Its density ranges between 10^{16}m^{-3} and 10^{17}m^{-3} , its temperature between 5000K and 8000K with dimensions as follows: length $6 \times 10^4 - 6 \times 10^5\text{km}$, height 15000 - 10^5km and thickness 4000 - 15000km. A sigmoid is a large bright S-shaped (or anti-S-shaped) X-ray structure which has recently been used by observers as a predictor of eruptions. The specimen studied in this thesis is about 200Mm across. The density and temperature profiles of a sigmoid have not yet been determined. In Figure 1.9, two sigmoid structures are clearly visible - they are the middle and right structures of the group of three in the middle of the picture.

We have introduced only a few of the many magnetic features observed in the solar

atmosphere, specifically the features we intend to model. Although physical conditions associated with each of the features may vary widely, the structuring of the solar atmosphere in many of its forms may be described by a single set of equations as will be seen in the next section.

1.3 The MHD Approximation

We aim to model the structures of the last section by describing the interaction of the plasma and the magnetic field. Many descriptions of this process are available, offering different compromises between physical sophistication and practical simplicity, from a full N-body problem to single fluid MHD. For a detailed discussion of some of the levels of description and the relationship between them see e.g. Balescu (1988). Here we give a justification for our choice of using MHD.

The usual condition for a fluid description is that the mean free path λ_c is short compared to typical length scales $\lambda_c |\nabla f| \ll f$ for physical quantities f . While this is usually satisfied for liquids and neutral gases the mean free path in hot plasmas becomes very long, $\lambda_c \propto T^2$ where T is the temperature, so that formally the condition for a fluid approximation may easily be violated. Fortunately, the formal argument is misleading.

At the high temperatures and low densities characteristic of the corona the atoms of the coronal gas are almost all ionised. The long-range electrostatic forces between the charges then dominates the small-scale motion of the particles. Any medium (not necessarily a fluid) in which this is the case is called a plasma. It is a basic property of plasmas that the scale of electrostatic interaction usually prevents any large-scale separation of opposite charges. The average charge density is effectively zero everywhere so that the large-scale dynamics of the plasma are controlled by the magnetic field.

In a uniform field a single charged particle moves helically along a field line. The radius of the circular projection of the path is called the Larmor radius, given by the equation

$$r_L = \frac{vm}{ZeB} \tag{1.1}$$

while the frequency of revolution is called the Larmor frequency or gyrofrequency, given by

$$\Omega = \frac{ZeB}{m} \quad (1.2)$$

where v is the speed of the particle in the plane of the circle and B and Ze are its mass and charge respectively (the quantity e is the charge of an electron). The motion in the direction of the field, i.e. along the field line, is uninfluenced by the field - the particle drifts freely. If other particles are present the drift continues until a collision - a near-encounter with another particle - scatters the particle from its helical path. These collisions are called Coulomb collisions and occur in a fully ionised plasma at a frequency

$$\nu_c \approx 1.3 \times 10^{-20} \frac{n}{m^{1/2} T^{3/2}} \quad (1.3)$$

where n is the particle number density and T is the temperature of the system. The distance drifted between collisions is the mean free path

$$\lambda_c = \frac{v_{th}}{\nu_c} \quad (1.4)$$

where $v_{th} = \sqrt{\frac{k_B T}{m}}$ is the typical thermal speed of the particles and k_B is Boltzmann's constant.

If we take approximate coronal values $T = 2.0 \times 10^6 \text{K}$, $|\mathbf{B}| = 1 \text{mT}$, then $r_L \approx 1 \text{m}$ for ions and 20mm for electrons with gyrofrequencies 10^5rad s^{-1} and 10^7rad s^{-1} respectively. Collision frequencies are of the order of 5s^{-1} for electrons and 0.1s^{-1} for ions giving in each case a mean free path of the order of 1000km. In cool loops and prominences the collision frequency is much higher and the mean free path much smaller as a consequence of the lower temperature and higher density.

These length scales are much smaller than those so far resolved in plasma loop structures and the time scales are shorter than those of all observed coronal phenomena except some transient flare systems. Furthermore, the plasma behaviour is in general

strongly anisotropic owing to the presence of the magnetic field. It turns out that in a magnetised plasma gradients parallel to the field where the mean free path is long tend to be much weaker than in the perpendicular direction. Under these circumstances the plasma may be treated as a fluid and the MHD description is appropriate.

Ideal (i.e. nondissipative) fluid equations appear to be a contradiction since the fluid approximation is based on the assumption that the system is locally close to a thermodynamic equilibrium which requires a certain rate of collisions and hence dissipation. However, even a collisionless plasma is not dissipationless. Even if Coulomb collisions are absent, small-scale plasma turbulence usually gives rise to stochastic particle orbits and phase-mixing and hence to efficient dissipation, though velocity distribution functions do not in general relax to a Maxwellian. For smooth quasistatic (see Section 1.5) plasma configurations dissipation rates are usually negligible so that they may be described using ideal MHD. We proceed by introducing the MHD equations in the next section.

1.4 The MHD Equations

Having decided to describe the solar atmospheric plasma motion using MHD we present in this section the MHD equations. The self-consistent theoretical description of a plasma is usually difficult because of the inter-relationship of the fluid dynamics and the electrodynamics. The motion of conducting material across the magnetic lines of force creates potential differences which generally cause electric currents to flow. Meanwhile the flow of electric current across a magnetic field is associated with a force, the Lorentz force, which influences the fluid flow. A self-consistent description therefore leads to non-linear equations.

The MHD equations have been discussed in many textbooks (e.g. Priest (1982), Parker (1979), Roberts (1967)).

In what follows we assume that:

- the plasma is a continuum. This is valid if the length scale for variation is much greater than typical internal plasma lengths such as the ion gyroradius.

- the plasma is in thermodynamic equilibrium with distribution functions close to Maxwellian. This holds for time-scales much larger than collision times and length-scales much longer than the mean free path.
- the magnetic diffusivity η is constant, and most of the plasma properties are isotropic (reasonable having assumed local thermodynamic equilibrium).
- the equations are written for an inertial frame. Effects of the Sun's rotation may be important for some large-scale processes, but we assume that they are not important for the structures considered in this thesis.
- electromagnetic variations are quasi-steady i.e. relativistic effects are neglected since the flow speed, sound speed and Alfvén speed are all much less than the speed of light.
- the plasma is a single fluid.
- the plasma is quasi-neutral i.e. $N_+ - N_- \ll n$ where N_+ and n_- are the number of positive and negative ions and $n = n_+ + n_-$ is the total number of ions.

Under these assumptions, Maxwell's equations can be written as

$$\nabla \times \mathbf{B} = \mu_0 \mathbf{j} \tag{1.5}$$

$$\nabla \cdot \mathbf{B} = 0 \tag{1.6}$$

$$\nabla \times \mathbf{E} = -\frac{\partial \mathbf{B}}{\partial t} \tag{1.7}$$

where \mathbf{B} is the magnetic induction, \mathbf{E} is the electric field, \mathbf{j} is the current density and μ_0 is the magnetic permeability. Ampère's Law (1.5) implies that currents may produce magnetic fields, Faraday's Law (1.7) implies that magnetic fields may cause electric fields. Gauss's law (1.6) for magnetic fields reflects the fact that magnetic monopoles have never been found.

The current density in a plasma moving at a nonrelativistic speed through a magnetic field is proportional to the total electric field in a frame of reference moving with the plasma as described by the simple single-fluid form of Ohm's Law

$$\mathbf{E} + \mathbf{v} \times \mathbf{B} = \frac{\mathbf{j}}{\sigma} \quad (1.8)$$

where σ is the electric conductivity of the plasma, here assumed to be scalar. More general forms of Ohm's Law are available: see Priest (1982), Section 2.1.3. We can rewrite equation (1.7) in terms of \mathbf{B} and \mathbf{v} by substituting for \mathbf{E} using Equation (1.8) and then for \mathbf{j} using Equation (1.5). After some vector manipulations, assuming that σ and μ_0 are constant, the induction equation is

$$\frac{\partial \mathbf{B}}{\partial t} = \nabla \times (\mathbf{v} \times \mathbf{B}) + \eta \nabla^2 \mathbf{B} \quad (1.9)$$

where $\eta = \frac{1}{\mu_0 \sigma}$ is the magnetic diffusivity. This equation couples the behaviour of the magnetic field with that of the plasma. In terms of a typical plasma speed V_0 and a typical length scale l_0 , the magnitude of the convective term divided by that of the diffusive term is a dimensionless parameter, the magnetic Reynold's number $R_m = l_0 V_0 / \eta$ measuring the strength of the coupling between the plasma and the magnetic field. In the solar atmosphere we take $R_m \gg 1$ (ideal MHD) and Equation (1.9) becomes approximately

$$\frac{\partial \mathbf{B}}{\partial t} = \nabla \times (\mathbf{v} \times \mathbf{B}), \quad (1.10)$$

the perfectly conducting limit, and magnetic field lines behave as if they move with the plasma (Alfvén's frozen flux theorem: see Priest, 1982). Furthermore, under this assumption Ohm's law is

$$\mathbf{E} + \mathbf{v} \times \mathbf{B} = 0. \quad (1.11)$$

The plasma motion is described by a mass continuity equation

$$\frac{\partial \rho}{\partial t} + \nabla \cdot (\rho \mathbf{v}) = 0, \quad (1.12)$$

a momentum conservation equation (equation of motion)

$$\rho \left(\frac{\partial \mathbf{v}}{\partial t} + \mathbf{v} \cdot \nabla \mathbf{v} \right) = \mathbf{j} \times \mathbf{B} - \nabla p + \mathbf{F} \quad (1.13)$$

and an energy equation (various different forms are possible)

$$\rho T \frac{Ds}{Dt} = -\mathcal{L} \quad (1.14)$$

where s is the entropy per unit mass of the plasma and \mathcal{L} is the energy loss function, the net effect of all sources and sinks of energy, e.g.

$$\mathcal{L} = \underbrace{\nabla \cdot \mathbf{q}}_{\text{heat flux}} + \underbrace{L_r}_{\text{radiative losses}} - \underbrace{\frac{\mathbf{j}^2}{\sigma}}_{\text{Ohmic heating}} - \underbrace{H}_{\text{everything else}} \quad (1.15)$$

For systems considered in this thesis an energy equation will not be used but alternative closure conditions will be used instead. Equation (1.12) says that the density in a volume changes if mass flows across its boundary so that the total mass is conserved. Equation (1.13) expresses the fact that the plasma moves subject to a pressure gradient, a Lorentz force and an external force \mathbf{F} e.g. the gravitational force $\mathbf{F} = -\rho \nabla \psi$ where ψ is a gravitational potential. The Lorentz force $\mathbf{j} \times \mathbf{B}$ can be decomposed into a magnetic tension force $\frac{1}{\mu_0} (\mathbf{B} \cdot \nabla) \mathbf{B}$ which is a directional derivative and a magnetic pressure force $-\nabla \left(\frac{B^2}{2\mu_0} \right)$, where $B = |\mathbf{B}|$ is the magnetic field strength, which is a gradient.

The Alfvén mach number $M = v/v_A$ gives the size of the flow speed $v = |\mathbf{v}|$ in terms of the Alfvén speed $v_A = B_0/\sqrt{\mu_0 \rho_0}$ where B_0 and ρ_0 are a typical magnetic field strength and density. The plasma beta $\beta_p = 2\mu_0 p_0/B_0^2$, where p_0 is a typical pressure, is the plasma pressure divided by the magnetic pressure and is a measure of the fluid's dominance over the magnetic field. From the relation involving the Alfvén speed and the sound speed $c_s = \sqrt{\gamma p_0/\rho_0}$ where $\gamma = c_p/c_v$ is the ratio of specific heats

$$\frac{c_s^2}{v_A^2} = \frac{\gamma \mu_0 p_0}{B_0^2} = \gamma \frac{\beta_p}{2} \quad (1.16)$$

the plasma beta is a comparison between the sound speed and the Alfvén speed. For example, above a sunspot where $v \approx 10^3 \text{m/s}$, $T \approx 10^4 \text{K}$ and $B \approx 10^3 \text{G}$, approximate

values are $c_s \approx 2 \times 10^4 \text{m/s}$, $v_A \approx 3 \times 10^5 \text{m/s}$, $M \approx 4 \times 10^{-3}$ and $\beta \approx 3 \times 10^{-3}$.

For simplicity we use as our equation of state the perfect gas law

$$p = \frac{k_B}{\mu} \rho T \quad (1.17)$$

where k_B is Boltzmann's constant and μ is the mean particle mass.

Solving the MHD equations is a formidable task and in an analytical project such as this one it is necessary to make simplifications such as to consider special cases e.g. static or symmetric cases or to impose a special form for the magnetic induction or the current density using vector potentials or Euler potentials (see Chapters 2 and 3). In the solar atmosphere the timescale for changes in some structures is large compared to the Alfvén time, the time taken by an Alfvén wave to cross the system. Therefore we can assume that the system evolves through a series of equilibrium states, the quasi-static approximation. In this thesis we will work without assuming symmetry (coordinate invariance) in our solutions but we will be restricted to steady ($\frac{\partial}{\partial t} = 0$) and static ($\frac{\partial}{\partial t} = 0$, $\mathbf{v} = \mathbf{0}$) cases. These cases and the quasi-static approximation are the subject of the next section.

1.5 The Magnetohydrostatic and Steady MHD Approximations

In this thesis we are concerned with structures which change slowly under quiet conditions, varying on a time-scale much larger than the typical MHD time scale. In addition only large-scale spatial variations are considered. We are interested both in steady cases (i.e. $\frac{\partial}{\partial t}$ small, see Chapter 2) and in static cases ($\frac{\partial}{\partial t}$ and \mathbf{v} small, see Chapters 3 and 4).

Consider the time-dependent MHD Equations (1.13), (1.10) and (1.12). The MHS and steady MHD approximations can be described systematically in the following way (see also Schindler & Birn, 1978,1986; Neukirch, 1999). Let L be the length scale of the system, t_0 the slow time scale of evolution and $v_A = B_0/\sqrt{\mu_0\rho_0}$ a typical Alfvén

speed. We then define the Alfvén time by $t_A = L/v_A$. We now normalize lengths by L , velocities by v_0 , the magnetic field by B_0 , the density by ρ_0 , the pressure by p_0 and the gravitational potential by ψ_0 . Normalised quantities are denoted by a $\tilde{\cdot}$. Equations (1.13) with $\mathbf{F} = -\rho\nabla\psi$, (1.10) and (1.12) can now be written, using Equation (1.5), as

$$\tilde{\rho} \left(\frac{t_A}{t_0} \frac{v_0}{v_A} \frac{\partial \tilde{\mathbf{v}}}{\partial \tilde{t}} + \frac{v_0^2}{v_A^2} \tilde{\mathbf{v}} \cdot \tilde{\nabla} \tilde{\mathbf{v}} \right) = \tilde{\mathbf{j}} \times \tilde{\mathbf{B}} - \frac{\beta_p}{2} \tilde{\nabla} \tilde{p} - \frac{\beta_g}{2} \tilde{\rho} \tilde{\nabla} \tilde{\psi} \quad (1.18)$$

$$\frac{L}{t_0 v_0} \frac{\partial \tilde{\mathbf{B}}}{\partial \tilde{t}} = \tilde{\nabla} \times (\tilde{\mathbf{v}} \times \tilde{\mathbf{B}}) \quad (1.19)$$

$$\frac{L}{t_0 v_0} \frac{\partial \tilde{\rho}}{\partial \tilde{t}} + \tilde{\nabla} \cdot (\tilde{\rho} \tilde{\mathbf{v}}) = 0 \quad (1.20)$$

Here, $\beta_p = 2\mu_0 p/B_0^2$ is the ratio between plasma pressure and magnetic pressure, the plasma beta as defined in Section 1.4, whereas $\beta_g = 2\mu_0 \rho_0 \psi_0/B_0^2$ is a similar ratio between the gravitational energy density and the magnetic pressure. Both numbers measure the relative importance of pressure gradient and gravitational force with respect to the $\mathbf{j} \times \mathbf{B}$ -force.

1.5.1 Magneto-hydrostatics

Magneto-hydrostatics (MHS) is the theory of the static ($\partial/\partial t = 0$, $\mathbf{v} = \mathbf{0}$) equilibria of the MHD equations. The main assumption is that

$$\frac{t_A}{t_0} = \frac{v_0}{v_A} = \epsilon \ll 1. \quad (1.21)$$

Since ϵ is assumed to be small, we obtain to lowest order for Equation (1.18)

$$\mathbf{0} = \tilde{\mathbf{j}} \times \tilde{\mathbf{B}} - \frac{\beta_p}{2} \tilde{\nabla} \tilde{p} - \frac{\beta_g}{2} \tilde{\rho} \tilde{\nabla} \tilde{\psi} \quad (1.22)$$

while the induction equation (1.19) and the mass continuity equation (1.20) remain unchanged except that they are seen to be first-order in ϵ (before dividing through by the scale of the terms with spatial derivatives). To lowest order we have the MHS force balance equation as fundamental equation and the time \tilde{t} appears merely as a parameter. The description of the quasi-static development of a structure therefore

requires the solution of Equation (1.23) at any instant in time, where the quasi-static solutions are connected through the time-dependent Equations (1.19) and (1.20). The quantities \mathbf{v} and ρ appear only in the first-order Equations (1.19) and (1.20). It is consistent with the approximation (ignoring terms in ϵ^2) to use a zero-order solution in the first-order equations. The fact that the MHD equations appear as two sets of equations which largely decouple from each other is particularly useful if a general MHS solution is available. Then we can understand the first-order equations as equations for \mathbf{v} and ρ with p and \mathbf{B} prescribed. Although the resulting time-dependent equations may be difficult to solve, a useful first step is to construct MHS solutions.

In MHS we consider a set of three equations:

$$\begin{aligned} \mathbf{j} \times \mathbf{B} - \nabla p - \rho \nabla \psi &= \mathbf{0} \\ \nabla \times \mathbf{B} &= \mu_0 \mathbf{j} \\ \nabla \cdot \mathbf{B} &= 0 \end{aligned} \tag{1.23}$$

This set of equations has to be completed by an equation of state and assumptions about the temperature or an energy equation. If $\mathbf{j} \times \mathbf{B} = \mathbf{0}$ then the magnetic stresses are carried through the region entirely within the field and are not transmitted to the fluid, and such a field is said to be force-free. Furthermore if the current density is zero then the magnetic field is curl-free and the field is said to be potential. It is useful to study MHS solutions because they are the simplest solutions of the very complicated MHD equations. Equally important from the point of view of modelling is the fact that many physical processes in plasma systems occur slowly, i.e. on time-scales which are much longer than the typical time-scale of the system.

1.5.2 Steady MHD

In the steady-flow case ($\frac{\partial}{\partial t} = 0$ only) we allow $v_0 \approx v_A$ but

$$\frac{t_A}{t_0} = \epsilon \ll 1. \tag{1.24}$$

Equations (1.13), (1.10) and (1.12) become

$$\tilde{\rho} \left(\epsilon \frac{v_0}{v_A} \frac{\partial \tilde{\mathbf{v}}}{\partial \tilde{t}} + \frac{v_0^2}{v_A^2} \tilde{\mathbf{v}} \cdot \tilde{\nabla} \tilde{\mathbf{v}} \right) = \tilde{\mathbf{j}} \times \tilde{\mathbf{B}} - \frac{\beta_p}{2} \tilde{\nabla} \tilde{p} - \frac{\beta_g}{2} \tilde{\rho} \tilde{\nabla} \tilde{\psi} \quad (1.25)$$

$$\epsilon \frac{v_A}{v_0} \frac{\partial \tilde{\mathbf{B}}}{\partial \tilde{t}} = \tilde{\nabla} \times (\tilde{\mathbf{v}} \times \tilde{\mathbf{B}}) \quad (1.26)$$

$$\epsilon \frac{v_A}{v_0} \frac{\partial \tilde{\rho}}{\partial \tilde{t}} + \tilde{\nabla} \cdot (\tilde{\rho} \tilde{\mathbf{v}}) = 0 \quad (1.27)$$

Neglecting first-order terms in ϵ we obtain

$$\tilde{\rho} \left(\frac{v_0^2}{v_A^2} \tilde{\mathbf{v}} \cdot \tilde{\nabla} \tilde{\mathbf{v}} \right) = \tilde{\mathbf{j}} \times \tilde{\mathbf{B}} - \frac{\beta_p}{2} \tilde{\nabla} \tilde{p} - \frac{\beta_g}{2} \tilde{\rho} \tilde{\nabla} \tilde{\psi} \quad (1.28)$$

$$\tilde{\nabla} \times (\tilde{\mathbf{v}} \times \tilde{\mathbf{B}}) = 0 \quad (1.29)$$

$$\tilde{\nabla} \cdot (\tilde{\rho} \tilde{\mathbf{v}}) = 0 \quad (1.30)$$

and \tilde{t} is once again relegated to parameter status. Where in MHS the equations reduce to a zeroth-order force-balance equation and two first-order time-dependent equations, in steady MHD we have three zeroth-order time-independent equations to solve. The equations do not decouple as they do in MHS and so the quasi-static evolution formulation does not carry over to steady MHD, although one could in principle construct a quasi-static evolutionary model using steady MHD equilibria. The system is completed by Equations (1.5), (1.6) and an energy equation or an alternative closure condition. Steady MHD equilibria are much more difficult to calculate than MHS equilibria as we discuss in the next section and in Chapter 2.

1.6 MHS and Steady MHD Equilibria: The General Picture and this Thesis

In MHS many symmetric solutions (i.e. solutions invariant in at least one coordinate direction) exist owing to the fact that, assuming a certain form for the magnetic field, the force-balance equation can be reduced to a single elliptic equation. This equation is called the Grad-Shafranov equation and many solutions are given in Neukirch (1999), Chapter 3. Because solving the Grad-Shafranov equation is a relatively simple

task involving standard techniques, analytical solutions are available for many different current structures and for a long time these solutions were standard tools for modelling magnetic structures in the solar atmosphere. This was justified by assuming e.g. loops and prominences to be translationally invariant and sunspots to be rotationally invariant to a reasonable approximation. However, it is clear from the manifest three-dimensionality of structures such as fluted sunspot penumbrae and coronal loops among others that these symmetric solutions cannot adequately address all situations and that in the case of such three-dimensional structures a move to three-dimensional equilibria is necessary.

For non-symmetric systems, however, a general equilibrium theory such as the Grad-Shafranov equation does not exist. Parker (1979) even proved that three-dimensional perturbations of two-dimensional equilibria cannot be in equilibrium, casting doubt on the existence of three-dimensional equilibria. Fortunately, in his proof Parker assumes existence and finiteness in all of R^3 . For solar applications the photosphere or some other surface is often considered as a boundary to the problem and Parker's proof no longer applies. In contrast to the situation with the Grad-Shafranov equation in two dimensions, for a three-dimensional problem it is not clear from the equations at the outset if an equilibrium exists at all. Three-dimensional equilibria are in use throughout this thesis, those in Chapter 2 summarised in Kaiser & Salat (1997) and those in Chapters 3 and 4 calculated by Low (1985, 1991, 1992, 1993a, 1993b) and Bogdan & Low (1986) with some additions by Neukirch (1995, 1997a, 1997b) and Neukirch & Rastätter (1999). Kaiser & Salat manage to reduce the force-balance equation to a system of nonlinear PDEs where even the differential operators are nonlinear (see that paper or our review in Chapter 2). Furthermore the equations are of mixed elliptic/parabolic/hyperbolic type so that no theory of well-posedness exists. Kaiser & Salat (1997) comprehensively calculate their class of solutions by rewriting their equations as a simple Grad-Shafranov-type elliptic equation coupled to a pair of difficult compatibility conditions, reducing the calculation to a complicated but systematic two-step process. The equilibrium class considered by Low and Neukirch, however, bears no resemblance to the Grad-Shafranov theory at all but instead is unexpectedly inspired by the standard treatment of Ampère's law in the theory of linear force-free fields (see

Chapter 3).

The work of this thesis uses these equilibria as a starting point. In Chapter 2 the equilibria of Kaiser & Salat (1997) are used in conjunction with a transformation method by Gebhardt & Kiessling (1992) to produce three-dimensional equilibria with steady, field-aligned, incompressible flow. These solutions are then used to provide simple models of plasma flow in loops and Evershed flow in fluted sunspot penumbrae. This is the first time that the transformation method has been applied to three-dimensional equilibria and to our knowledge the resulting equilibria are the only fully three-dimensional equilibria with flow apart from one by Chandrasekhar (1961). The work is motivated by the recent discovery that in the solar atmosphere plasma flow is more common than not (Fleck, 1997), while this is not reflected in the number of equilibria with flow available. Steady-state MHD has been of interest for a long time but the work in ideal MHD equilibria with flow has concentrated on symmetric systems. A generalised Grad-Shafranov equation can be found and, while this is elliptic in the incompressible flow case (Grad, 1960), for compressible flow the equation may change its type (Heinemann & Olbert, 1978). Therefore more success has been achieved in the incompressible flow case. Having taken pains to stress the difficulty surrounding the calculation of static three-dimensional equilibria and their scarcity, we emphasise the further rarity of three-dimensional equilibria with flow and the difficulties to be overcome in their calculation. The nonlinearities of the static case carry over to the flow case with some added complications. It is only via the transformation method of Gebhardt & Kiessling (1992), hinging on the identical structure of a form of the equations with flow and a form of the static equations with magnetic field gauged in a certain way, that these equilibria can be found. In calculating these equilibria we must work under the restrictions of both the static equilibria and the transformation method so that gravity is neglected, the flow is strictly field-aligned and incompressible and the magnetic field has some unphysical properties. However, bearing in mind the mathematical difficulties overcome and the advance over existing solutions, we argue that these limitations are a small price to pay for the first fully three-dimensional exact MHD models of flow in loops and Evershed flow in sunspot penumbrae.

Meanwhile Chapters 3 and 4 begin with the equilibrium class discussed by Neukirch

& Rastätter (1999). In Chapter 3 the relationship between the equilibrium class and the theory of linear force-free fields (see Neukirch & Rastätter, 1999) is exploited when a Green's function method for this class is derived inspired by an existing method for linear force-free fields (Chiu & Hilton, 1977). This is carried out with a view to applying the equilibria to boundary conditions in the form of line-of-sight photospheric magnetic field data from magnetograms and thereby extrapolating to give models of the solar atmosphere. Examples where a working version of this method is applied to observed magnetogram data are given and discussed in Chapter 4.

Methods for extrapolating models of the solar atmosphere from observed photospheric boundary data have been topics for research since the 1960s when potential field methods were developed. Existing extrapolation methods now include potential, linear force-free and nonlinear force-free methods. Potential and linear force-free methods can be implemented simply and quickly using only the line-of-sight photospheric magnetic field as a boundary condition and can provide a good representation of the coronal field over a local area and, although not as effective as nonlinear force-free methods in giving good global representations of active regions with non-uniform distributions of electric currents, the uncertainties surrounding the existence and uniqueness of nonlinear force-free solutions and the computational complexity of nonlinear force-free methods have the consequence that potential and force-free fields are still commonly used in generating coronal magnetic field models. Most extrapolation methods for potential and linear force-free fields are based on Green's functions, particularly in Cartesian coordinates for obtaining local models of structures in domains bounded below by a small part of the photosphere. The problem with these methods that we aim to address is that, being force-free, they do not give structured plasma models to be compared directly with observed plasma emission patterns but instead rely on the modeller to compare a number of fieldlines by eye with the emission patterns and to draw appropriate conclusions from this. In Chapter 3 we develop a non-force-free Green's function method, i.e. a method where the solution includes cross-field currents which structure the plasma giving for the first time self-consistent plasma model patterns to be compared directly with observation.

In Chapter 4 this comparison of the extrapolated model with observations is carried

out with mixed success for a number of examples of observed slowly-evolving phenomena. Solutions are calculated taking line-of-sight magnetograms as boundary data and the resulting plasma structures are compared to near-simultaneous emission patterns. The incompleteness of the success of these models in reproducing the emission patterns can be blamed on deficiencies in the MHS equilibrium class whose non-force-free current component is restricted to a special form to enable analytical integration of the force-balance equation and whose magnetic field offers no improvement over those of existing force-free methods and non-force-free methods using fast Fourier transforms (e.g. Aulanier, 1998, 1999) and is more limited than the nonlinear force-free fields of e.g. Amari et al. (1997). The effects of these restrictions cannot be known without implementing a full numerical approach to the problem for comparison. Given the complexity of nonlinear force-free methods this is not a realistic option at present and the restrictions imposed here by the analytical treatment seem to be a worthwhile compromise. Also the worked examples of Chapter 4 use the simplest possible non-force-free Green's function calculated in Chapter 3 and there is hope that, on adopting a more sophisticated Green's function in our working algorithm the greater flexibility will result in improved models. In the meantime the successful elements of the results in Chapter 4 encourage us to believe that this approach offers a worthwhile alternative to existing extrapolation methods and a first success in generating self-consistent plasma structures from observed magnetic field data.

1.7 Outline of Thesis

In this thesis analytical methods are used to solve the magnetohydrodynamic equations and the resulting solutions are used to give simple steady or static qualitative models of the macroscopic structure of certain magnetic features in the solar atmosphere. Some of the material in Chapters 2-4 appeared in the papers Petrie & Neukirch (1999) and Petrie & Neukirch (2000). In Chapter 2, new three-dimensional magnetohydrodynamic equilibria with steady field-aligned incompressible flow are calculated and are applied to modelling sunspots and coronal loop- or arcade-like structures. In Chapter 3 a Green's function method for a special class of magnetohydrostatic equilibria is derived with a view to solving Cartesian photospheric boundary value problems. In Chapter

4 the work of Chapter 3 is extended when a simple illustrative example of a Green's function solution of this type is given, before the Green's function method is applied to magnetogram data from SoHO/MDI and Big Bear observatories. The magnetohydrostatic structures calculated by this procedure are then compared as far as possible with available near-simultaneous emission patterns. Chapter 5 is a short concluding chapter summarising what has been achieved in the thesis and how the work may be built upon in the future.

Some extensions of Chapters 2 and 3 which are either peripheral to the main intention behind the work or which could not be carried to a satisfactory conclusion but nevertheless may be of interest appear as appendices. Appendix A describes an extension to the transformation method which we apply in Chapter 2 taking static solutions to solutions with steady flow. Since no static solutions of the required structure for application of the transformation to be possible are known this line of research has not been developed further. An alternative method for calculating the linear force-free Green's function is given in Appendix B. This calculation uses a standard method to be seen in textbooks (see e.g. Morse & Feshbach, 1953) in calculating the Green's function solution of the Helmholtz equation. Appendix B is therefore intended as a counterpoint to the non-standard derivations already known.

Chapter 2

Self-consistent steady state solutions with field-aligned incompressible flow

2.1 Introduction

In this chapter, new three-dimensional MHD equilibria with flow are calculated by transforming from a known class of static equilibria, and these new equilibria are applied in giving simple models of magnetic structures with flow in the solar atmosphere. A shorter version of this chapter was published as Petrie & Neukirch (1999).

Traditionally, the basic models for plasma systems occurring in the laboratory, in space, in the solar atmosphere and in other astrophysical objects use static solutions of the MHD equations. Usually additional symmetry assumptions are made to make the mathematical problem more tractable. However, plasma flows are common phenomena in laboratory and astrophysical plasmas and recently there has been a considerable increase in interest in solutions of the MHD equations including steady flows (e.g. Tsinganos, 1996; Throumoulopoulos & Pantis, 1996; Throumoulopoulos & Tasso, 1997; Throumoulopoulos, 1998; Tasso & Throumoulopoulos, 1998; Goedbloed et al., 1997; Lifschitz & Goedbloed, 1997).

This statement is in particular true for the case of the solar atmosphere which is the system which motivated the present investigation. Well-known examples of plasma flow observed in the solar atmosphere are the solar wind, the Evershed flow in sunspots and flows in coronal loops and arcades. Recent observations by the SoHO spacecraft actually indicate that plasma flow is the rule and not the exception in the solar atmosphere (see, for example, Fleck, 1997).

The investigation of the theory of the steady state MHD equations including steady flow has a long history (e.g. Grad, 1960; Solov'ev, 1967). The main obstacle for obtaining solutions with steady plasma flow is the nonlinearity of the governing MHD equations. The vast majority of the work on (ideal) MHD solutions with steady flows uses additional symmetry assumptions as in the static case. As in the static case the ideal MHD equations can then be reduced to a single non-linear second order partial differential equation. But, whereas in the static case the resulting PDE is always elliptic, in the case with steady compressible flow the PDE changes its type from elliptic to hyperbolic and back to elliptic at certain critical points (e.g. Heinemann & Olbert, 1978). The correct conditions at these critical points have been the subject of recent discussions (Goedbloed et al., 1997). In the case of incompressible flow the problem of critical points does not appear and the resulting equation is always elliptic as in the static case (e.g. Grad, 1960) and therefore more work has been done on the incompressible than on the compressible case.

For symmetric systems a number of analytical solutions are known with applications to both laboratory plasmas (e.g. Solov'ev, 1967; Zehrfeld & Green, 1972; Maschke & Perrin, 1980 and Agim & Tataronis, 1985), and astrophysical plasmas (e.g. de Ville & Priest, 1991a, 1991b; Tsinganos & Surlantzis, 1992, Tsinganos, Surlantzis & Priest, 1993 and Del Zanna & Chiuderi, 1996).

For many applications, however, we cannot idealise the system as being symmetric. The solar atmosphere is well-populated by structures which are clearly three-dimensional as is emphasised in the introduction to this thesis. If we are to meet the challenge posed by such structures we are forced to handle the MHD equations without assuming any coordinate invariance. Only an extremely small number of exact solutions with flow are known in 3D (to the knowledge of the author there is only one, see Chandrasekhar

(1961); however, some work has also been done on weakly three-dimensional solutions with flow by Birn, 1992). One particular application that we will discuss in this chapter is the sunspot. In recent years, observations have shown that the structure of the magnetic field even of simple sunspots is very complicated (e.g. Degenhardt & Wiehr, 1991; Title et al., 1993; Rimmele, 1995a, 1995b) and genuinely three-dimensional. Recent investigations (Martens et al., 1996; Neukirch & Martens, 1998) use static three-dimensional solutions to model the three-dimensional magnetic field structure of sunspots. The observations also show that the Evershed flow phenomenon is closely related to the three-dimensional structure of the magnetic field. For a more complete discussion we refer the reader to Section 2.5.1. One of the motivations of the present chapter is therefore to investigate the possibility of finding three-dimensional steady state MHD solutions with flow which may be used as models for sunspot fields.

Another application we consider in this chapter is flows in coronal loops and arcades. Flows in loops and arcades have been observed for a long time (e.g. Bray et al., 1991) and we want to find the first genuinely three-dimensional solutions which can be used as models for loops with stationary flow. A description of patterns of flow to be found in loops is included in Section 2.5.1.

It is well-known that even the problem of finding three-dimensional (i.e. non-symmetric) static MHD solutions is extremely difficult and only very special classes of solutions are known (e.g. Woolley, 1976, 1977; Shivamoggi, 1985; Salat & Kaiser, 1995; Kaiser & Salat, 1997; Low, 1982, 1984; Neukirch, 1995, 1997). The problem of finding steady state solutions with flow is then even harder and we therefore have to make a number of simplifying assumptions to be able to make any progress. These assumptions are: a) we neglect external forces such as gravity, b) we study only field-aligned flows and c) assume that the flow field is incompressible. We concede that these are rather severe restrictions but in view of the fact that the number of known three-dimensional solutions with flow is of the order one, any new solution will be potentially useful. Whereas assumption b) can be justified by the fact that for all of our applications the plasma β is low (i.e. the magnetic field is strong) so that Alfvén's frozen flux theorem applies, assumptions a) and c) do, for example, prevent any stratification from appearing in our models. Assumption a) relies on the flow speed staying small compared to the

propagation speed of compressional waves and implies that the density along a field line is constant but this does not imply that the density is constant throughout the region.

Under the assumptions just mentioned, it was already noted by Grad (1960) that steady state MHD solutions with flow can be generated by a transformation using solutions of steady hydromechanics. Grad (1960), however, did not formulate the transformation method in a way that it could be easily used. Gebhardt & Kiessling (1992) extended and completed the transformation method and formulated it in terms of Euler potentials for the non-symmetric case and in terms of the flux function for the symmetric cases. (A description of the basic properties of Euler potentials, the formulation relevant to our three-dimensional work, follows this introduction). Their method transforms static MHD solutions into steady state MHD solutions with sub-alfvénic field-aligned incompressible flow and solutions of stationary hydromechanics into steady state MHD solutions with super-alfvénic field-aligned incompressible flow.

In the way that Gebhardt & Kiessling (1992) formulated the method, it is in principle easily applicable if one knows either static MHD solutions in terms of a flux function in the symmetric case (or solutions to the steady hydromechanics equation with the same symmetry in terms of a stream function) or static MHD solutions expressed by Euler potentials (or in the Clebsch representation) for the non-symmetric case (or the equivalent steady hydromechanics solutions). Gebhardt & Kiessling (1992) themselves discuss a few examples for solutions with symmetry. To our knowledge the method has never before been applied to non-symmetric systems and we will carry this out for the first time in the present chapter.

One reason that this method has never been used before in three dimensions may be that of the small set of known non-symmetric static MHD solutions only a small subset is given in terms of Euler potentials (e.g. Woolley, 1976, 1977; Shivamoggi, 1985; Low, 1982, 1984; Salat & Kaiser, 1995; Kaiser & Salat, 1997) and only those by Woolley (1976, 1977), Shivamoggi (1985), Salat & Kaiser (1995) and Kaiser & Salat (1997) can be used in applying the method since only in these solutions does the gas pressure vary with the Euler potentials alone. The construction of non-symmetric equilibria in terms of Euler potentials is very difficult because the MHD equilibrium equations in

this case reduce to a system of two coupled non-linear partial differential equations of mixed elliptic-hyperbolic type for which no general theory on the existence and uniqueness of solutions is available. There is also no general procedure for constructing solutions and, in order to make progress, one has to fall back on certain ansatzes for the Euler potentials. The most general and most exhaustive discussion of one such ansatz is given by Kaiser and Salat (1997) which covers also the solutions given previously by Woolley (1977), Shivamoggi (1985) and Salat & Kaiser (1995). Kaiser and Salat (1997) investigate the ansatz $\mathbf{B} = \nabla f \times \nabla g$ where f is an arbitrary scalar function and $g = r, \theta$, or z in cylindrical polar coordinates. It turned out that for all Euler-potential representations considered, the problem can be reduced to an elliptic equation in two independent coordinates perpendicular to the particular coordinate line corresponding to g , and certain nonlinear compatibility conditions. For $g = z$ or θ non-trivial solutions of the reduced problem, i.e. non-symmetric equilibria, could be found. We found one interesting additional solution which was overlooked by Kaiser & Salat (1997), because it represents a special case, very similar in structure to solutions found by Low (1982) for cases including gravity. Since these equilibria are of a form compatible with the transformation method of Gebhardt & Kiessling (1992), we will apply the transformation method to some of them and try to apply the resulting steady state solutions with flow to magnetic structures in the solar atmosphere.

The organization of the chapter is as follows. In Section 2.2 we summarise the basic properties of Euler potentials in preparation for exploiting them throughout this chapter. In Section 2.3 we briefly outline the transformation method of Gebhardt & Kiessling (1992). In Section 2.4 we briefly summarize the available static solutions in Euler potential form. In Section 2.5 we discuss the solutions which have applications to coronal loops and sunspots. We finish with a discussion and conclusions in Section 2.6.

2.2 Euler Potentials

A general vector field in three dimensions requires three scalar functions of space to describe it but the magnetic field requires only two since it satisfies $\nabla \cdot \mathbf{B} = 0$. One

such representation which can be shown to be generally possible (at least locally) is

$$\mathbf{B} = \nabla\alpha \times \nabla\beta. \quad (2.1)$$

Here the scalar functions $\alpha(x, y, z)$ and $\beta(x, y, z)$ are called Euler potentials and this representation is sometimes referred to as a Clebsch representation. This representation is equivalent to using the vector potential $\mathbf{A} = \alpha\nabla\beta$ satisfying the gauge condition $\mathbf{A} \cdot \mathbf{B} = 0$. The Euler potentials for a given magnetic field are not unique because an arbitrary function of α can be added to β and vice versa without changing the field. More generally, it can be shown that any pair of functions $u(\alpha, \beta)$ and $v(\alpha, \beta)$ can be used in place of α and β if

$$\frac{\partial(u, v)}{\partial(\alpha, \beta)} \neq 0. \quad (2.2)$$

The vector fields $\nabla\alpha$ and $\nabla\beta$ are both perpendicular to \mathbf{B} and so surfaces of constant α or β are tangential to \mathbf{B} everywhere. It therefore follows that their intersections are field lines. If we know Euler potentials representing a field in a region of space then there exist two associated families of surfaces

$$\alpha(x, y, z) = \alpha_i, \quad \beta(x, y, z) = \beta_i, \quad (2.3)$$

where α_i and β_i are constants. Any field line is an intersection of two such surfaces, one from each family, characterised by the two parameters α_i and β_i where the α 's and β 's have constant values along their respective field line. In this way a formulation of the magnetic field in terms of Euler potentials allows a direct representation of the field lines not possible with an ordinary vector potential.

Given a magnetic field in a region surrounding a point P it is always possible in principle to derive a pair of Euler potentials describing it in some vicinity of the point. For a proof of this see Stern (1970).

Generally in non-symmetric cases the analytic derivation of Euler potentials is very difficult because $\nabla\alpha \times \nabla\beta$ is nonlinear and involves products of derivatives. This

nonlinearity prevents us from building a solution from a superposition of solutions, a disadvantage compared with ordinary vector potentials. Furthermore, the existence proof for Euler potentials is only valid locally. Over larger regions the Euler potentials may no longer be single-valued (for examples see Stern, 1970). In three dimensions we can only be sure that a magnetic field can be defined globally by a single pair of Euler potentials if the domain contains one surface which each field line intersects exactly once and if either the magnetic field has no null points $\mathbf{B} = \mathbf{0}$ in the domain or if the magnetic field has a potential \mathbf{A} such that $\mathbf{A} \cdot \mathbf{B} = 0$ (see Rosner et al., 1989), difficult criteria to meet in general. Fortunately in this thesis we avoid issues of global existence of Euler potentials since where they are used Euler-potential forms for the magnetic field are assumed at the beginning to enable calculation of the equilibria to take place at all. It is important to note, however, that magnetic fields representable with Euler potentials are a special case and prescribing a magnetic field in Euler potential form restricts the generality of a solution.

Despite the nonlinearity of the Euler potential representation and the further nonlinearity of the MHD equations in Euler-potential form, the Euler potentials reduce the MHD equations sufficiently to make calculation of three-dimensional equilibria possible, as can be seen in the following sections.

2.3 Transformation Method

We briefly summarise the basic idea behind the transformation method of Gebhardt & Kiessling (1992) for the sub-alfvénic case. In the super-alfvénic case we have to substitute $\mathbf{u} = \sqrt{\rho}\mathbf{v}$ for \mathbf{B} and $-(p + (1/2)|\mathbf{u}|^2)$ for p . The analysis can then be carried out in the same way as for the sub-alfvénic case.

The equations of static MHD are

$$\mathbf{j} \times \mathbf{B} = \nabla p \tag{2.4}$$

$$\mathbf{j} = \frac{1}{\mu_0} \nabla \times \mathbf{B} \tag{2.5}$$

$$\nabla \cdot \mathbf{B} = 0 \tag{2.6}$$

where \mathbf{B} is the magnetic field, \mathbf{j} the current density and p the pressure. We represent

the solenoidal field \mathbf{B} in terms of Euler potentials $f(\mathbf{x})$ and $g(\mathbf{x})$ where $\mathbf{x} \in \mathbb{R}^3$ and ∇f and ∇g are linearly independent,

$$\mathbf{B} = \nabla f \times \nabla g \quad (2.7)$$

so that \mathbf{B} satisfies Equation (2.6) automatically. Substituting Equation (2.7) into Equations (2.4) and (2.5) we can use the linear independence of ∇f and ∇g to resolve the resulting vector equations in the ∇f and ∇g directions to give

$$\begin{aligned} \nabla g \cdot \nabla \times (\nabla f \times \nabla g) &= \mu_0 \left(\frac{\partial p}{\partial f} \right)_g \\ \nabla f \cdot \nabla \times (\nabla f \times \nabla g) &= -\mu_0 \left(\frac{\partial p}{\partial g} \right)_f \end{aligned} \quad (2.8)$$

It is important for the method that the representation of the magnetic field \mathbf{B} in terms of Euler potentials is not unique (see Section 2.2) because any transformation from f, g to new Euler potentials a, b given by

$$f = f(a, b), \quad g = g(a, b) \quad (2.9)$$

would give the same magnetic field, but this time given by the equation

$$\mathbf{B} = [f, g]_{a,b} \nabla a \times \nabla b \quad (2.10)$$

where the Poisson bracket $[f, g]_{a,b}$ is defined by

$$[f, g]_{a,b} = \frac{\partial f}{\partial a} \frac{\partial g}{\partial b} - \frac{\partial f}{\partial b} \frac{\partial g}{\partial a} \quad (2.11)$$

and is equal to the Jacobian of the transformation from a, b to f, g . With the new unmatched Euler potentials a and b the Lorentz force becomes

$$\begin{aligned} (\nabla \times \mathbf{B}) \times \mathbf{B} &= [f, g]_{a,b} \nabla \times (\nabla a \times \nabla b) \times ([f, g]_{a,b} \nabla a \times \nabla b) \\ &\quad + (\nabla [f, g]_{a,b} \times (\nabla a \times \nabla b)) \times ([f, g]_{a,b} \nabla a \times \nabla b) \\ &= [f, g]_{a,b}^2 (\nabla \times (\nabla a \times \nabla b)) \times (\nabla a \times \nabla b) \\ &\quad + \frac{1}{2} \nabla [f, g]_{a,b}^2 |\nabla a \times \nabla b|^2 \end{aligned} \quad (2.12)$$

and Equations (2.8) are replaced by

$$\begin{aligned}
& ([f, g]_{a,b})^2 \nabla b \cdot \nabla \times (\nabla a \times \nabla b) - \\
& \quad \frac{1}{2} \frac{\partial}{\partial a} ([f, g]_{a,b})^2 (\nabla a \times \nabla b)^2 = \mu_0 \left(\frac{\partial p}{\partial a} \right)_b \\
& ([f, g]_{a,b})^2 \nabla a \cdot \nabla \times (\nabla a \times \nabla b) + \\
& \quad \frac{1}{2} \frac{\partial}{\partial b} ([f, g]_{a,b})^2 (\nabla a \times \nabla b)^2 = -\mu_0 \left(\frac{\partial p}{\partial b} \right)_a.
\end{aligned} \tag{2.13}$$

On the other hand, for steady state ($\frac{\partial}{\partial t} = 0$ for all quantities) MHD with field-aligned ($\mathbf{v} = \sigma \mathbf{B}$), incompressible ($\nabla \cdot \mathbf{v} = 0$) flow and magnetic field written in terms of Euler potentials α and β ($\mathbf{B} = \nabla \alpha \times \nabla \beta$), the induction equation (1.10) and Gauss's law (1.6) are trivially solved. The incompressibility condition implies that

$$\mathbf{B} \cdot \nabla \sigma = 0 \tag{2.14}$$

and, from the linear independence of \mathbf{B} , $\nabla \alpha$ and $\nabla \beta$, σ depends only on α and β and is constant along magnetic field lines. The mass continuity equation gives

$$\nabla \cdot (\rho \mathbf{v}) = \mathbf{v} \cdot \nabla \rho = \sigma \mathbf{B} \cdot \nabla \rho = 0 \tag{2.15}$$

so that ρ depends only on α and β and is also constant along magnetic field lines. The momentum balance equation can be written as

$$\rho \nabla \left(\frac{1}{2} \sigma^2 \mathbf{B}^2 \right) - \rho \sigma \mathbf{B} \times (\nabla \times \sigma \mathbf{B}) = -\nabla p + \mathbf{j} \times \mathbf{B}. \tag{2.16}$$

The scalar product of Equation (2.16) with \mathbf{B} gives

$$\begin{aligned}
\rho \mathbf{B} \cdot \nabla \left(\frac{1}{2} \sigma^2 \mathbf{B}^2 \right) + \mathbf{B} \cdot \nabla p &= \\
\mathbf{B} \cdot \nabla \left(\frac{1}{2} \rho \sigma^2 \mathbf{B}^2 + p \right) &= 0,
\end{aligned} \tag{2.17}$$

since ρ is constant along magnetic field lines, implying that the generalised pressure $\Pi = p + \frac{1}{2}\rho v^2$ depends only on α and β and is also constant along field lines.

We are now in a position to treat the momentum balance equation (1.13) and Ampère's law (1.5). Define the vector field $\mathbf{w} = \sqrt{\mu_0\rho}\mathbf{v}$. Then we can transform ρ out of the inertial term using \mathbf{w} :

$$\rho(\mathbf{v} \cdot \nabla)\mathbf{v} = \frac{1}{\mu_0}(\mathbf{w} \cdot \nabla)\mathbf{w} \quad (2.18)$$

again using the fact that ρ is constant along field lines. Using Ampère's law and the definition of $\Pi(\alpha, \beta)$, the momentum balance equation can be written as

$$(\nabla \times \mathbf{B}) \times \mathbf{B} - (\nabla \times \mathbf{w}) \times \mathbf{w} = \mu_0 \nabla \Pi. \quad (2.19)$$

If $M(\alpha, \beta) = \sqrt{\mu_0\rho}\sigma$ is the Alfvén Mach number $|\mathbf{v}|/v_A$, then $\mathbf{w} = M(\alpha, \beta)\mathbf{B}$ and

$$\begin{aligned} (\nabla \times \mathbf{w}) \times \mathbf{w} &= M^2(\nabla \times \mathbf{B}) \times \mathbf{B} + M(\nabla M \times \mathbf{B}) \times \mathbf{B} \\ &= M^2(\nabla \times \mathbf{B}) \times \mathbf{B} - \frac{1}{2}\nabla M^2|\mathbf{B}|^2. \end{aligned} \quad (2.20)$$

The momentum balance equation (1.13) can now be written as

$$(1 - M^2)(\nabla \times \mathbf{B}) \times \mathbf{B} - \frac{1}{2}\nabla M^2|\mathbf{B}|^2 = \mu_0 \nabla \Pi \quad (2.21)$$

which, resolved in the $\nabla\alpha$ and $\nabla\beta$ directions becomes

$$\begin{aligned} (1 - M^2)\nabla\beta \cdot \nabla \times (\nabla\alpha \times \nabla\beta) - \\ \frac{1}{2}\frac{\partial}{\partial\alpha}(1 - M^2)|\nabla\alpha \times \nabla\beta|^2 &= \mu_0 \frac{\partial\Pi}{\partial\alpha} \end{aligned} \quad (2.22)$$

$$\begin{aligned} (1 - M^2)\nabla\alpha \cdot \nabla \times (\nabla\alpha \times \nabla\beta) + \\ \frac{1}{2}\frac{\partial}{\partial\beta}(1 - M^2)|\nabla\alpha \times \nabla\beta|^2 &= -\mu_0 \frac{\partial\Pi}{\partial\beta}. \end{aligned}$$

Note that the quantities σ and ρ appear in Equations (2.22) in the combination

$M = \sqrt{\mu_0 \rho} \sigma$ so that in any solution of Equations (2.22) for α and β with prescribed M and Π there remains one degree of freedom - we can choose one of σ and ρ freely thereby defining the other. We also mention that the square of the Alfvén Mach number is exactly half the ratio of the energy density of the flow and the magnetic energy density. Therefore the value of the square of the Alfvén Mach number directly provides an estimate of the relative energies stored in the flow field and in the magnetic field.

The similarity between Equations (2.13) and Equations (2.22) is striking. Moreover, if we replace a , b , $([f, g]_{a,b})^2$, and p in Equations (2.13) by α , β , $1 - M^2$, and Π , respectively, we obtain exactly Equations (2.22). It is at this point that it is important to distinguish between sub-alfvénic ($M^2 < 1$) and super-alfvénic ($M^2 > 1$) flow (see Gebhardt & Kiessling, 1992, for an extension of the method to cases including critical cases where $M^2 - 1$ has zeros).

This means that if we have a solution of Equations (2.8) then we can get solutions of the equations of steady state MHD with sub-alfvénic flow (2.22) by solving the equation

$$[f, g]_{\alpha, \beta} = \sqrt{1 - M^2(\alpha, \beta)} \quad (2.23)$$

for given $M(\alpha, \beta)$. Since this is only one equation for two unknowns, one of the transformation equations can be chosen conveniently and Equation (2.23) then has to be solved to obtain the other one.

Once the transformation is known, we can calculate the other physical quantities of the steady state solution with flow. The magnetic field is given by

$$\mathbf{B} = \nabla \alpha \times \nabla \beta = \frac{1}{[f, g]_{\alpha, \beta}} \nabla f \times \nabla g \quad (2.24)$$

and the velocity field by

$$\mathbf{v}_{\pm} = \pm \frac{|M(\alpha, \beta)|}{\sqrt{\mu_0 \rho}} \mathbf{B}. \quad (2.25)$$

The generalised pressure Π is the same function of \mathbf{x} as the pressure p because

$$\Pi(\alpha(\mathbf{x}), \beta(\mathbf{x})) = p[f(\alpha(\mathbf{x}), \beta(\mathbf{x})), g(\alpha(\mathbf{x}), \beta(\mathbf{x}))], \quad (2.26)$$

but $\Pi(\eta, \xi) \neq p(\eta, \xi)$.

The task is now reduced to a two-step process: a) find a non-symmetric static MHD equilibrium in Euler potential form and b) find a suitable transformation to a steady state MHD solution with sub-alfvénic flow.

It is possible (Gebhardt & Kiessling, 1992) to extend this transformation method to one transforming a MHS equilibrium together with a matching hydromechanical equilibrium to a steady MHD equilibrium with incompressible field-aligned flow which has both super- and sub-alfvénic velocities by rewriting the steady flow equations with gauged magnetic field in terms of the original Euler potentials. This would be useful for, e.g., modelling fast flow in coronal loops but unfortunately no suitable hydromechanical equilibria are known to the author.

Two variations of this transformation are given in Appendix A. One of them transforms from static 3D MHD without gravity to 3D MHD with steady field-aligned incompressible flow and gravity while the other transforms from static 3D MHD with gravity to 3D MHD with steady incompressible field-aligned flow and gravity.

Having introduced the transformation method we introduce in the next section the three-dimensional static equilibria to which the method will be applied.

2.4 Non-symmetric Static MHD Solutions

2.4.1 Solutions in Cartesian Coordinates

One class of non-symmetric solutions discussed by Kaiser and Salat (1997) has the form

$$\mathbf{B} = \nabla f \times \nabla y, \quad (2.27)$$

where f depends on all three coordinates x , y , and z (we remark that our coordinate system is rotated with respect to the coordinate system used by Kaiser and Salat (1997), because our coordinate system is more in line with the intended solar applications). Since there is no B_y component the field lines are confined to the planes $y = \text{constant}$. Magnetic fields of this type are therefore sometimes called laminated fields.

The equilibrium equations (2.8) reduce in this case to

$$-\Delta_2 f = \mu_0 \left(\frac{\partial p}{\partial f} \right)_y \quad (2.28)$$

$$\frac{\partial}{\partial y} \left\{ p + \frac{1}{2\mu_0} \left[\left(\frac{\partial f}{\partial x} \right)^2 + \left(\frac{\partial f}{\partial z} \right)^2 \right] \right\} = 0 \quad (2.29)$$

in the ∇f and ∇y directions respectively, where

$$\Delta_2 = \frac{\partial^2}{\partial x^2} + \frac{\partial^2}{\partial z^2}.$$

The first equation has the form of a Grad-Shafranov equation with a parametric y -dependence and the second equation states that the variation of the total pressure $p_T = p + |\mathbf{B}|^2/(2\mu_0)$ in the y -direction vanishes.

Solutions of this type have been found by Woolley (1977), Shivamoggi (1985) and Salat and Kaiser (1995). Low (1982) has found solutions of this type for cases with an external gravitational field and for force-free cases ($p = \text{constant}$; Low, 1988).

Kaiser and Salat (1997) discuss solutions obtained from pressure functions p in the form

$$p(f, y) = p_0(y) + p_1(y)f + \frac{1}{2}p_2(y)f^2 \quad (2.30)$$

rendering Equation (2.28) linear in f . The major difficulty is to find solutions $f(x, y, z)$ and functions $p_0(y)$, $p_1(y)$, and $p_2(y)$ which also satisfy the nonlinear Equation (2.29). Kaiser and Salat (1997) manipulate the condition (2.29) into a set of two nonlinear compatibility conditions for f that have to be satisfied. They present solutions for several special cases. For the case $p_2(y) = 0$ they find solutions of the type

$$f(x, y, z) = a(y)x^2 + 2b(y)xz + c(y)z^2 \quad (2.31)$$

where the functions $a(y)$, $b(y)$ and $c(y)$ are related by the conditions

$$a(y)c(y) - b(y)^2 = \text{constant} \quad (2.32)$$

and $a(y)$ and $c(y)$ are related to $p_1(y)$ by

$$a(y) + c(y) = \frac{1}{2}p_1(y). \quad (2.33)$$

Also one has $p_0(y) = \text{constant}$ for this solution.

For the case $p_2(y) \neq 0$ one can set $p_1(y) = 0$ without loss of generality, because the corresponding part of the solution does not contribute to \mathbf{B} . Kaiser and Salat (1997) discuss two different special forms for f . The first form for f they discuss is

$$f(x, y, z) = g(x, y)h(z, y). \quad (2.34)$$

Kaiser and Salat (1997) dismiss this form for f because they argue that it leads only to solutions with non-closed pressure surfaces. It seems, however, that they have overlooked the following special case which is consistent with Equation (2.34):

$$f(x, y, z) = g(x, y) \exp(-kz) \quad (2.35)$$

if $p_1(y) = 0$. Substituting Equation (2.35) into Equation (2.28) one finds

$$g(x, y) = g_1(y) \sin(\kappa(y)x) + g_2(y) \cos(\kappa(y)x) \quad (2.36)$$

with $\kappa^2(y) = k^2 + p_2(y)$. Equation (2.29) then implies that

$$p_0(y) = \text{constant} \quad (2.37)$$

and

$$\kappa^2(y) (g_1^2(y) + g_2^2(y)) = \text{constant}. \quad (2.38)$$

We remark that we have not discussed the most general possible form of the solution here but only the case which is useful for possible later applications of the transformation method.

The other ansatz discussed by Kaiser and Salat (1997) leads to solutions of the form

$$f(x, y, z) = \frac{c}{k} \left(a(y) \cos(kz) + \frac{b}{a(y)} \sin(kx) \right) \quad (2.39)$$

with b , c and $k^2 = p_2$ constant and $a(y)$ arbitrary. For p_2 negative the trigonometric functions have to be replaced by hyperbolic functions.

2.4.2 Solutions in Cylindrical Coordinates

Here the solutions found have the form

$$\mathbf{B} = \nabla f \times \nabla \theta. \quad (2.40)$$

Again the Equations (2.8) reduce to a Grad-Shafranov like equation with parametric θ dependence

$$-\frac{1}{r} \frac{\partial}{\partial r} \left(\frac{1}{r} \frac{\partial f}{\partial r} \right) - \frac{1}{r^2} \frac{\partial^2 f}{\partial z^2} = \mu_0 \left(\frac{\partial p}{\partial f} \right)_\theta \quad (2.41)$$

and the total pressure balance in the θ -direction

$$\frac{\partial}{\partial \theta} \left\{ p + \frac{1}{2\mu_0 r^2} \left[\left(\frac{\partial f}{\partial r} \right)^2 + \left(\frac{\partial f}{\partial z} \right)^2 \right] \right\} = 0 \quad (2.42)$$

Again solutions are sought for

$$p = p_0(\theta) + p_1(\theta)f + \frac{1}{2}p_2(\theta)f^2. \quad (2.43)$$

In the case $p_2(\theta) = 0$ the presented solution has the form

$$f(r, \theta, z) = \frac{1}{8}p_1(\theta)r^4 + \frac{1}{2}a(\theta)r^2 + bz + \frac{1}{2}cr^2z \quad (2.44)$$

where b and c are constant and $p_1(\theta)$ is related to $a(\theta)$ by

$$a(\theta) = \frac{b}{c}p_1(\theta) + d. \quad (2.45)$$

We also find

$$p_0(\theta) = \hat{p} - \frac{1}{2}a^2(\theta). \quad (2.46)$$

The function $p_1(\theta)$ and the constants b and c are arbitrary. It turns out that only the choice $b = 0$ avoids singularities of the magnetic field at $r = 0$. Therefore, only $p_1(\theta)$ and c are really unrestricted.

For the case $p_2(\theta) \neq 0$, Kaiser and Salat (1997) present solutions for which $p_1(\theta) = 0$ and $p_2(\theta) = \text{constant}$. In this case, $f(r, \theta, z)$ has the form

$$f(r, \theta, z) = (b_1(\theta) + c_1z) \sin \left(\frac{1}{2}\sqrt{|p_2|r^2} \right) + (b_2(\theta) + c_2z) \cos \left(\frac{1}{2}\sqrt{|p_2|r^2} \right) \quad (2.47)$$

for $p_2 < 0$ and

$$f(r, \theta, z) = (b_1(\theta) + c_1z) \sinh \left(\frac{1}{2}\sqrt{p_2r^2} \right) + (b_2(\theta) + c_2z) \cosh \left(\frac{1}{2}\sqrt{p_2r^2} \right) \quad (2.48)$$

for $p_2 > 0$. Here c_1 and c_2 are constant and $b_1(\theta)$ and $b_2(\theta)$ are related by

$$c_1b_1(\theta) + c_2b_2(\theta) = \text{constant}. \quad (2.49)$$

For cylindrical coordinates there is no equivalent to the Cartesian solution type (2.35). This can be proved by substituting a similar expression into the consistency relations

given by Kaiser and Salat (1997), their Equations (39), where the first equation gives for Euler potential $H = H_0(r, \theta)e^{-\kappa z}$

$$\frac{\partial}{\partial \theta} \left(\frac{1}{r^2} \kappa^2 h_0^2(r, \theta) \right) = 0 \quad (2.50)$$

and any solution is necessarily two-dimensional.

2.5 Non-symmetric solutions with steady flow

2.5.1 Background

In general, to each of the static solutions discussed in the last section the transformation method could be applied to generate solutions with flow. It is, however, clear that such an approach is useless unless one has some physical background information which helps to choose the appropriate static solution and the most useful type of transformation. Our main concern is to model, within the confines of the available choice of static solutions, magnetic structures in the solar atmosphere, especially coronal arcades or loops and sunspots. Therefore we first give a brief discussion of the criteria we used to choose particular solutions and the corresponding transformations. In all cases that we discuss in this chapter we assume that we have an appropriate source of mass at one end of each field line and a corresponding sink at the other end.

Flows in coronal loops have been studied theoretically for a long time (e.g. Bray et al., 1991) whereas the direct observational evidence of flows in loops or arcades has been comparatively scarce. Recent observations with the SoHO spacecraft (e.g. Brekke et al., 1997; Fleck, 1997) have shown for the first time that plasma flows in loops and arcades are quite a common phenomenon in the solar corona. The static solutions which are most appropriate to model coronal loops or arcades are the Cartesian cases (2.35) and (2.39). We will generally introduce a lower boundary at $z = 0$ which we loosely identify with the photosphere. If we make reasonable choices for the free functions $g_1(y)$ and $g_2(y)$, the solution (2.35) will be bounded in the half space $\{x, y, z | z \geq 0\}$. The solution (2.39) is only suited to model arcades locally because it is periodic in z and we have to introduce an upper boundary at a height $z = z_{max}$ corresponding to

the period of the function in the z -direction. More details about the specific solutions and the transformations used to obtain solutions with flow from the static solutions can be found in Subsection 2.5.2.

It has been known since the late fifties (Bray et al., 1991) that there are three patterns of flow associated with active region loops: a flow down both legs starting at the top of the loop, a flow up one leg and down the other and a mainly horizontal back-and-forth motion of the whole loop oscillating. For such long-lasting flows a steady-flow model may be reasonable but a field-aligned flow model will only be possible for a loop with unidirectional flow up one leg and down the other. Most observed velocities lie in the range 20 – 150km/s. The motion may continue in the loop for up to several hours, roughly the same interval over which loop systems last.

The longest-known flow phenomenon in the solar atmosphere is the Evershed effect (Evershed, 1909). Although Evershed flow has been observed to be time-dependent (e.g. Shine et al., 1994) we are only interested in steady properties of the flow because of the limitations of our solutions. The structure of even the most regular sunspot is very complicated and our intention is to describe with our models only the most basic features of the most regular sunspot. The complexity of structure of a sunspot depends partly on its size and partly on its stage of evolution. In general the most regular penumbral structure is to be seen in leader spots which have reached the stationary stage of their development. This regular structure consists of a pattern of narrow bright fibrils on a darker background running radially outward from the inner penumbra to the photosphere. However, even in a regular spot the fibrils frequently branch and coalesce, and the clarity of fibril detail can vary in one spot. Statistical analyses of data for the total and umbral areas of individual spots have been used to calculate an average ratio of the umbral radius to spot radius of just over 0.4. The classical description of the magnetic field configuration inside a single regular sunspot was given by Hale and Nicholson in 1938 (see Bray & Loughhead, 1964) and we summarise it as follows. The field is symmetrical around the axis of the spot. It has its maximum strength at the centre of the umbra, where the fieldlines are vertical. Away from the centre of the umbra the fieldlines become inclined to the vertical reaching 70° at the outer boundary of the penumbra, and the field strength decreases with radius.

For a long time, the apparent cross-field direction of the plasma flow and its abrupt vanishing at the outer penumbral boundary of a sunspot has puzzled solar researchers. In recent years, high resolution observations of sunspots with many different methods have revealed that the magnetic field in the sunspot penumbra has a very complicated three-dimensional structure called flutedness (also sometimes referred to as an uncombed or corrugated field or spines). These observations confirmed that both the alternating dark and bright fibrils extending in the radial direction across the penumbra and the Evershed flow are closely correlated with the three-dimensional structure of the magnetic field. Observations by Beckers and Schröter (1969) have suggested that the magnetic field inside the dark fibrils might be close to horizontal whereas the field in the bright fibrils is less inclined with respect to the vertical. This magnetic field structure has implications for the Evershed flow which was also suggested to be mainly associated with the dark fibrils. The association of the Evershed flow with the dark penumbral fibrils has been confirmed by Shine et al. (1994) and Rimmele (1995a, 1995b). Shine et al. (1994) deduce this from the fact that the bright fibrils are correlated with inclined magnetic field lines suggesting structures that rise with radial distance, restricting the Evershed effect to the dark fibrils. Rimmele (1995a, 1995b) provides more detail. Near the inner penumbral boundary blueshifted plasma is observed by Rimmele (1995a) corresponding to the upstream legs of the Evershed loops. At about one third of the penumbral radius the blueshift gradually turns to redshift as the loops reach their maxima and start to return to the surface. Within the penumbra dark fibrils are observed which are correlated with the velocity fibrils. These dark fibrils turn bright near the outer penumbral boundary and extend into the adjacent photosphere where they correlate perfectly with extensions of the velocity fibrils which usually end in brightly intense features and display a strong redshift. Rimmele (1995b) reports that the flow extends far beyond the penumbral boundary in contrast to the conclusions of earlier investigations (e.g. Title et al., 1993) although it decreases abruptly at the penumbral boundary so that it is difficult to observe beyond there. The flow is confined to a loop structure which is elevated above the surface at approximately one photospheric scale height. The correlation of velocity fibrils with dark fibrils is good provided that the velocity and intensity signals come from approximately the same height (Stanchfield II et al., 1997 confirmed these time-averaged results with their instantaneous flow maps).

Westendorp-Plaza et al. (1997) describe relatively low-lying flux tubes carrying most of the Evershed flow re-entering the solar surface in or just beyond the outer penumbra with other more elevated tubes carrying a small proportion of the flow well outside the sunspot. They estimate that the down-flowing mass just outside the penumbral boundary to the up-flowing mass in the inner penumbra agree to a remarkable extent. The observations of Degenhardt & Wiehr (1991) and Title et al. (1993) show that the average inclination, defined as the angle of a field line with the vertical direction, of the magnetic field increases from $40^\circ - 50^\circ$ to $70^\circ - 75^\circ$ across the penumbra and that there is a rapid azimuthal variation of the inclination angle of amplitude about $15^\circ - 18^\circ$. The observations also show that magnetic field strength does not vary strongly with azimuth and that the azimuthal field component is weak compared to the other two components. The fundamental problem thus posed by the observations is that a genuinely three-dimensional solution of the MHD equations is necessary. So far, this problem has only been solved using force-free fields, i.e. neither plasma flow nor other forces have been included. Linear force-free models (Martens et al., 1996) have some difficulties in explaining the observations in a simple way whereas exact fluted non-linear force-free solutions do not exist in the appropriate cylindrical coordinates, but approximate solutions have been successfully used to model the field within the penumbra (Neukirch & Martens, 1997). It is clear that the static cylindrical solutions (2.44) and (2.47) would be most appropriate to model simple round sunspots, but as we will see later both solutions can only be considered as local and very rough models. More details about the solutions and the transformations used to obtain solutions with flow from the static solutions can be found in Subsection 2.5.3. Cartesian solutions, especially (2.35), can also be considered as approximate models for the penumbra as lowest order terms of an asymptotic expansion procedure similar to the one used by Neukirch & Martens (1998) for force-free fields. We will discuss these models and the transformed solutions with flow in Subsection (2.5.2).

2.5.2 Solutions in Cartesian coordinates

Arcade-like solutions

As already mentioned in Section 2.5.1 the most realistic static solution for the solar applications that we have in mind is the solution (2.35) because it is bounded in the half space $\{x, y, z | z \geq 0\}$. This is not the case for the other solutions we will discuss later and for them we will have to restrict our treatment to a finite domain. We therefore discuss the solution (2.35) first.

For an arcade-like solution we can write Equation (2.35) with

$$g(x, y) = \sqrt{g_1(y)^2 + g_2(y)^2} \cos(\kappa(y)x - \phi_{ph}(y)) \quad (2.51)$$

where $\phi_{ph}(y) = \arctan\left(\frac{g_1(y)}{g_2(y)}\right)$ is the phase angle. The corresponding magnetic field \mathbf{B} is

$$B_x = B_0 \frac{k}{\sqrt{k^2 + p_2(y)}} \cos(\sqrt{k^2 + p_2(y)}x - \phi_{ph}(y)) \exp(-kz) \quad (2.52)$$

$$B_y = 0 \quad (2.53)$$

$$B_z = -B_0 \sin(\sqrt{k^2 + p_2(y)}x - \phi_{ph}(y)) \exp(-kz). \quad (2.54)$$

We see that the z -component of the magnetic field changes sign at $x = \frac{\phi_{ph}(y)}{\sqrt{k^2 + p_2(y)}}$, i.e. $x = \frac{\phi_{ph}(y)}{\sqrt{k^2 + p_2(y)}}$ represents a polarity inversion line. The minus sign in front of the B_z component is necessary to obtain arcade-like field lines at $x = \phi_{ph}(y)$. The pressure is given by

$$\begin{aligned} p &= p_0 + \frac{1}{2}p_2(y)f^2 \\ &= p_0 + \frac{1}{2}p_2(y) \frac{B_0^2}{k^2 + p_2(y)} \cos^2(\sqrt{k^2 + p_2(y)}x - \phi_{ph}(y)) \exp(-2kz) \end{aligned} \quad (2.55)$$

The pressure has its minimum in y where the field lines extend furthest from the photosphere. We can now exploit our freedom to choose $p_2(y)$ or $g_2(y)$ to shape the solution. As an example, we have chosen $\phi_{ph} = 0$ and $g_2(y) = g_{21} + g_{22}(1.0 - \text{sech}^2(2y))$ with $g_{21} = 0.75$ and $g_{22} = 0.15$ giving a non-periodic three-dimensional arcade-like

solution (see Figure 2.1) but making sure that the quadratic term in the pressure Equation (2.55) is kept positive.

We now use the transformation method to generate solutions with flow. This can be done by choosing the Mach number $M(\alpha, \beta)$ in a convenient way. We choose an Alfvén Mach number function that concentrates $|\mathbf{v}|$ around a particular field line. Since we are only looking for solutions with sub-alfvénic flow ($M^2 < 1$) we know that the Jacobian of the transformation from f, g to α, β is non-zero everywhere. The transformation is also invertible and we can, in principle, also regard α and β as functions of f and g . This gives us the possibility of prescribing M directly as a function of f and g . Note that we do not necessarily need to calculate f and g as functions of α and β (or vice versa), because once M is known as a function of space which is constant along field lines, we can calculate the magnetic field from Equation (2.24) and the velocity field from Equation (2.25). The total pressure is given as a function of space by the pressure of the static solution. The density does only have to be constant along field lines but is arbitrary otherwise, which means that we can choose an arbitrary positive definite function of f and g . Once the density is known, the plasma pressure for the steady state case with flow can be calculated from the definition of the total pressure. This completes the calculation of the physical quantities as functions of space. Note, however, that in this way we are not able to derive the dependence of M or Π on α and β , unless we solve Equation (2.23).

We choose

$$M^2 = M_0^2 \frac{1}{\cosh^2\left(\frac{f(x, y, z) - f_0}{\Delta f}\right) \cosh^2\left(\frac{y}{\Delta y}\right)}. \quad (2.56)$$

This choice concentrates the flow on the field line with $f(x, y, z) = f_0$ and $y = 0$ with half-widths Δf and Δy , respectively.

In Figure 2.1 we show an example with $f_0 = f(0.5, 0.0, 0.0)$, $\Delta f = 0.1$, $\Delta y = 0.1$ and $M_0^2 = 0.5$. The parameter values for the static solution are $k = 1$, $g_{21} = 0.8$, $g_{22} = 0.1$ and $\gamma = 2$. Figure 2.1 is designed to display graphically the variation of the velocity amplitude on each field line and from field line to field line by using a colour code. The picture is plotted taking the velocity amplitude to be $|\mathbf{v}| = M|\mathbf{B}|$, i.e. assuming that the density in Equation (2.25) is constant so that M is directly proportional to σ .

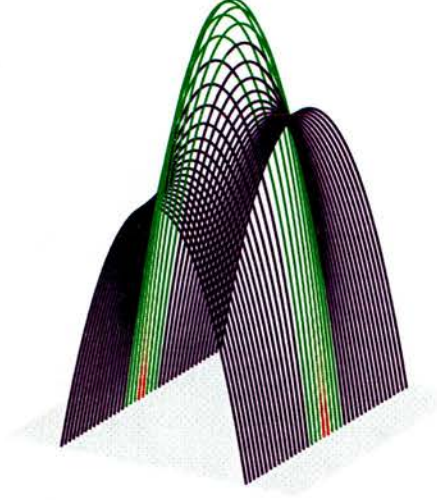


Figure 2.1: Magnetic field lines of an arcade-like stratified solution (2.52)-(2.54) with flow. The plasma flow speed is colour-coded as follows. On velocity field lines with non-zero flow, speed ranges from slow (green) to fast (red). Blue indicates zero flow speed. In this example we have chosen $g_2(y) = 0.75 + 0.15(1.0 - \text{sech}^2(2y))$ in the static solution. The static solution has been transformed using the form of the Mach number given in Equation (2.56) with parameter values $f_0 = f(0.5, 0.0, 0.0)$, $\Delta f = 0.1$, $\Delta y = 0.1$ and $M_0^2 = 0.5$. The colour code shows the velocity amplitude with blue referring to very low velocity, green referring to medium velocity and red referring to high velocity. It can be seen that the flow is confined to the set of field lines in the middle part and that the largest velocities are reached close to the lower boundary. Note that the field lines shown do not lie on the same surface of constant pressure. They are the set of field lines through the line $x = 0.5$ on the photosphere.

Recall from Section 2.3, however that because σ and ρ only appear in the flow equations in the combination $M = \sqrt{\mu_0 \rho} \sigma$ we have a further degree of freedom to work with. We could therefore alter the situation and, for example, concentrate ρ on the flow lines of Figure 2.1, keeping σ as it is, and adjust M to preserve the relation $M = \sqrt{\mu_0 \rho} \sigma$. This would give a model of an isolated coronal loop of dense, flowing plasma in an atmosphere of sparse, static plasma.

Because in this solution the field strength and the pressure are vertically stratified and $|\mathbf{v}|$ is proportional to $|\mathbf{B}|$ on each field line, the flow speed is stratified as well, i.e. the flow speed has its maximum at the photosphere and its minimum at the loop top.

As an alternative arcade-like solution we choose the special case of (2.39) with $b = 1$. The magnetic field of this solution is given by

$$B_x = a(y)c \sin(kz) \quad (2.57)$$

$$B_y = 0 \quad (2.58)$$

$$B_z = -\frac{c}{a(y)} \sin(kx) \quad (2.59)$$

The solution still contains two free parameters (c and k) and the free function $a(y)$. The solution is periodic in the x - and z -directions and we therefore have to restrict the domain on which we discuss the solution to the set of points $\{x, y, z \mid -\pi/(2k) \leq x \leq \pi/(2k), 0 \leq z \leq \pi/(2k)\}$. In this domain the field lines have an arcade-like shape. As an example we have chosen $c = k = 1$ and $a(y) = a_1 + a_2 \sin 2y$ with $a_1 = 0.6$ and $a_2 = 0.1$.

We can now add field-aligned flow to the solution using the same choice of Alfvén Mach number function as for the stratified solution discussed above the previous subsection. A plot of the resulting field lines is shown in Figure 2.2. Again, the plotted field lines are colour coded to show the amplitude of the velocity field. For this solution we have chosen our parameters such that the field strength along the field lines carrying flow increases from the foot points to the loop top. Therefore the velocity increases as well as can be clearly seen by the red colour code.

Note that with solutions of this type it is possible to have unidirectional plasma flow in a loop whose footpoints have equal pressure values or even, owing to the insensitivity of the equations to the sign of σ , unequal pressure values which would be expected to

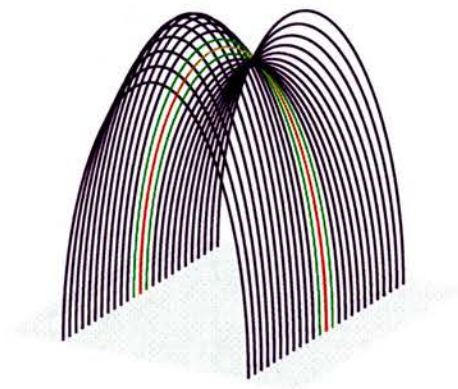


Figure 2.2: Static solution (2.57)-(2.59) in Cartesian coordinates (x, y, z) taken from Kaiser & Salat (1997) with $\mathbf{B} = \nabla f(x, y, z) \times \nabla y$ laminated. The plasma flow speed is colour-coded as in Figure 2.1. We can choose the shape of the arcade-like solution in the y -direction. In this example we have chosen $a(y) = 0.6 + 0.1 \sin 2y$. Note that the field lines drawn do not lie on a single surface of constant pressure. They are the set of field lines through the line $x = 0.5$ on the photosphere.

cause a siphon flow (Thomas, 1995) in the opposite direction.

Sunspot-like solutions

Although the most appropriate coordinate system for the description of simple sunspots would be a cylindrical coordinate system with its origin at the spot centre, a Cartesian solution can still be a very useful model for the outer part of the spot, the penumbra (e.g. Chou et al., 1993; Neukirch and Martens, 1998). In the paper of Neukirch & Martens (1998), a systematic expansion procedure has been developed for force-free fields. The lowest order equations of this expansion have the same mathematical structure as the Cartesian Equations (2.28) and (2.29) with constant pressure if x is replaced by a transformed radial coordinate $\varpi = (r^2 - a^2)/2a$, where a is a radial value to be chosen, and y by θ . This expansion scheme is easily extended to include pressure gradients. The lowest order equations in this case have exactly the same mathematical structure as the Cartesian equations. Therefore, Cartesian solutions can be used to model the penumbra of sunspots and the transformation method can be applied to the lowest order solution. To see this, write the static equations in cylindrical coordinates

$$-\frac{1}{r^2} \frac{\partial^2 f}{\partial z^2} - \frac{1}{r} \frac{\partial}{\partial r} \left(\frac{1}{r} \frac{\partial f}{\partial r} \right) = \mu_0 \left(\frac{\partial p}{\partial f} \right)_\theta \quad (2.60)$$

$$\frac{1}{r^2} \frac{\partial f}{\partial r} \frac{\partial^2 f}{\partial \theta \partial r} - \frac{1}{r^2} \frac{\partial f}{\partial \theta} \frac{\partial^2 f}{\partial z^2} - \frac{1}{r} \frac{\partial f}{\partial \theta} \frac{\partial}{\partial r} \left(\frac{1}{r} \frac{\partial f}{\partial r} \right) + \frac{1}{r^2} \frac{\partial f}{\partial z} \frac{\partial^2 f}{\partial \theta \partial z} = \mu_0 \left(\frac{\partial p}{\partial \theta} \right)_f \quad (2.61)$$

Let $\varpi = \frac{r^2 - a^2}{2a}$. If the radial extent of the penumbra is $2R_p$ we expect the parameter $\epsilon = R_p/a$ to be less than 1. Then the static equations become

$$-\frac{1}{a^2(1 + 2\epsilon\varpi/R_p)} \frac{\partial^2 f}{\partial z^2} - \frac{1}{a^2} \frac{\partial^2 f}{\partial \varpi^2} = \mu_0 \left(\frac{\partial p}{\partial f} \right)_\theta \quad (2.62)$$

$$\frac{1}{a^2} \frac{\partial f}{\partial \varpi} \frac{\partial^2 f}{\partial \theta \partial \varpi} - \frac{1}{a^2(1 + 2\epsilon\varpi/R_p)} \frac{\partial f}{\partial \theta} \frac{\partial^2 f}{\partial z^2} - \frac{1}{a^2} \frac{\partial f}{\partial \theta} \frac{\partial^2 f}{\partial \varpi^2} + \frac{1}{a^2(1 + 2\epsilon\varpi/R_p)} \frac{\partial f}{\partial z} \frac{\partial^2 f}{\partial \theta \partial z} = \mu_0 \left(\frac{\partial p}{\partial \theta} \right)_f \quad (2.63)$$

If we now expand p and f in ϵ

$$p = \sum_{n=0}^{\infty} \epsilon^n p^{(n)}(\varpi, \theta, z) \quad (2.64)$$

$$f = \sum_{n=0}^{\infty} \epsilon^n f^{(n)}(\varpi, \theta, z) \quad (2.65)$$

then to lowest order in ϵ these become the Cartesian equations with $\varpi = x$, $\theta = y$ and $z = z$.

Again the most useful solution is given by Equation (2.35). We will first use the freedom of choosing the function $g_1(\theta)$ to generate a static solution which mimics the basic observational features of a fluted penumbra. Having achieved this we will transform this static solution into a solution with flow.

For this application we need to retain both $g_1(\theta)$ and $g_2(\theta)$ in the solution to have sufficient flexibility although, from Equation (2.38) we have freedom to choose only one of these on which choice the other is fixed up to a constant. The magnetic field components are now

$$B_r = k \left(g_1(\theta) \sin(\sqrt{k^2 + p_2(\theta)}\varpi) + \sqrt{1/(k^2 + p_2(\theta)) - g_1(\theta)^2} \cos(\sqrt{k^2 + p_2(\theta)}\varpi) \right) \exp(-kz) \quad (2.66)$$

$$B_\theta = 0 \quad (2.67)$$

$$B_z = \sqrt{k^2 + p_2(\theta)} \left(g_1(\theta) \cos(\sqrt{k^2 + p_2(\theta)}\varpi) - \sqrt{1/(k^2 + p_2(\theta)) - g_1(\theta)^2} \sin(\sqrt{k^2 + p_2(\theta)}\varpi) \right) \exp(-kz) \quad (2.68)$$

which can be rewritten as

$$\mathbf{B} = (k\text{Im}(A), 0, \sqrt{k^2 + p_2(\theta)}\text{Re}(A)) \quad (2.69)$$

where

$$A = \left(g_1(\theta) + i \sqrt{\frac{1}{k^2 + p_2(\theta)} - g_1(\theta)^2} \right) \exp(i\sqrt{k^2 + p_2(\theta)}\varpi) \exp(-kz). \quad (2.70)$$

We start from the observation (e.g. Degenhardt & Wiehr, 1991, Title et al., 1993) that the inclination of the magnetic field with vertical in the plane $z = 0$ varies rapidly with θ around an average inclination which increases from about $40^\circ - 50^\circ$ at the inner penumbral boundary to $70^\circ - 75^\circ$ at the outer penumbral boundary. If we begin by setting $p_2(\theta) = 0$ (so that the pressure is constant) then we can fix the field line inclination of solution (2.66) - (2.68) as follows. The field line inclination from the vertical in this case is given by

$$\delta = \text{Arg}(A) = k\varpi + \arctan \sqrt{\frac{1}{k^2 g_1(\theta)^2} - 1} \quad (2.71)$$

which consists of an r -dependent part and a θ -dependent part. The r -dependence can be fixed by considering the desired average inclination at the inner and outer penumbral boundaries δ_{in} and δ_{out} :

$$\delta_{out} - \delta_{in} = k(\varpi_{out} - \varpi_{in}) = k \left(\frac{r_{out}^2 - r_{in}^2}{2a} \right). \quad (2.72)$$

This fixes one of a and k when we have chosen the other. We choose the angular variation to vary sinusoidally with θ by setting

$$\arctan \sqrt{\frac{1}{k^2 g_1(\theta)^2} - 1} = \delta_0 + \delta_{mod} \sin(m\theta). \quad (2.73)$$

Now we can fix δ_0 with either of $\delta_{out} = k\varpi_{out} + \delta_0$ or $\delta_{in} = k\varpi_{in} + \delta_0$ which are consistent with each other. The amplitude of angular variation δ_{mod} can then be chosen to fit observation.

We can now re-introduce a pressure gradient in the z -direction by making $p_2(\theta)$ non-zero. Figures 2.3, 2.4 and 2.5 were all generated by fixing the penumbral field line structure to be flatter than desired while the pressure was constant and then afterwards introducing a pressure gradient to give the field lines approximately the desired inclination. We chose the radial parameter a to be $a = 0.8$. Figures 2.4 and 2.5 show that the field lines of smallest inclination to the vertical reach relatively large heights before returning to the photosphere. We can change this by altering the pressure gradient via $p_2(\theta)$.

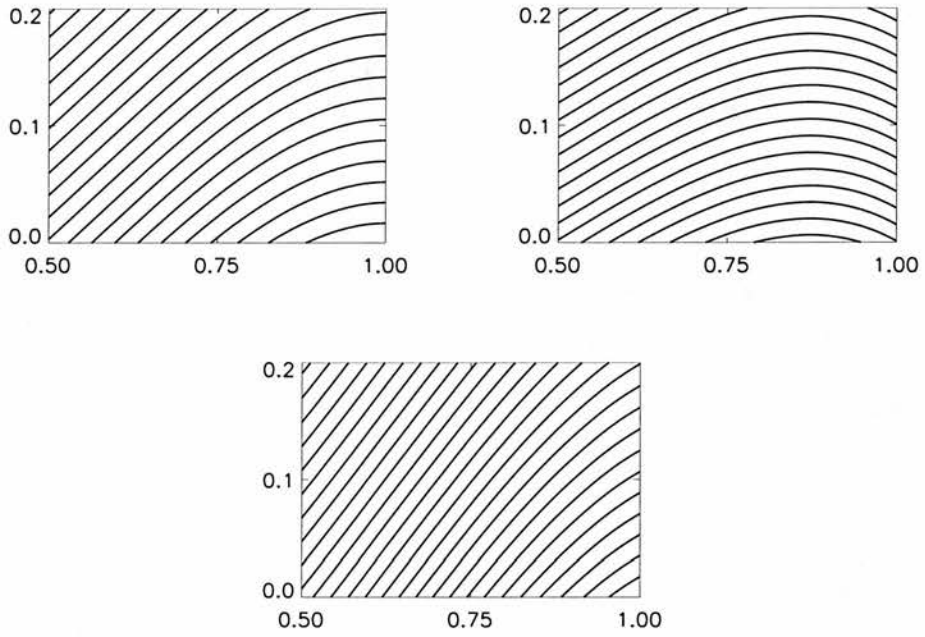


Figure 2.3: Pictured are slices through the approximate sunspot-like solution (2.66)-(2.68) at three different constant values of θ . Top picture: field lines of average inclination to the vertical. Middle: field lines highly inclined with respect to the vertical. Bottom: field lines of low inclination.

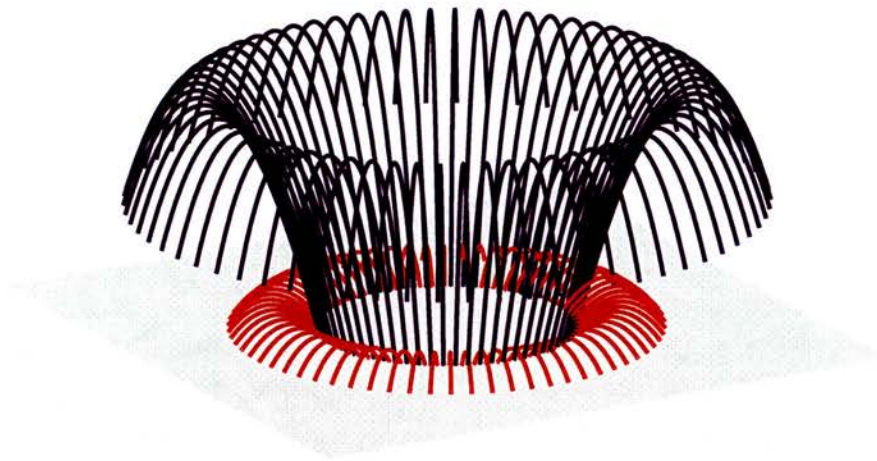


Figure 2.4: Most- and least-inclined field lines through $r = 0.6$ at $z = 0$ of solution (2.66)-(2.68) with $p_2 = 0.5$. The plasma flow speed is colour-coded as in Figure 2.1. Note that Figure 2.4 shares a colour table with Figure 2.5 and flow velocity minima (green) or maxima (red) may not be represented in both Figures 2.4 and 2.5. This figure gives an impression of what the solution looks like as a whole. Over a full rotation in the θ direction, the field line inclination alternates $m = 66$ times between high and low inclination. The colour-coding shows that the plasma flow is confined to low-lying field lines.

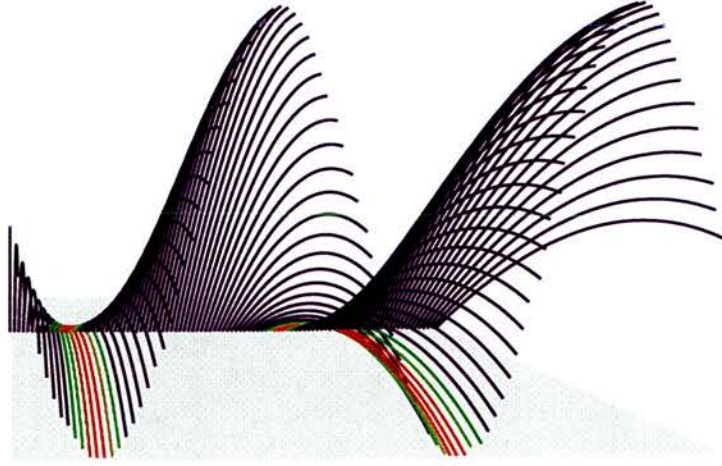


Figure 2.5: Most- and least-inclined field lines through $r = 0.6$ at $z = 0$ over two wavelengths in θ for solution (2.66)-(2.68) with $p_2 = 0.5$. The plasma flow speed is colour-coded as in Figure 2.1. Figure 2.5 shows the sinusoidal variation in θ chosen for resemblance to a “fluted” penumbra. The colour-coding indicates the distribution of flow speed among the lowest-lying field lines.

2.5.3 Solutions in cylindrical coordinates

As already mentioned several times, solutions in cylindrical coordinates are most useful to model sunspot-like fields. The known solutions in cylindrical coordinates are, however, only partially useful because they are not bounded functions of space. We therefore have to restrict our analysis to a finite spatial domain, assuming that we have prescribed appropriate boundary conditions at the boundary of the domain. Due to these restrictions we can also only expect to find solutions which have the same general topological features as the observed sunspots but not models which match every observational detail.

The static solution we choose is given in Equation (2.44). The corresponding magnetic field which is non-singular on the z -axis ($b = 0$) is given by

$$B_r = -\frac{1}{2}cr \quad (2.74)$$

$$B_\theta = 0 \quad (2.75)$$

$$B_z = \frac{1}{2}p_1(\theta)r^2 + cz + d. \quad (2.76)$$

This solution has two free parameters, c and d , and a free function $p_1(\theta)$. We use this freedom to generate a fluted field.

Choosing without loss of generality to model a sunspot with positive polarity, we must have B_z positive in the spot at $z = 0$. In particular this must be true on the axis $r = 0$ where $B_z = d$ for $z = 0$ and thus we must choose d to be positive. We see that the physical meaning of the parameter d is the value of B_z at the centre of the spot at level $z = 0$.

If we take a look at Equation (2.74) we see that the parameter c determines the sign of B_r . Since the magnetic field should point outward from the spot centre we must choose $c < 0$ so that $B_r > 0$ for $r > 0$.

A second look at Equation (2.76) reveals one of the shortcomings of the present solution. Clearly for sufficiently large z ($z > -d/c$), B_z becomes negative and the vertical field direction reverses. This happens at a magnetic null point on the z -axis and we have separatrix surfaces associated with this null point separating domains of different magnetic topology from each other. Our model can only be considered valid in a region below the critical value $z_{lim} = -d/c$ at $r = 0$ and below the separatrix surface in general.

In order to mimic a fluted penumbra we choose B_z to vary sinusoidally with azimuthal angle θ . For example, we let

$$p_1(\theta) = \bar{a} + \bar{a}_1 \sin m\theta \quad (2.77)$$

where \bar{a} , \bar{a}_1 and azimuthal wavenumber m are constants to be chosen.

Denoting by r_{out} the radius of the outer penumbral boundary and by r_{in} the radius of the inner penumbral boundary, we can fix the average field line inclination angle at r_{out} and r_{in} to be what we want by choosing the value of \bar{a} appropriately. The field line inclination takes its average value where $\sin m\theta = 0$ and so $p_1(\theta) = \bar{a}$. Denoting by ϕ_{out} the average field line inclination angle from the vertical at $r = r_{out}$, $z = 0$, ϕ_{out} is defined by

$$\tan \phi_{out} = \frac{\frac{1}{2}|c|r_{out}}{\frac{1}{2}\bar{a}r_{out}^2 + d} \quad \left(= \frac{B_r}{B_z} \right). \quad (2.78)$$

Solving this for \bar{a} we obtain

$$\bar{a} = \frac{1}{r_{out}^2} \left(\frac{|c|r_{out}}{\tan \phi_{out}} - 2d \right). \quad (2.79)$$

In order to proceed further, we need additional information on the sign of \bar{a} and \bar{a}_1 . We can actually get this information from recent observations (Westendorp-Plaza et al., 1997) which show that some magnetic flux returns to the photosphere just outside the outer penumbral boundary. If we want to include this feature in our model, we have to assume that B_z (for our purpose here it is sufficient to look just at $z = 0$) changes its sign at some value of $r \geq r_{out}$ at least for the flatter (more inclined) field lines. Within our model this can only happen if $p_1(\theta)$ becomes negative for at least some θ . It turns out that for the parameter values we will choose both \bar{a} and \bar{a}_1 are negative.

We now proceed by looking at a field line with the largest inclination (smallest B_z because B_r does not change with θ) at the outer penumbral boundary. The inclination angle ϕ_{max} is given by

$$\tan \phi_{max} = \frac{\frac{1}{2} |c| r_{out}}{\frac{1}{2} (\bar{a} + \bar{a}_1) r_{out}^2 + d}. \quad (2.80)$$

Solving this equation for \bar{a}_1 , we get

$$\bar{a}_1 = \frac{1}{r_{out}^2} \left(\frac{|c|r_{out}}{\tan \phi_{max}} - 2d \right) - \bar{a}. \quad (2.81)$$

By substituting Equation (2.79) into Equation (2.81) we obtain

$$\bar{a}_1 = \frac{|c|}{r_{out}} \left(\frac{1}{\tan \phi_{max}} - \frac{1}{\tan \phi_{out}} \right). \quad (2.82)$$

One immediately sees that \bar{a}_1 is indeed negative as long as ϕ_{max} is bigger than ϕ_{min} .

If we denote by ϕ_{in} the average field line inclination angle from the vertical at $r = r_{in}$, $z = 0$, then ϕ_{in} is defined by

$$\tan \phi_{in} = \frac{\frac{1}{2} |c| r_{in}}{\frac{1}{2} \bar{a} r_{in}^2 + d}. \quad (2.83)$$

Solving this for \bar{a} we have

$$\bar{a} = \frac{1}{r_{in}^2} \left(\frac{|c|r_{in}}{\tan \phi_{in}} - 2d \right). \quad (2.84)$$

We can use Equations (2.79) and (2.84) to obtain d :

$$d = \frac{|c|}{2} \frac{r_{out}^2 r_{in}^2}{r_{out}^2 - r_{in}^2} \left(\frac{1}{r_{in} \tan \phi_{in}} - \frac{1}{r_{out} \tan \phi_{out}} \right). \quad (2.85)$$

Consistently with our assumption of a positive polarity spot, d is positive. We see that the modulus of c determines the value of the parameter d , equivalent to the strength of the z -component of the magnetic field at the spot centre. Once $c < 0$ is chosen, the parameter d is given in terms of parameters whose values can be taken from observations. Having calculated d , we can use this to calculate \bar{a} by using (2.79) or (2.84). The result is

$$\bar{a} = \frac{|c|}{r_{out}^2 - r_{in}^2} \left(\frac{r_{out}}{\tan \phi_{out}} - \frac{r_{in}}{\tan \phi_{in}} \right) \quad (2.86)$$

For realistic parameter values \bar{a} again is always negative as already mentioned before. Our solution (2.74)-(2.76) is then completely defined to match the basic features of the observations. By similar reasoning we can generate a negative-polarity sunspot matching the observational features discussed (choose $c > 0$, $d < 0$ and replace $|c|$ with $-|c|$ in the above).

As an example we chose the outer penumbral boundary to be normalised $r_{out} = 1.0$ and the inner penumbral boundary to be at $r_{in} = 0.5$. The average inclination angle at the inner and outer boundaries are chosen to be $\phi_{in} = 50^\circ$ and $\phi_{out} = 70^\circ$. The maximum inclination angle at the outer boundary is chosen to be $\phi_{max} = 88^\circ$. We choose the azimuthal wavenumber m to be 66 in accordance with Martens et al. (1996) and Neukirch & Martens (1998). With this choice of parameter values, the highly-inclined (flatter) field lines reach a polarity inversion line and return to the photosphere while the less-inclined lines continue upwards as far as the model can be considered valid. (There is some indication of this in Figure 2.6.)

One additional feature of the solution which appears naturally is that the highly-inclined (flat) field lines actually return to the photosphere ($z = 0$) just outside the outer penumbral boundary, in agreement with recent observations by Westendorp-Plaza et al. (1997) (see also Stanchfield II et al., 1997). This can be seen in Figure 2.7.

Having generated our static solution with a fluted penumbra the next step is to transform this static solution to a steady solution with flow. As in the previous cases we do this by prescribing M as a function of f and θ appropriately. To match the basic observations (e.g. Rimmele, 1995a, 1995b, Shine et al., 1994) we want to concentrate flow to field lines that a) emerge from the photosphere close to the inner penumbral

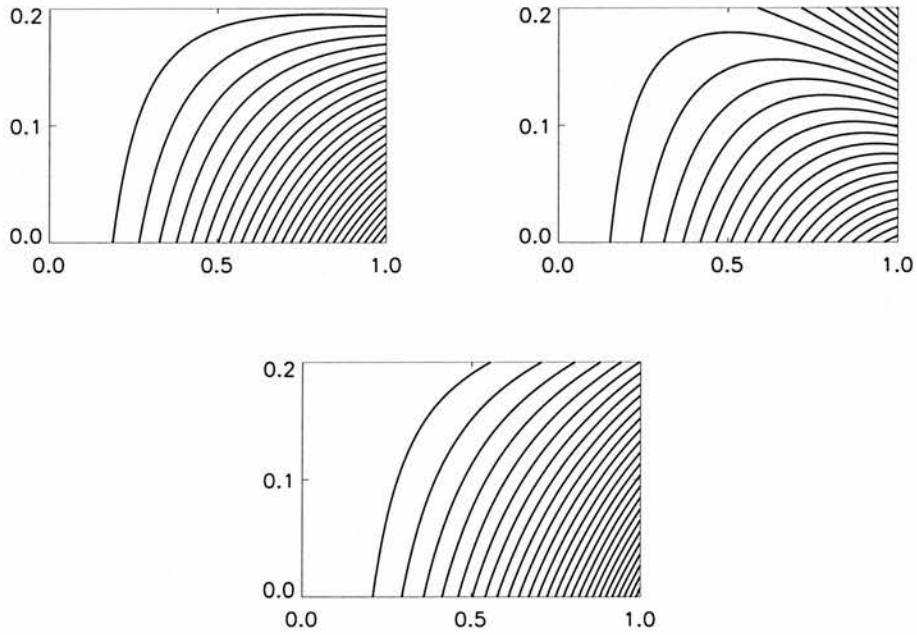


Figure 2.6: Pictured are slices through the exact sunspot-like solution (2.74)-(2.76) at three different constant values of θ . Top picture: field lines of average inclination to the vertical. Middle: field lines highly inclined with respect to the vertical. Bottom: field lines of low inclination. As well as the solution's resemblance to a sunspot, this figure also shows the high field strength far from the umbra.

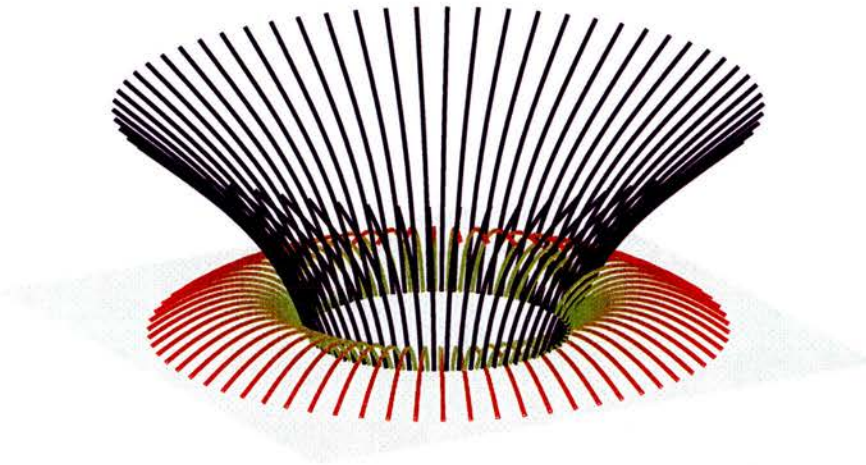


Figure 2.7: Most- and least-inclined field lines through $r = 0.6$ at $z = 0$ of solution (2.74)-(2.76). The plasma flow speed is colour-coded as in Figure 2.1. Note that Figure 2.7 shares a colour table with Figure 2.8 and flow velocity minima (green) or maxima (red) may not be represented in both Figures 2.7 and 2.8. This figure gives an impression of what the solution looks like as a whole. Over a full rotation in the θ direction, the field line inclination alternates $m = 66$ times between high and low inclination. The colour-coding shows that the plasma flow is confined to low-lying field lines and accelerates from the centre outwards.

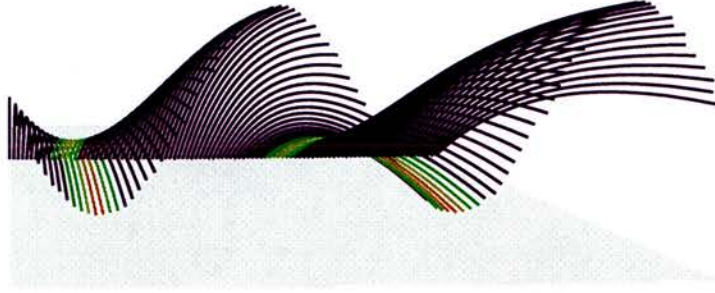


Figure 2.8: Most- and least-inclined field lines through $r = 0.6$ at $z = 0$ over two wavelengths in θ of solution (2.74)-(2.76). The plasma flow speed is colour-coded as in Figure 2.1. Figure 2.8 shows the sinusoidal variation in θ chosen for resemblance to a “fluted” penumbra. The colour-coding indicates the distribution of flow speed among the lowest-lying field lines.

boundary and b) are highly inclined with respect to the vertical, i.e. flat. A particular choice for M satisfying these two conditions is

$$M^2 = \frac{M_0^2}{\cosh^2\left(\frac{f(r, \theta, z) - f_0}{\Delta f}\right) \cosh^2\left(\tan^2\left(\frac{m}{2}\theta - \frac{3\pi}{4}\right)\right)}, \quad (2.87)$$

with $M_0^2 < 1$ to ensure sub-alfvénic flow speed. This choice for M ensures that the flow is concentrated to field lines having f values close to f_0 and θ values close to $3\pi/(2m)$. In the Figures 2.7 and 2.8 we have chosen $f_0 = f(0.6, 3\pi/2m, 0)$, thus concentrating the flow to field lines which emerge from the photospheric level ($z = 0$) at $r = 0.6$ and $\theta = 3i\pi/2m$ ($i = 1, \dots, m$) i.e. close to the inner penumbral boundary $r = 0.5$ and where $p_1(\theta)$ takes its minimum value $\bar{a} - \bar{a}_1$. M is $2\pi/m$ -periodic in θ and so concentrates \mathbf{v} to every flat-lying field line through $r = 0.6$ at $z = 0$. The coefficient M_0^2 in these figures has been chosen as $1/2$ ensuring that the Alfvén Mach number is $1/\sqrt{2}$ on flow lines so that the transformation exists and is invertible. Finally we choose the sign of σ to ensure that the plasma flow is outward whether the sunspot polarity is positive or negative.

From the generalised pressure function

$$\Pi = p + \frac{1}{2}\rho v^2 \quad (2.88)$$

and the gas pressure function

$$p = p_0 - p_1(\theta)f - \frac{1}{2}\rho(f, \theta)\sigma^2(f, \theta)|\mathbf{B}|^2 \quad (2.89)$$

we can give a little physical background to the Evershed flow in the solution. From equation (2.89), $p|_{z=0, \theta=\text{const}}$ decreases as r increases and so there is a difference in the gas pressure at each of the footpoints of a flow line although Π and ρ are constant on each flow line. Therefore, from Equation (2.88), $|\mathbf{v}|$ has to increase as we move out from the centre along a flow line. This physical interpretation of the Evershed flow is similar to the siphon flow models (e.g. Thomas, 1995).

Along field lines with little or no flow, the transformed magnetic field of the flow solution is (almost) identical to that of the static solution. Along field lines with significant flow, the magnetic field becomes $1/\sqrt{1-0.5^2} = 2/\sqrt{3}$ times as strong as the corresponding static field. The basic global topology of the magnetic field remains unaffected by the transformation.

We can choose a second static solution in cylindrical coordinates (r, θ, z) from Kaiser & Salat (1997) to generate another sunspot-like solution. This solution, whose field lines lie on surfaces $\theta = \text{constant}$, has magnetic field components given by

$$B_r = -\frac{1}{r}c_1 \sin\left(\frac{1}{2}kr^2\right) \quad (2.90)$$

$$B_\theta = 0 \quad (2.91)$$

$$B_z = k(b_1 + c_1z) \cos\left(\frac{1}{2}kr^2\right) - kb_2(\theta) \sin\left(\frac{1}{2}kr^2\right) \quad (2.92)$$

The solution has three free parameters, b_1 , c_1 and k , and a free function $b_2(\theta)$. We use this freedom to generate a fluted, sunspot-like field exactly as discussed above for solution (2.74)-(2.76) and a very similar field results here. Observations indicate that Evershed flow speed accelerates away from the inner penumbral boundary while magnetic field strength decreases with distance from the umbra. Note that we cannot model both of these properties here as $|\mathbf{v}| \propto |\mathbf{B}|$. We still have enough freedom with

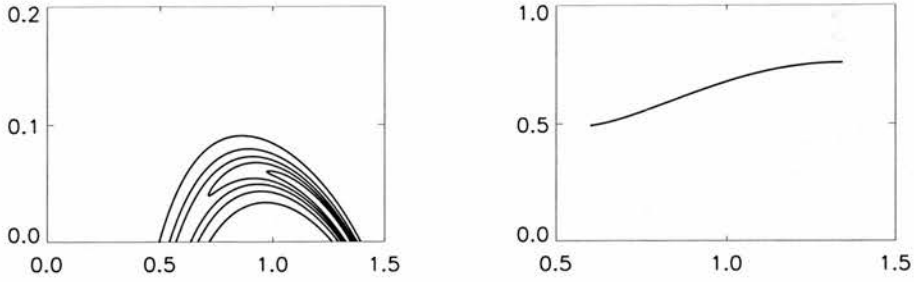


Figure 2.9: Exact sunspot-like solution (2.90)-(2.92): the left picture shows a contour plot of the flow velocity profile in the penumbra. It can be seen that Evershed flow is concentrated to those field lines in planes $\theta = \frac{3\pi}{2m}$ through $(r, z) = (0.6, 0)$ as required to model observed Evershed flows. The right picture shows the flow velocity amplitude profile along a field line of maximum flow in the penumbra.

our parameters to choose the flow speed to reach its maximum precisely on returning to $z = 0$ (see Figure 2.9).

2.6 Discussion and Conclusion

In the present chapter we have for the first time applied a transformation method (Grad, 1960; Gebhardt and Kiessling, 1992) to three-dimensional static MHD equilibria and have thus calculated classes of solutions of the stationary three-dimensional MHD equations with field-aligned incompressible flow. In our use of static MHD equilibria we have chosen those solutions which seemed to be most suitable as models for flows in solar coronal arcades and sunspots. To the knowledge of the author the presented solutions are the first self-consistent exact solutions of the stationary MHD equations with flow apart from very few special solutions which were previously known.

Unfortunately, only very few exact three-dimensional MHD equilibria are known and of these only a much smaller sub-class is suitable for a straightforward application of the transformation method. Also the transformation method is restricted to field-aligned incompressible flow. These limitations are reflected in the shortcomings that some of the presented solutions necessarily have if critically examined as models of

solar magnetic structures. Although finding exact solutions of a set of complicated equations as the steady state MHD equations is very pleasing from a mathematical point of view and also certainly rewarding from a physical point of view, the deficiencies of the solutions regarding their value as models of solar magnetic structures can only be remedied by relaxing some of the restrictive assumptions made in the present chapter. This leads us to the discussion of possible future work extending the present analysis.

One possibility to generalize the present work is to relax the assumption of incompressible flow and allow for compressible flow. Since the mathematical complexity of the equations is much larger in this case, no equivalent of the transformation method is known for the compressible case, and the only possible approach is to study special simple cases using other methods (see e.g. Imai, 1960, and Webb et al., 1994 for a method based on an analogy between field-aligned compressible MHD flows and compressible irrotational steady flows in ordinary fluid dynamics which has so far been only applied to symmetric equilibria).

The other assumption which needs to be relaxed at least for some solar applications is the neglect of an external gravitational field. In Appendix A we give two extensions of the Gebhardt & Kiessling transformation method: one transforming from static 3D MHD without gravity to 3D MHD with steady field-aligned incompressible flow and gravity, and the other transforming from static 3D MHD with gravity to 3D MHD with steady incompressible field-aligned flow and gravity. We are not able to apply the second of these extended transformations as we are not aware of any three-dimensional static equilibria for which this transformation is applicable. In principle, we could have included an external gravitational field in the analysis presented in this chapter using the first extended Gebhardt & Kiessling (1992) transformation given in Appendix A by transforming from our familiar static equilibria without gravity. We have refrained from doing so for two reasons: a) including an external gravitational field would have only affected the form of the transformed plasma pressure as a function of space, not the form of the magnetic field and b) we would have to use a relation between pressure and density which could lead to unphysical negative values of the pressure. Both of these points are due to the assumption of incompressible flow which does not allow for a general stratification of the pressure and the density whereas the gravitational force is

acting to establish such a stratification. We have therefore postponed the inclusion of external gravity to cases with compressible flow which we eventually want to find.

An important final point we need to mention is the stability of the presented solutions. The stability of none of the solutions presented here has been tested. This is another important point for future work. However, though the methods for assessing the stability or instability of static equilibria are well established (see e.g. Lifschitz, 1989) they are far from simple to apply to specific equilibria. To our knowledge only a vanishingly small number of three-dimensional equilibria has ever been tested for stability (e.g. Chou et al., 1993; Longbottom et al., 1994). The situation is even worse for stationary solutions with flow because even though methods such as the energy principle have been extended to solutions with steady flow there is an ongoing debate about the usefulness of the derived principles because most of them lead to functionals having a saddle point structure instead of being bounded from below as in the static case (e.g. Hameiri 1998). An interesting but yet unsolved question is whether the transformation method we used to calculate the stationary solutions with steady flow has any consequences for the stability problem, i.e. if the stability properties of a static equilibrium have been investigated, does this have any implications for the stability properties of the transformed solution ? Again, the answer of this question is beyond the scope of this chapter and will be left for future work. An attempt at this was made for the static case of one of the equilibria of Chapter 2, borrowing from the successful investigation of a different three-dimensional MHS equilibrium by Chou et al. (1993) (despite mathematical errors in their calculation of the energy integral) and by Longbottom et al. (1994) using a general technique by Longbottom et al. (1993). Although some progress has been achieved, this work suggests that an analytical treatment using an energy method may be intractable since there are more cross-field derivatives to consider with our solutions than with the one considered by Chou et al. (1993) and Longbottom et al. (1994), and even if these were to be eliminated from the problem by restricting them to a positive-definite part of the integral, the resulting Euler-Lagrange equations may reduce to a system of ordinary differential equations too cumbersome to work with. However, further simplifications to the energy integral would increase the likelihood of success and this possibility will be investigated in the future.

Chapter 3

The Green's Function Method for a Special Class of Linear 3D Static Equilibria

3.1 Introduction

Having calculated new three-dimensional equilibria with flow using a known class of static three-dimensional equilibria in the previous chapter, in this chapter we derive a Green's function method for another class of known static three-dimensional equilibria to be used in modelling structures in the solar atmosphere. The material of this chapter has been published in a shorter form in Petrie & Neukirch (2000).

Observations of the solar corona, especially in X-rays and EUV, show that its spatial and temporal structure is dominated by the coronal magnetic field. The determination of the magnetic field structure in the solar corona is therefore a prime task of solar physics. However, the coronal magnetic field cannot be measured directly with present techniques. Hence the coronal magnetic field has to be calculated by extrapolation from data taken at photospheric level. Although modern instruments allow measurement of the photospheric magnetic field, horizontal (i.e. parallel to the photosphere) measurements have large uncertainty margins and a 180° ambiguity in direction. These

measurements provide boundary values for the problem of determining the magnetic field in the corona above the photosphere. The photospheric field is not force-free but becomes approximately force-free about 400km above the photosphere. Since the magnetic observations are made where the field is not force-free it seems necessary to model the photospheric region in order to deduce the magnetic field at the base of the corona and go on to use this as the starting point for extrapolation. However, the radiative transfer and the inhomogeneity of density and temperature in the photosphere is very difficult to model. Fortunately the photosphere is very thin compared to the horizontal extent of an active region and \mathbf{B} , being divergence-free, will not vary much through the photosphere. Therefore the photospheric magnetic field is often used as a boundary condition. Any extrapolation method relies on assumptions about the electric current density in the corona. Existing extrapolation methods include potential (e.g. Schmidt, 1964; Semel, 1967; Schatten et al., 1969; Altschuler & Newkirk, 1969), linear force-free (e.g. Chiu & Hilton 1977; Alissandrakis 1981; Semel 1988; Gary 1989) and nonlinear force-free fields (e.g. Sakurai, 1981; Wu et al., 1985; Aly, 1989; McClymont & Mikic, 1994; Roumeliotis, 1996; Amari et al., 1997; McClymont et al., 1997; Lee et al., 1999). Details of the various methods for magnetic field reconstruction and discussion of their relative merits can be found in the review papers of e.g. Amari & Démoulin (1992), Démoulin et al. (1997), McClymont et al. (1997) and Amari et al. (1997).

The simplest physical assumption possible is to assume that the system is current-free, i.e. the magnetic field is a potential field. Implementing this assumption only requires the line-of-sight photospheric magnetic field as a boundary condition. This procedure is well-understood, being a linear classical mathematical problem with a unique solution. The potential assumption is, however, not applicable to many active regions where the magnetic field is known to have stored free energy, i.e. its energy is greater than the minimum energy corresponding to the current-free configuration with the same line-of-sight magnetic field in the photosphere. The linear force-free approximation allows field-aligned electric currents directly proportional to the magnetic field, $\mathbf{j} = \alpha\mathbf{B}$ where \mathbf{j} is the current density, \mathbf{B} is the magnetic field and α is a constant. This assumption can also be implemented using only the line-of-sight photospheric magnetic field as a boundary condition in a manner very similar to potential methods, although a linear

force-free field is not uniquely determined by these boundary conditions in contrast to potential fields. Linear force-free fields can provide a good representation of the coronal field over a local area but generally does not give a good global description. Moreover observed active regions appear to have a non-uniform current distribution implying a non-constant α . Further weaknesses are that the total energy of the field in an unbounded domain is generally infinite and linear force-free fields do not become potential at great heights whereas in the solar atmosphere currents are restricted to a finite volume. Applied to active regions on the sun linear force-free fields might be expected to be useful models on small scales, in particular close to the photosphere. Because of the limitations of linear force-free field models, much effort has been devoted to calculating nonlinear force-free fields (i.e. $\mathbf{j} = \alpha\mathbf{B}$ where α is now a function of space) to match the photospheric boundary conditions. In addition to questions surrounding existence and uniqueness of solutions, nonlinear force-free methods are computationally expensive requiring many hours of computer time to calculate. For these reasons and others and despite their shortcomings linear force-free fields are often used as approximate models of coronal magnetic fields.

Apart from the well-known limitations of potential and linear force-free field reconstruction (Amari et al., 1997) a general problem of all reconstruction methods is that their success in representing the “true” coronal magnetic field is difficult to assess. The present chapter tries to address this particular problem but we do not suggest that the method presented improves upon magnetic field reconstruction in the force-free case. In our opinion the advantage of the present method over linear force-free reconstruction is the possibility of comparing the calculated model plasma properties with observations brought about by modelling in a simple way non-force-free effects close to the photosphere. This is in contrast to the usual way of assessing reconstructed magnetic field lines, which is to carry out a visual comparison of a number of field lines with the observed plasma emission patterns. In a stationary model, the only possibility of allowing for spatial variations of the plasma properties (apart from stratification by gravity) is by including currents flowing perpendicular to the magnetic field. Therefore the three-dimensional stationary plasma structures imply the existence of perpendicular currents, i.e. deviations from a force-free field. Strictly speaking, the only structuring of

the plasma allowed in a potential or force-free field is stratification by the gravitational force. Such a structure cannot match the observed emission patterns. Approaches towards overcoming this disadvantage include e.g. rendering techniques (Gary, 1997) and testing the consistency of physical properties of loops with the calculated field line structure (Lee et al., 1999).

However, in the solar corona the perpendicular currents necessary to explain most of the observed structures will be much smaller than the field-aligned currents determining the structure of the magnetic field. It turns out that in the method presented here only very small perpendicular currents are necessary to produce significant structuring of the plasma if the average plasma beta is small. In principle, one could imagine an expansion procedure in which the force-free current and the boundary conditions determine the large-scale structure of the magnetic field in the lowest order and the perpendicular currents determine the spatial structure of the plasma in the next order. A more straightforward approach is to take the perpendicular currents directly into account in the solution of the MHS equations and this is the approach we will follow in the present contribution. A non-trivial difficulty with this approach is that three-dimensional MHS equilibria have to be used and their calculation is a problem in itself. We will use a special class of analytical self-consistent three-dimensional MHS equilibria which has been discovered by Low (1985, 1991, 1992, 1993a, b) and Bogdan & Low (1986), with some additions made by Neukirch (1995, 1997a, b). A subset of this class of equilibria has already been used to model the large-scale corona globally using spherical coordinates (e.g. Bagenal & Gibson, 1991; Zhao & Hoeksema, 1993, 1994; Gibson & Bagenal, 1995). This subset can be derived by a simple transformation of potential or linear force-free solutions and has also recently been used for local smaller-scale modelling (Alexander & Gary, 1999). All other contributions using this class of MHS solutions for the purpose of modelling local coronal structures using Cartesian coordinates (e.g. Aulanier et al., 1998, 1999) rely on expansions of the solutions in discrete (normal) modes. Aulanier et al. (1998, 1999) have made use of this solution class in modelling local prominence structures using Cartesian coordinates. Our method is unique in that it uses a Green's function formulation.

Most extrapolation methods for potential and linear force-free fields are based on the

general mathematical method of Green's functions (e.g. Schmidt, 1964; Semel, 1967; Chiu & Hilton, 1977; Alissandrakis, 1981; Sakurai, 1982; Semel, 1988; Gary, 1989). Exceptions are extrapolation methods for the global solar magnetic field using (synoptic) magnetic maps of the complete solar surface where an expansion in spherical harmonics is usually used (e.g. Schatten et al., 1969; Altschuler & Newkirk, 1969; Altschuler et al., 1974, 1977). All of these methods use either the photospheric field component perpendicular to the solar surface or the line-of-sight component as input and give all magnetic field components in the complete domain as output.

The purpose of this chapter is to develop the Green's function method for the special class of MHS equilibria mentioned above. We will use the results of Neukirch & Rastätter (1999) who showed that it is possible to express the magnetic field of this solution class by a single scalar function in the same way as for the linear force-free case. This result can be used to calculate the Green's function in a way completely analogous to the linear force-free case. The use of the Green's function method allows boundary conditions to be imposed which do not have to be periodic. The method enables us to calculate not only the magnetic field, but also the plasma pressure, the plasma density and the plasma temperature from the boundary data. This makes a much better comparison of the models with the observations possible.

It is, however, necessary to mention some limitations of the models. First of all, the price we pay for an analytical description of the complex plasma-magnetic field interaction is finding the equation of state of the plasma as a result rather than having it as an a priori condition. This could lead to results which are unreasonable from a physical point of view. Furthermore, the resulting magnetic fields share the deficiencies of linear force-free fields: they cannot represent different length scales as α is constant, they are not uniquely determined by the z -component of the magnetic field on the boundary and they have infinite magnetic energy if considered in an unbounded domain. Therefore we consider these models only as a first step on the way to better and more realistic models. We believe that the disadvantages just described are more than compensated for by the possibility of an analytical treatment.

The chapter is organised in the following way. In Section 3.2 we summarize the necessary facts about the solution class used. We introduce in Section 3.3 the concept of

a Green's function and attempt to convey its power in fitting a solution to boundary data. In Section 3.4 we show how the representation of the magnetic field by a single scalar function (which we call the P-representation for short) simplifies the calculation of the Green's function. In Section 3.5, we show three particularly interesting special cases, starting with the linear force-free case as reference case. We summarize our results in Section 3.6.

3.2 The Solution Class

We are looking for three-dimensional solutions to the MHS equations (see Section 1.5)

$$\frac{1}{\mu_0}(\nabla \times \mathbf{B}) \times \mathbf{B} - \nabla p - \rho \nabla \psi = 0, \quad (3.1)$$

$$\nabla \times \mathbf{B} = \mu_0 \mathbf{j}, \quad (3.2)$$

$$\nabla \cdot \mathbf{B} = 0, \quad (3.3)$$

where p = pressure, ρ = density and $\psi = gz$ = gravitational potential. Therefore the static equilibria of this chapter differ from those of Chapter 2 in that here the effects of gravity are included. We have already emphasised in Section 1.6 of the introduction to this thesis that solutions to this set of partial differential equations varying in all three spatial directions are rare and are difficult to find. Therefore we follow Low (1991, 1992) and assume that Ampère's law has the form

$$\mu_0 \mathbf{j} = \nabla \times \mathbf{B} = \alpha \mathbf{B} + \nabla \times (F \nabla \psi) \quad (3.4)$$

where F is arbitrary, with the constraint that ∇F and $\nabla \psi$ have to be linearly independent vector fields, and α is constant (n.b. Equation (3.3) immediately follows). The last term is the link between the magnetic field and the plasma (if $F = 0$ the field is force-free). Using this special form for the current density the force-balance equation Equation (3.1) has only two components: in the ∇F and $\nabla \psi$ directions. Let $F = K(\psi) \mathbf{B} \cdot \nabla \psi$, where $K(\psi)$ is a free function, so that these two components can be integrated:

$$p = p_0(\psi) - \frac{1}{2\mu_0 K(\psi)} F^2 \quad (3.5)$$

$$\rho = -\left(\frac{\partial p}{\partial \psi}\right)_F + \frac{1}{\mu_0} \mathbf{B} \cdot \nabla F. \quad (3.6)$$

In Cartesian coordinates we have $\psi = gz$ and $F = \frac{1}{g}\xi(z)B_z$ where $\xi(z)$ is a function to be defined. We can then obtain a linear equation for B_z from the z -component of the curl of Ampère's Law (Neukirch 1995)

$$\Delta B_z + \alpha^2 B_z - \xi(z) \left[\frac{\partial^2 B_z}{\partial x^2} + \frac{\partial^2 B_z}{\partial y^2} \right] = 0. \quad (3.7)$$

The coefficients of this equation do not depend on x and y . Therefore we can Fourier transform Equation (3.7) in the x - and y -directions,

$$B_z(x, y, z) = \iint \tilde{B}_z(k_x, k_y, z) e^{i(k_x x + k_y y)} dk_x dk_y \quad (3.8)$$

and obtain a Schrödinger equation

$$\frac{d^2 \tilde{B}_z}{dz^2} + [\alpha^2 - k^2 + k^2 \xi(z)] \tilde{B}_z = 0 \quad (3.9)$$

and so we know that if $\xi(z)$ is of a recognised form we can solve for B_z explicitly. However the problem remains to solve the other components of Ampère's Law. Substituting Equation (3.8) into Equation (3.4) gives

$$ik_y \tilde{B}_z - \frac{d}{dz} \tilde{B}_y = \alpha \tilde{B}_x + ik_y \xi(z) \tilde{B}_z \quad (3.10)$$

$$\frac{d}{dz} \tilde{B}_x - k_x \tilde{B}_z = \alpha \tilde{B}_y - ik_x \xi(z) \tilde{B}_z \quad (3.11)$$

$$ik_x \tilde{B}_y - ik_y \tilde{B}_x = \alpha \tilde{B}_z \quad (3.12)$$

Solving Equations (3.10,3.11) for \tilde{B}_x and \tilde{B}_y in terms of \tilde{B}_z gives

$$\tilde{B}_x = \frac{i}{k_x^2 + k_y^2} (k_x \frac{d}{dz} + k_y \alpha) \tilde{B}_z \quad (3.13)$$

$$\tilde{B}_y = \frac{i}{k_x^2 + k_y^2} (k_y \frac{d}{dz} - k_x \alpha) \tilde{B}_z \quad (3.14)$$

so that Equation (3.12) is also satisfied. This suggests that the components $B_i(x, y, z)$ are linked by a function $P(x, y, z)$ with $\tilde{B}_z = (k_x^2 + k_y^2) \tilde{P}$, which is precisely the structure of MHS equilibrium treated by Neukirch & Rastätter (1999). The force-free Green's-function solution described by Chiu & Hilton (1977) also has this structure (see Equations (14-16) of that paper). Chiu & Hilton (1977) use a well-known representation for solenoidal vector fields often used for force-free fields (see e.g. Chandrasekhar, 1961; Nakagawa & Raadu, 1972) which allows them to calculate the magnetic field components by solving a single scalar equation, the Helmholtz equation, before using an eigenfunction expansion method to derive their Green's function solution. Neukirch & Rastätter (1999) show how this special representation for the magnetic field reveals an intrinsic relationship between linear force-free fields and our special class of MHS fields. Such a link therefore opens up the possibility of reducing the problem of solving all three components of Equation (3.4) for the three magnetic field components to that of solving a single scalar equation for P , as described by Neukirch & Rastätter (1999), and of using its solution to derive a Green's function solution to Equations (3.1-3.3). We will summarise the method of Neukirch & Rastätter (1999) before applying it to deriving such a solution.

The advantage of using this representation for \mathbf{B} is that we can reduce the problem of calculating the complete field to that of solving one equation for the scalar quantity P , as will be seen. We guarantee $\nabla \cdot \mathbf{B} = 0$ by using the following representation for \mathbf{B} (c.f. Nakagawa & Raadu, 1972)

$$\mathbf{B} = \nabla \times (\nabla \times (P\hat{\mathbf{z}}) + T\hat{\mathbf{z}}). \quad (3.15)$$

The two components are called the poloidal and toroidal components respectively since, for axisymmetric fields of this form for which neither P nor T depends on the azimuth angle, a toroidal field of this type is aligned in the azimuthal direction and circles the z -axis while a poloidal field of this type is orthogonal to the azimuthal direction and is confined to meridional planes. But P and T are not unique. We get the same magnetic

field \mathbf{B} from another set of functions $P' = P + \Phi$ and $T' = T + \Psi$, if

$$\begin{aligned}\nabla \times \nabla \times (\Phi \mathbf{e}_z) + \nabla \times (\Psi \mathbf{e}_z) &= 0 \quad \implies \\ \nabla(\nabla \cdot (\Phi \mathbf{e}_z)) - \mathbf{e}_z \Delta \Phi + \nabla \Psi \times \mathbf{e}_z &= 0\end{aligned}\quad (3.16)$$

Then the z -component of the gauge condition (3.16) is

$$\frac{\partial^2 \Phi}{\partial x^2} + \frac{\partial^2 \Phi}{\partial y^2} = 0 \quad (3.17)$$

with the solution

$$\Phi = \Re(f(x + iy, z)) \quad (3.18)$$

where $f(u, z)$ is an analytic function of $u = x + iy$. The other two components of the gauge condition are

$$\nabla_2 \Psi \times \mathbf{e}_z + \nabla_2 \frac{\partial \Phi}{\partial z} = 0 \quad (3.19)$$

where $\nabla_2 = \mathbf{e}_x \partial / \partial x + \mathbf{e}_y \partial / \partial y$. Now $\partial \Phi / \partial z$ is also an analytic function and the two components of the gauge condition are

$$-\frac{\partial \Psi}{\partial y} = \frac{\partial}{\partial x} \left(\frac{\partial \Phi}{\partial z} \right) \quad (3.20)$$

$$\frac{\partial \Psi}{\partial x} = \frac{\partial}{\partial y} \left(\frac{\partial \Phi}{\partial z} \right). \quad (3.21)$$

These are the Cauchy-Riemann equations for Ψ and $\partial \Phi / \partial z$ and we conclude that

$$\Psi = -\Im \left(\frac{\partial f}{\partial z} \right). \quad (3.22)$$

So Φ and Ψ are determined up to an arbitrary analytic function $f(x + iy, z)$.

We will now use this result to derive the equations that P and T have to satisfy in the case of linear non-force-free fields. Because

$$\begin{aligned}\nabla \times \mathbf{B} &= \nabla \times [\nabla(\nabla \cdot (P \mathbf{e}_z)) - \mathbf{e}_z \Delta P] + \nabla \times \nabla \times (T \mathbf{e}_z) \\ &= \nabla \times (-\mathbf{e}_z \Delta P) + \nabla \times \nabla \times (T \mathbf{e}_z) \\ &= \nabla \times (\nabla \times (\alpha P \mathbf{e}_z)) + \nabla \times (\alpha T \mathbf{e}_z) + \nabla \times (F \nabla \psi) \\ &= \alpha \mathbf{B} + \nabla \times (F \nabla \psi)\end{aligned}\quad (3.23)$$

we get

$$-\nabla \times [(\alpha T + \Delta P + gF) \mathbf{e}_z] + \nabla \times \{\nabla \times [(T - \alpha P) \mathbf{e}_z]\} = 0. \quad (3.24)$$

This is the same equation as for the gauge functions Φ and Ψ so that we can set

$$-\alpha T - \Delta P - gF = \Im\left(\frac{\partial f}{\partial z}\right) \quad (3.25)$$

$$T - \alpha P = \Re(f). \quad (3.26)$$

We can most easily solve Ampère's law by letting $f = 0$ so that

$$T = \alpha P, \quad \Delta P + \alpha^2 P + gF = 0 \quad (3.27)$$

Now if we simplify the force-balance Equation (3.1) equation by letting

$$F = \frac{1}{g}\xi(z)B_z \quad (3.28)$$

with $\xi(z)$ arbitrary, Equation (3.27) becomes (see Neukirch & Rastätter, 1999)

$$\Delta P + \alpha^2 P - \xi(z) \left[\frac{\partial^2 P}{\partial x^2} + \frac{\partial^2 P}{\partial y^2} \right] = 0 \quad (3.29)$$

and we have reduced the problem to solving the scalar equation Equation (3.29) for P .

Now we can relate the scalar quantity P to the magnetic field via

$$\begin{aligned} B_z &= - \left(\frac{\partial^2}{\partial x^2} + \frac{\partial^2}{\partial y^2} \right) P \\ &= \frac{1}{(1 - \xi(z))} \left(\frac{\partial^2 P}{\partial z^2} + \alpha^2 P \right). \end{aligned} \quad (3.30)$$

Note that we can recover Equation (3.7) by applying $-\left(\frac{\partial^2}{\partial x^2} + \frac{\partial^2}{\partial y^2}\right)$ to Equation (3.29). We will find the same solution class by solving Equation (3.29) as was sought by previous authors solving Equation (3.7) but without the inconvenience of having to solve the x - and y -components of Equation (3.4) afterwards. When $\xi(z) < 1$, Equation (3.29) is elliptic, when $\xi(z) = 1$ parabolic and when $\xi(z) > 1$ hyperbolic. The change in character of the equation as $\xi(z)$ varies through 1 is brought about by the fact that at $\xi(z) = 1$, $\nabla F \times \nabla \psi$ cancels with part of the current corresponding to P in Equation (3.15).

Noting that Equation (3.29) is linear and that its coefficients are independent of x and y we can Fourier transform P in the x - and y -directions,

$$P(x, y, z) = \iint \tilde{P}(k_x, k_y, z) e^{i(k_x x + k_y y)} dk_x dk_y \quad (3.31)$$

giving for Equation (3.29)

$$\frac{d^2 \tilde{P}}{dz^2} + [\alpha^2 - k^2 + k^2 \xi(z)] \tilde{P} = 0 \quad (3.32)$$

This is a Schrödinger-type equation again, and for several forms of $\xi(z)$ we can solve Equation (3.32) for \tilde{P} , upon which we can find P from Equation (3.31) at least in the form of a Fourier-Bessel integral (see Morse & Feshbach Vol. 1, p766), and in the simplest cases in a closed analytical form. We can then obtain expressions for the magnetic field components by substituting P back into Equation (3.15) recalling that $T = \alpha P$.

Having calculated a MHS equilibrium with a structure similar to a force-free field we are ready to derive a Green's function method for our MHS equilibrium class similar to the force-free method of Chiu & Hilton (1977). Before proceeding in this way we introduce in the next section the idea of a Green's function.

3.3 Introduction to Green's Functions

A central problem of field theory is that of fitting the solution of a given partial differential equation to suitable boundary conditions. Often the technique of expanding in eigenfunctions is used, a method which can be used whenever we can find a coordinate system, suitable to the boundaries, in which the equation will separate. However, the result is usually an infinite series which may converge slowly, making it difficult to achieve an insight into the general behaviour of the solution. For some problems it is more desirable to represent the solution with a closed function, even if it is an integral representation involving closed functions. The Green's function technique is such an approach.

The idea of the Green's function can be described in physical terms. To obtain the field caused by a distributed source we calculate the effect of each element of source and add them all. If $G(\mathbf{r}, \mathbf{r}')$ is the field at the observer's point \mathbf{r} caused by a unit source at the source point \mathbf{r}' then the field at \mathbf{r} caused by the source distribution $\rho(\mathbf{r}')$ is the integral of $G(\mathbf{r}, \mathbf{r}')\rho(\mathbf{r}')$ over the whole range of \mathbf{r}' occupied by the source. Here the function G is called the Green's function.

Boundary conditions can be satisfied in the same way. For Dirichlet boundary conditions (i.e. field values are given on the boundary) we calculate the field at \mathbf{r} for boundary values zero everywhere except at \mathbf{r}' (which is on the surface), where we impose delta-function behaviour, so that the integral of boundary values over any small surface area near \mathbf{r}' is unity. We call the field at the observer's point \mathbf{r} (not on the boundary) $G(\mathbf{r}, \mathbf{r}')$. Then the general solution for an arbitrary choice of boundary values $\psi(\mathbf{r}')$ is equal to the integral of $G(\mathbf{r}, \mathbf{r}')\psi(\mathbf{r}')$ over the boundary surface. This function G is also called the Green's function.

What makes these ideas useful is that these two functions G are essentially the same function. For certain linear partial differential equations we can obtain a function which, when integrated over a volume represents the field caused by a distributed source and which, when integrated over a surface, represents the field caused by specific boundary conditions on the surface. The fact that boundary conditions can be satisfied by surface integrals of source functions makes the use of source (Green's) functions very useful. The Green's function is a solution to an equation which is homogeneous everywhere except at one point. When the point is put on the boundary the Green's function may be used to satisfy inhomogeneous boundary conditions. When it is within the volume it may be used to satisfy the inhomogeneous equation.

In the context of our problem of solving the MHS equations in Cartesian coordinates in the Euclidean half space $z > 0$ with boundary $z = 0$ we aim to use a Green's function to solve inhomogeneous conditions on the boundary. Standing in our way is the task of calculating the Green's function. This is carried out in the next section.

3.4 Green's Function Method

Having decided upon a convenient method for calculating the equilibria we are in a position to consider fitting boundary data. We formulate the Green's function method for this class of MHS solutions by generalising the eigenfunction expansion method employed by Chiu & Hilton (1977). For convenience we rewrite Equation (3.31) as a Fourier-Bessel series in cylindrical coordinates

$$P(\rho, \phi, z) = \sum_{m=-\infty}^{\infty} e^{im\phi} \left(\int_0^{\infty} dk \left[A_m(k) Q_k^{(1)}(z) + B_m(k) Q_k^{(2)}(z) \right] J_m(k\rho) \right) \quad (3.33)$$

where ρ, ϕ are polar coordinates in the x - y plane, $k^2 = k_x^2 + k_y^2$, ϕ is the angle between x and y (the angle between k_x and k_y has been absorbed into $A_m(k)$ and $B_m(k)$), and $Q_k^{(i)}(z)$ are the solutions of

$$\frac{d^2 Q_k^{(i)}(z)}{dz^2} + [\alpha^2 - k^2 + k^2 \xi(z)] Q_k^{(i)}(z) = 0. \quad (3.34)$$

We assume without loss of generality that $Q_k^{(1)}(0) = Q_k^{(2)}(0) = 1$ since any other finite behaviour can be absorbed into $A_m(k)$ and $B_m(k)$. Substituting P into Equation (3.30) and applying Equation (3.34) gives

$$\begin{aligned} B_z(\rho, \phi, z) &= \frac{1}{1 - \xi(z)} \sum_{m=-\infty}^{\infty} e^{im\phi} \left(\int_0^{\infty} dk \left[A_m(k) \left(\frac{d^2}{dz^2} + \alpha^2 \right) Q_k^{(1)}(z) \right] J_m(k\rho) \right) \\ &+ \frac{1}{1 - \xi(z)} \sum_{m=-\infty}^{\infty} e^{im\phi} \left(\int_0^{\infty} dk \left[B_m(k) \left(\frac{d^2}{dz^2} + \alpha^2 \right) Q_k^{(2)}(z) \right] J_m(k\rho) \right) \\ &= \sum_{m=-\infty}^{\infty} e^{im\phi} \left(\int_0^{\infty} dk k^2 \left[A_m(k) Q_k^{(1)}(z) + B_m(k) Q_k^{(2)}(z) \right] J_m(k\rho) \right). \end{aligned} \quad (3.35)$$

We expect only one of $Q_k^{(1)}(z)$ and $Q_k^{(2)}(z)$ to decay with height. We assume this is $Q_k^{(1)}(z)$ and that $B_m(k) = 0$. To evaluate $A_m(k)$ with respect to the boundary data we use the identities

$$\int_0^{2\pi} e^{in\phi} e^{-im\phi} = 2\pi\delta_{mn} \quad (3.36)$$

$$\int_0^\infty dx x J_m(\lambda x) J_m(\lambda' x) = \frac{1}{\lambda'} \delta(\lambda - \lambda'), \quad (3.37)$$

multiply $B_z(\rho, \phi, 0)$ by $e^{-im\phi} J_m(k'\rho)$ then integrate it over $\int_0^\infty d\rho \rho \int_0^{2\pi} d\phi$

$$\begin{aligned} & \int_0^\infty d\rho \rho \int_0^{2\pi} d\phi e^{-im\phi} J_m(k'\rho) B_z(\rho, \phi, 0) \\ = & \int_0^\infty d\rho \rho \int_0^{2\pi} \sum_{n=-\infty}^{\infty} e^{in\phi} e^{-im\phi} \\ & \left(\int_0^\infty dk k^2 A_m(k) Q_k^{(1)}(z) J_m(k\rho) J_m(k'\rho) \right) \end{aligned} \quad (3.38)$$

$$\begin{aligned} = & 2\pi \int_0^\infty dk k^2 A_m(k) \int_0^\infty d\rho \rho J_n(k\rho) J_n(k'\rho) \\ = & 2\pi k' A_m(k') \end{aligned} \quad (3.39)$$

by Equation (3.36) and Equation (3.37) respectively. Thus

$$A_m(k) = \frac{1}{2\pi k} \int_0^\infty d\rho \rho \int_0^{2\pi} d\phi e^{-im\phi} J_m(k\rho) B_z(\rho, \phi, 0). \quad (3.40)$$

Substituting $A_m(k)$ back into Equation (3.33) then gives us P in a Green's function form

$$\begin{aligned} P(\rho, \phi, z) &= \sum_{m=-\infty}^{\infty} \int_0^\infty dk \frac{1}{2\pi k} \int_0^\infty d\rho' \rho' \int_0^{2\pi} d\phi' \\ & e^{im\phi} e^{-im\phi'} J_m(k\rho) J_m(k\rho') B_z(\rho', \phi', 0) Q_k^{(1)}(z) \\ &= \frac{1}{2\pi} \int_0^\infty d\rho' \rho' \int_0^{2\pi} d\phi' G_P(\rho, \phi, z, \rho', \phi', 0) B_z(\rho', \phi', 0) \end{aligned} \quad (3.41)$$

where

$$G_P(\rho, \phi, z, \rho', \phi', 0) = \int_0^\infty dk \frac{1}{k} J_0(kR) Q_k^{(1)}(z) \quad (3.42)$$

using the identity

$$\sum_{m=-\infty}^{\infty} e^{im(\phi-\phi')} J_m(k\rho) J_m(k\rho') = J_0(kR) \quad (3.43)$$

with $R^2 = (x - x')^2 + (y - y')^2$. The full k -spectrum from 0 to ∞ is necessary for the Green's function to have the correct behaviour at the boundary. Therefore it is not possible to reject unwanted wavenumbers for physical reasons as is done by e.g. Low (1991, 1992). As in the linear force-free case (Alissandrakis, 1981; Gary, 1989) the Green's function method presented here is equivalent to a Fourier integral transform method using the complete k -space. From Equations (3.15,3.27),

$$G_x = \frac{\partial^2 G_P}{\partial x \partial z} + \alpha \frac{\partial G_P}{\partial y} = \frac{\partial R}{\partial x} \frac{\partial \bar{\Gamma}}{\partial z} + \alpha \frac{\partial R}{\partial y} \bar{\Gamma} \quad (3.44)$$

$$G_y = \frac{\partial^2 G_P}{\partial y \partial z} - \alpha \frac{\partial G_P}{\partial x} = \frac{\partial R}{\partial y} \frac{\partial \bar{\Gamma}}{\partial z} - \alpha \frac{\partial R}{\partial x} \bar{\Gamma} \quad (3.45)$$

$$G_z = -\frac{\partial^2 G_P}{\partial x^2} - \frac{\partial^2 G_P}{\partial y^2} = -\frac{\partial \bar{\Gamma}}{\partial R} - \frac{\bar{\Gamma}}{R} \quad (3.46)$$

where $\bar{\Gamma} = \frac{\partial G_P}{\partial R}$ (c.f. Chiu & Hilton (14-16)), or

$$G_R = \frac{\partial \bar{\Gamma}}{\partial z} \quad (3.47)$$

$$G_\theta = -\alpha \bar{\Gamma} \quad (3.48)$$

$$G_z = -\frac{\partial \bar{\Gamma}}{\partial R} - \frac{\bar{\Gamma}}{R} \quad (3.49)$$

We remark that the structure of Equations (3.44-3.49) matches that anticipated by Equations (3.13,3.14). Using the identity

$$\frac{\partial}{\partial R} J_0(kR) = k J_0'(kR) = -k J_1(kR) \quad (3.50)$$

we can calculate

$$\bar{\Gamma} = \frac{\partial G_p}{\partial R} = - \int_0^\infty dk J_1(kR) Q_k^{(1)}(z). \quad (3.51)$$

Now we can calculate the Green's function components using Equations (3.47-3.49) and Bessel function identities:

$$G_R = - \int_0^\infty dk J_1(kR) \frac{d}{dz} Q_k^{(1)}(z) \quad (3.52)$$

$$G_\theta = \alpha \int_0^\infty dk J_1(kR) Q_k^{(1)}(z) \quad (3.53)$$

$$G_z = \int_0^\infty dk k J_0(kR) Q_k^{(1)}(z) \quad (3.54)$$

where Equation (3.54) is calculated either from Equation (3.51) and the identity

$$-\frac{\partial}{\partial R} J_1(kR) - \frac{J_1(kR)}{R} = -k J_0(kR) \quad (3.55)$$

or from Equation (3.42) and the first equality of Equation (3.30). The Cartesian Green's function components can then be calculated from

$$G_x = \frac{x-x'}{R} G_R - \frac{y-y'}{R} G_\theta \quad (3.56)$$

$$G_y = \frac{x-x'}{R} G_\theta + \frac{y-y'}{R} G_R. \quad (3.57)$$

This is the structure of the Green's function solutions found by Chiu & Hilton (1977) for the force-free case, where the magnetic field is known in terms of a scalar function $\bar{\Gamma}$. We have generalised this structure to include our adopted class of MHS equilibria. Finally we can write the magnetic field in Green's function form

$$\mathbf{B}(x, y, z) = \int_{z'=0} \mathbf{G}(x-x', y-y', z) B_z(x', y', 0) dx' dy' \quad (3.58)$$

where $\mathbf{G} = (G_x, G_y, G_z)$. This concludes the derivation of the non-force-free Green's function method for our special MHS solution class.

Except for the force-free and $\xi = \text{constant}$ cases we only know Green's function as a Fourier-Bessel integral. Chiu & Hilton (1977) could calculate their force-free Green's function in closed form by this method only because their Fourier-Bessel integral was to be found in the Hankel transforms literature. If $\xi(z)$ takes any other form (except $\xi(z) = \text{constant}$) the resulting Fourier-Bessel integral cannot to the knowledge of the author be treated analytically. In order to keep our discussion analytically explicit, we will concentrate on the force-free and $\xi = \text{constant}$ cases which will give us a closed analytical form for the Green's function, before describing a more complicated and practically applicable case as far as is analytically possible.

3.5 Special Cases

3.5.1 Force-Free Case

The force-free case has already been calculated by Chiu & Hilton (1977) using the P -representation method of the last section. However, this case can also be treated using a more standard Green's function method as described in Morse & Feshbach (1953) Vol. 2. A derivation of the force-free Green's function using this method is given in Appendix B. The results are found to agree with those of Chiu & Hilton (1977) and we quote them here. The expression for $\bar{\Gamma}$ is

$$\bar{\Gamma} = \frac{z}{Rr} \cos(\alpha r) - \frac{1}{R} \cos(\alpha z). \quad (3.59)$$

where r is defined by $r^2 = R^2 + z^2$, giving for the Green's function components

$$G_R = \frac{R}{r^3} \cos(\alpha r) - \frac{z^2}{Rr^2} \alpha \sin(\alpha r) + \frac{\alpha}{R} \sin(\alpha z) \quad (3.60)$$

$$G_\theta = -\frac{\alpha z}{Rr} \cos(\alpha r) + \frac{\alpha}{R} \cos(\alpha z) \quad (3.61)$$

$$G_z = \frac{\alpha z}{r^2} \sin(\alpha r) + \frac{z}{r^3} \cos(\alpha r). \quad (3.62)$$

Note that this is not a unique solution since the general solution includes also a multiple of a complementary Green's function $\tilde{\mathbf{G}}$ whose constant of multiplication is not

determined by the boundary conditions (see Chiu & Hilton, 1977; Gary, 1989; Lothian & Browning, 1995). We follow these authors in ignoring contributions from $\tilde{\mathbf{G}}$ (see also Appendix B). Recently, there have been several suggestions for how $\tilde{\mathbf{G}}$ could be determined by minimising the deviation of the force-free field on the boundary from the measured field (Amari et al., 1997; Wheatland, 1999). Although we do not consider these possibilities here we remark that these approaches will in principle also work for the non-force-free fields discussed below. As a full assessment of this possibility is beyond the scope of this thesis we leave the discussion for future work and include only \mathbf{G} in the following.

3.5.2 Case $\xi(z) = \text{constant}$

If $\xi(z) = \xi_0$ a constant then Equation (3.29) becomes equivalent to the force-free case if $\xi_0 < 1$. To see this, let

$$\alpha_{ff} = \frac{\alpha}{\sqrt{1 - \xi_0}}, \quad z_{ff} = \sqrt{1 - \xi_0}z \quad (3.63)$$

so that

$$(1 - \xi_0) \left[\frac{\partial^2 P}{\partial x^2} + \frac{\partial^2 P}{\partial y^2} + \frac{\partial^2 P}{\partial z_{ff}^2} + \alpha_{ff}^2 P \right] = 0 \quad (3.64)$$

This correspondence breaks down for $\xi_0 \geq 1$ and such cases must be treated in another way. We omit them here, however, since we are interested only in cases with relatively small cross-field currents. This approach is similar to the stretching procedure discussed by Lites et al. (1995) and to the transformation in spherical coordinates employed by Gary & Alexander (1999) to introduce non-force-free effects to their model. From substituting Equation (3.63) into Equation (3.59) the expression for $\bar{\Gamma}$ is

$$\bar{\Gamma} = \frac{\sqrt{1 - \xi_0}z}{Rr} \cos\left(\frac{\alpha r}{\sqrt{1 - \xi_0}}\right) - \frac{1}{R} \cos(\alpha z) \quad (3.65)$$

with $r^2 = x^2 + y^2 + (1 - \xi_0)z^2$, giving for the Green's function components using Equations (3.47-3.49)

$$G_R = \sqrt{1-\xi_0} \frac{R}{r^3} \cos\left(\frac{\alpha r}{\sqrt{1-\xi_0}}\right) + (1-\xi_0) \frac{z^2}{Rr^2} \alpha \sin\left(\frac{\alpha r}{\sqrt{1-\xi_0}}\right) - \frac{\alpha}{R} \sin(\alpha z) \quad (3.66)$$

$$G_\theta = -\alpha \frac{\sqrt{1-\xi_0} z}{Rr} \cos\left(\frac{\alpha r}{\sqrt{1-\xi_0}}\right) + \alpha \frac{1}{R} \cos(\alpha z) \quad (3.67)$$

$$G_z = \frac{\alpha z}{r^2} \sin\left(\frac{\alpha r}{\sqrt{1-\xi_0}}\right) + \frac{\sqrt{1-\xi_0} z}{r^3} \cos\left(\frac{\alpha r}{\sqrt{1-\xi_0}}\right). \quad (3.68)$$

Our strategy for finding analytically tractable worked examples in the next chapter will be to transform force-free solutions to constant- ξ solutions and generate self-consistent models of fields with three-dimensional pressure and density profiles (see Chapter 4).

3.5.3 Case $\xi(z) = ae^{-\kappa z}$

With this form of $\xi(z)$ the magnetic field is approximately force-free above a boundary layer of height $\frac{1}{\kappa}$ with a static interaction between the field and the plasma with magnitude increasing towards the photosphere (see Low 1991, 1992).

Referring to Equation (3.32) we solve Schrödinger's equation

$$\frac{\partial^2 Q_k^{(i)}}{dz^2} + [\alpha^2 - k^2 + k^2 a e^{-\kappa z}] Q_k^{(i)} = 0. \quad (3.69)$$

Note from Equation (3.69) that its general solution in the limit of large z becomes the force-free general solution, while in the limit of small z its general solution is asymptotically the constant- ξ general solution. The general solution of Equation (3.69) is found as follows (see Morse & Feshbach 1953 Vol. 2, p1670):

Let $\eta = be^{-cz}$. Then Equation (3.69) becomes

$$\frac{d^2 Q_k^{(i)}}{d\eta^2} + \frac{1}{\eta} \frac{dQ_k^{(i)}}{d\eta} + \left[\frac{\alpha^2 - k^2}{c^2 \eta^2} + \frac{ak^2}{b^{\frac{\kappa}{c}} c^2} \eta^{\frac{\kappa}{c} - 2} \right] Q_k^{(i)} = 0. \quad (3.70)$$

This is a Bessel equation if

$$\eta = \sqrt{\frac{4k^2 a}{\kappa^2}} e^{-\frac{1}{2}\kappa z}, \quad s^2 = \frac{4(k^2 - \alpha^2)}{\kappa^2}. \quad (3.71)$$

Then the general solution is

$$Q_k^{(i)} = \tilde{M}J_s(\eta) + \tilde{N}J_{-s}(\eta) \quad (3.72)$$

where \tilde{M} and \tilde{N} are functions of k_x and k_y . Assuming that \mathbf{B} vanishes as $z \rightarrow \infty$ implies $\tilde{N} = 0$. Now from Equation (3.42) we can write

$$G_P = \int_0^\infty \tilde{M}J_s(\eta)J_0(kR)\frac{1}{k}dk \quad (3.73)$$

where we now choose \tilde{M} to depend only on $k = \sqrt{k_x^2 + k_y^2}$. From Equation (3.51),

$$\bar{\Gamma} = \frac{\partial G_P}{\partial R} = - \int_0^\infty dk J_1(kR)\tilde{M}J_s(\eta). \quad (3.74)$$

Now we can calculate the Green's function components using Equations (3.52-3.54):

$$G_R = \int_0^\infty dk J_1(kR)\tilde{M}(-\sqrt{4k^2a}e^{-\kappa z}J_{s+1}(\eta) + \sqrt{4(k^2 - \alpha^2)}J_s(\eta)) \quad (3.75)$$

$$G_\theta = \alpha \int_0^\infty dk J_1(kR)\tilde{M}J_s(\eta) \quad (3.76)$$

$$G_z = \int_0^\infty dk k J_0(kR)\tilde{M}J_s(\eta) \quad (3.77)$$

If we choose \tilde{M} so that

$$\tilde{M}J_s\left(\sqrt{\frac{4k^2a}{\kappa^2}}\right) = 1 \quad (3.78)$$

then we have as $z \rightarrow 0$

$$G_z \rightarrow \int_0^\infty J_0(kR)kdk = \frac{1}{R}\delta(R), \quad (3.79)$$

giving G_z the desired unit two-dimensional delta function behaviour on the boundary.

Taking the limit as $z \rightarrow \infty$

$$\begin{aligned}
\tilde{M}J_s(\eta) &\approx \frac{\left(\frac{1}{2}\sqrt{\frac{4k^2a}{\kappa^2}}e^{-\frac{1}{2}\kappa z}\right)^s}{\Gamma(s+1)} \bigg/ \frac{\left(\frac{1}{2}\sqrt{\frac{4k^2a}{\kappa^2}}\right)^s}{\Gamma(s+1)} \\
&= e^{-\sqrt{k^2-\alpha^2}z}
\end{aligned} \tag{3.80}$$

and we have recovered the eigenfunction for Equation (3.34) with $\xi(z) = 0$. Our solution is asymptotically force-free at large heights.

Note that we can treat the case $\xi(z) = ae^{-\kappa z} + c$ by transforming to the case $c = 0$ as in Subsection 3.5.2. We anticipate that a description a coronal magnetic field by this class of Green's function solutions will be calculated using a solution with this form of ξ as it appropriately models the concentration of the interaction of the magnetic field with the plasma near the photosphere while it is approximately force-free in the corona. To keep the mathematics simple we use in our illustrative example solutions of Chapter 4 a constant ξ . We concede that this reduced versatility compromises the worked examples of Chapter 4. However this compromise is necessary for the time being. The constant- ξ Green's function is a relatively simple closed function Equations (3.66-3.68) while the exponential- ξ Green's function Equations (3.75-3.77) includes integrals of Bessel functions whose calculation seems a non-trivial task. However, close to $z = 0$ the constant- ξ and exponential- ξ solutions are almost equal and so the worked examples of Section 4 should give a fair indication of how an exponential- ξ method will perform, at least close to the photosphere. We leave the implementation of an exponential- ξ Green's function method for future work.

3.6 Discussion

We have derived the Green's function method for a particular class of MHS equilibria for which the current density is a combination of a linear force-free part and a part with non-force-free components. The method was developed by extending an existing linear force-free field Green's function method and by exploiting a recently-discovered relationship between linear force-free fields and the class of MHS equilibria. Existing Green's function methods are force-free and allow only an indirect comparison between

extrapolated coronal fieldlines and observed parameter profiles. This MHS Green's function method therefore allows the first opportunity for a direct comparison between a coronal magnetic field model and observation. An artificial intensity map may be constructed from the model for direct comparison with an observed intensity map. We have also presented in Appendix B a derivation of the linear force-free Green's function based on textbook theory for the Helmholtz equation. This places the nonstandard eigenfunction expansion method used elsewhere in agreement with standard textbook theory.

We have prepared the solutions anticipating fitting the vertical magnetic field component on the photosphere. In fact, Semel (1988) has presented a method of fitting line-of-sight data to a linear force-free Green's function solution but his idea is not easily applied to our scheme because of the strictly vertical influence of gravity. It remains to be seen how much of a practical limitation this will be when we try to fit our solutions to observational data.

We have omitted the term of the Green's function which is zero on the boundary. It would be most natural to fix it by imposing the value of a component of \mathbf{B} other than B_z on the boundary but we cannot see an easy way of fixing the coefficient of this term using a horizontal field component were one available from observation. Although vector magnetogram data sets are becoming more common, and will become even more so as new improved instruments are used, most data sets available to us at present have only a line-of-sight component and even in the case of vector magnetogram data sets there is much uncertainty in the horizontal components. Nevertheless a natural forward-looking step would be to use every piece of information available to us in improving the solutions, e.g. horizontal magnetic field components where available. For the force-free case Chiu & Hilton (1977) suggest imposing the angle

$$\tan \delta(x, y, 0) = \frac{B_y(x, y, 0)}{B_x(x, y, 0)} \quad (3.81)$$

fixing all three field components. Alternatively Amari et al. (1997) and Wheatland (1999) suggest minimising the deviation of the calculated field from the measured field components on the photosphere by varying the coefficient of the term of the Green's

function which is zero on the boundary or α and we can imagine attempting something similar with our non-force-free case where we have the additional freedom of a non-force-free function ξ to vary as well. It remains to be seen if implementing such a scheme is feasible.

An impression of how the constant- ξ Green's function method performs when fitted to observational data is given in Chapter 4 where line-of-sight magnetograms of a solar coronal bright point, a region where a filament forms and a sigmoid-like structure are all used as boundary conditions. For practical reasons implementation of an exponential- ξ Green's function method is left for future work.

Chapter 4

Magnetohydrostatic Green's Function Method: Applications

4.1 Introduction

In this chapter we continue the work of Chapter 3 in developing the magnetohydrostatic Green's function method of that chapter to prepare it for application to observational data in the form of line-of-sight magnetograms. The worked example of Section 4.2 appeared in the paper Petrie & Neukirch (2000).

Given photospheric boundary data for the line-of-sight magnetic field, we aim to model the corona above it. The usual method is to assume that the magnetic field is strong and that the cross-field current is relatively small but nevertheless large enough to structure the plasma, and then to extrapolate the field into the corona using a force-free method. It may be possible in the future to model this situation more fully by deriving an expansion method where the description is force-free to first order and the plasma structuring is modelled at a higher order. For the moment, however, we include cross-field currents more directly by using the force-balance Equation (3.1) of MHS to calculate a self-consistent interaction of the plasma and magnetic field. We then compare the resulting calculated plasma structure directly with observed emission patterns.

For given $\xi(z)$ a Green's function solution for \mathbf{B} can be derived using B_z at $z = 0$ as boundary condition

$$\mathbf{B}(x, y, z) = \int_{z'=0} dx' dy' \mathbf{G}(x - x', y - y', z) B_z(x', y', 0) \quad (4.1)$$

For Ampère's Law to be linear and easy integration of the force-balance equation for p and ρ , assume (for $\alpha = \text{constant}$)

$$\mathbf{j} = \alpha \mathbf{B} + \nabla \times (\xi(z) B_z \hat{\mathbf{z}}) \quad (4.2)$$

(see Chapter 3). In this case the Green's function can usually not be given in closed form (but always as a one-dimensional integral). For the special case of $\xi(z) = \xi_0 = \text{constant}$ a closed form of the Green's function can be found by rescaling α and z in the force-free Green's function (see Subsection 3.5.2). This is the simplest non-force-free solution available to us and for computational simplicity we will apply this solution throughout the present chapter. We leave application of a more complicated Green's function for future work.

This chapter is organised as follows. We give in Section 4.2 a simple example of a solution of this type and investigate some of its properties. Section 4.3 explains how we adapt the simple example of Section 4.2 to the task of fitting such a solution to observational data. In Section 4.4 we briefly mention the telescopes and instruments used to obtain the featured observational data sets before their reaching the author. Sections 4.5, 4.6 and 4.7 give the results of applying the Green's function method to three sets of observational data: of a solar coronal bright point, of the formation of a filament and of a sigmoid-like structure respectively. Section 4.8 describes an attempt at using the method to model an intense flux tube. We conclude the chapter with a discussion in Section 4.9.

4.2 Illustrative Example: $\xi(z) = \text{constant}$

Having derived the Green's function for the upper half space in Chapter 3 and before applying the method to observational data in Sections 4.5, 4.6 and 4.7 we illustrate the method with a simple example. To obtain an analytical expression for the magnetic field we generate boundary flux at $z = 0$ by putting point magnetic sources a small distance under the photosphere:

$$B_z(x, y, a) = \sum_i w_i \delta(x - x_i, y - y_i, z - a). \quad (4.3)$$

for some small negative a . We must have $z = a$ below the boundary in order to ensure that the magnetic field and also the plasma pressure and density are finite in the volume of interest, but otherwise a is a free parameter. We restrict ourselves to point magnetic sources at points (x_i, y_i, a) in this example so that we can easily obtain closed analytical expressions for the magnetic field components. We implicitly make the assumption that the current density below the photosphere has the same form as that above the photosphere so that the magnetic sources generate just the right boundary field at $z = 0$. We emphasise that in principle we could calculate the magnetic field and plasma quantities for any given distribution of B_z on $z = 0$ and that we use this particular configuration in our example for convenience.

From Equation (3.58)

$$\mathbf{B}(x, y, z) = \sum_i w_i \mathbf{G}(x - x_i, y - y_i, z - a) \quad (4.4)$$

Denoting by $p_B(z)$ the hydrostatic background pressure, the plasma pressure and density can be found from

$$p(x, y, z) = p_B(z) - \frac{1}{2\mu_0} \xi_0 B_z(x, y, z)^2 \quad (4.5)$$

$$\rho(x, y, z) = -\frac{1}{g} \frac{dp_B}{dz} + \frac{1}{\mu_0 g} \mathbf{B} \cdot (\nabla(\xi_0 B_z)) \quad (4.6)$$

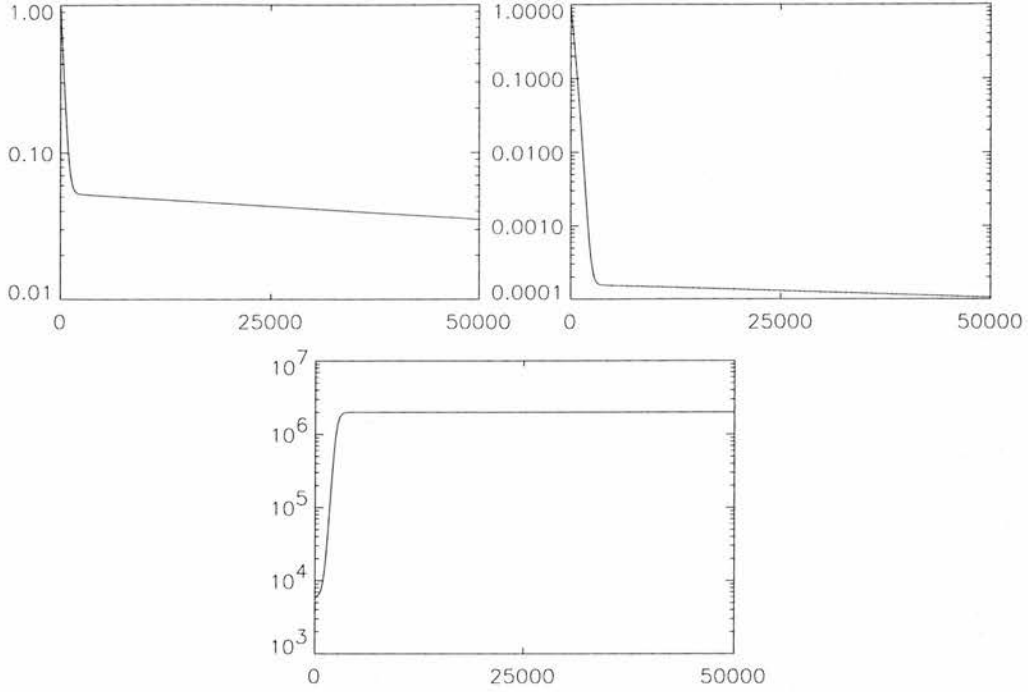


Figure 4.1: Plots of the background hydrostatic equilibrium plasma parameters (vertical axes) against height (horizontal axes). Top left: background pressure. Top right: background density. Bottom: background temperature. The background parameter profiles are independent of x and y so that any three-dimensionality in the final profiles is caused by non-force-free interaction between the plasma and the magnetic field. Heights are in kilometres, temperatures are in Kelvin and the pressure and density have been normalised using their photospheric values.

both of which have to be kept positive and non-singular in $z \geq 0$. This is clearly not possible for $a = 0$ because \mathbf{G} is singular at the position of the source.

Assuming the plasma to be an ideal gas it is possible to define the temperature by

$$T = \frac{\mu p}{k_B \rho} \quad (4.7)$$

where μ = mean molecular weight and k_B = Boltzmann constant.

The particular example we consider has two flux sources (monopoles) underneath the photospheric boundary. The magnetic field therefore has the shape of a three-

dimensional magnetic flux tube with strong field inside the tube and a drop-off of the field strength with increasing distance from the tube. The example is completed by a model for the background atmosphere which is to mimic the average solar atmosphere from photosphere through chromosphere and transition region up to the corona. To achieve this we have chosen a background temperature profile $T_B(z)$ given by

$$T_B(z) = T_0 + \Delta T \tanh\left(\frac{z - z_0}{\Delta z}\right) \quad (4.8)$$

where T_0 is the temperature at $z = 0$, ΔT is the difference between the temperature at $z = 0$ and the asymptotic temperature for $z \rightarrow \infty$, and z_0 and Δz are the position and width of the model transition region respectively. The hydrostatic equilibrium equation

$$\frac{dp_B}{dz} = -\rho_B g = -\frac{\mu p_B}{k_B T_B} g \quad (4.9)$$

is used to calculate the background pressure. Finally the background density $\rho_B(z)$ is calculated from Equation (4.7). Figure 4.1 shows plots of the background pressure $p_B(z)$, background density $\rho_B(z)$ and background temperature $T_B(z)$ against height used in this example.

Figure 4.2 shows a set of 20 magnetic field lines having their footpoints on a circle centred above the positive polarity source. In the example shown the length scale is $L = 5000\text{km}$. The square domain of the plot extends from $-5L$ to $5L$ in both x and y , and shows the vertical magnetic field strength and polarity in grey scale from maximum positive (white) to maximum negative (black). The sources are located at $z_+ = z_- = -1.0$ beneath the photosphere at the positions $(x_+, y_+) = (-2.5L, -2.5L)$ for the positive flux source and $(x_-, y_-) = (2.5L, 2.5L)$ for the negative source. In the example shown we use the values $\alpha = 0.5$ and $\xi_0 = -0.1$. The field-aligned currents cause a visible twisting of the field lines. This is in contrast to the potential field case $\alpha = \xi_0 = 0$ where the field lines are not twisted (see Figure 4.3, left panel). The effect of the cross-field currents on the magnetic field is relatively small if one compares this example with the corresponding force-free case ($\xi_0 = 0$, see Figure 4.3, right panel), and different values of $\xi_0 \neq 0$ do not alter the fieldlines significantly. The spatial variation of the plasma parameters, however, is noticeably changed by the presence of the cross-field

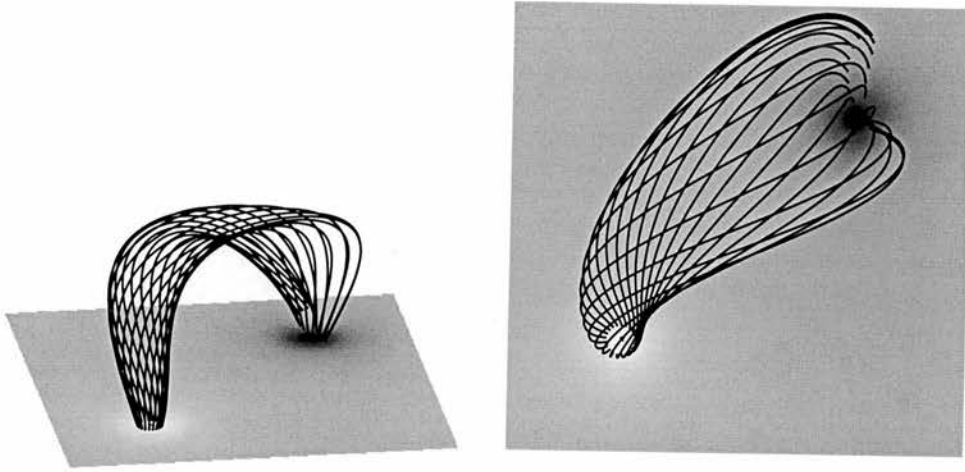


Figure 4.2: Field line plot of example with $\alpha = 0.5$ and $\xi_0 = -0.1$ (left) with view from above (right). Shown are 20 field lines with one foot point on a circle of radius 0.3125 centred above the monopole of positive polarity. The field is generated by two submerged ($z = a = -1.0$) sources of equal but opposite strength.

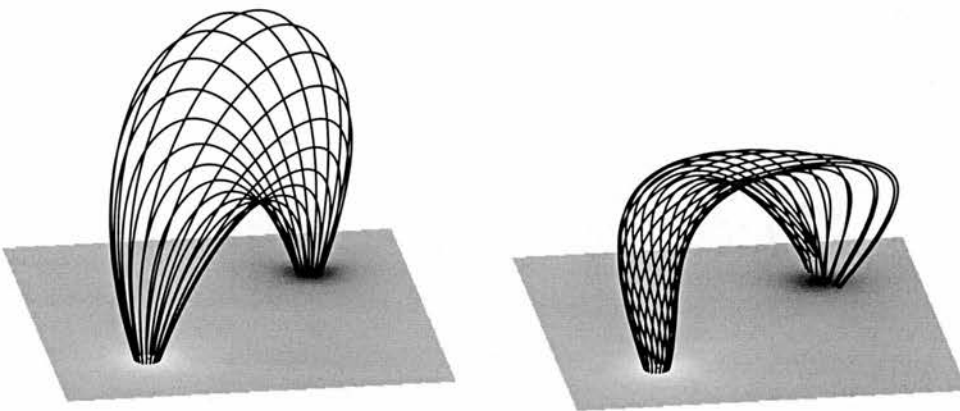


Figure 4.3: Field line plot of examples with $\alpha = 0.0$ and $\xi_0 = 0.0$ (left) and with $\alpha = 0.5$ and $\xi_0 = 0.0$ (right). See caption to Figure 4.2 for more details.

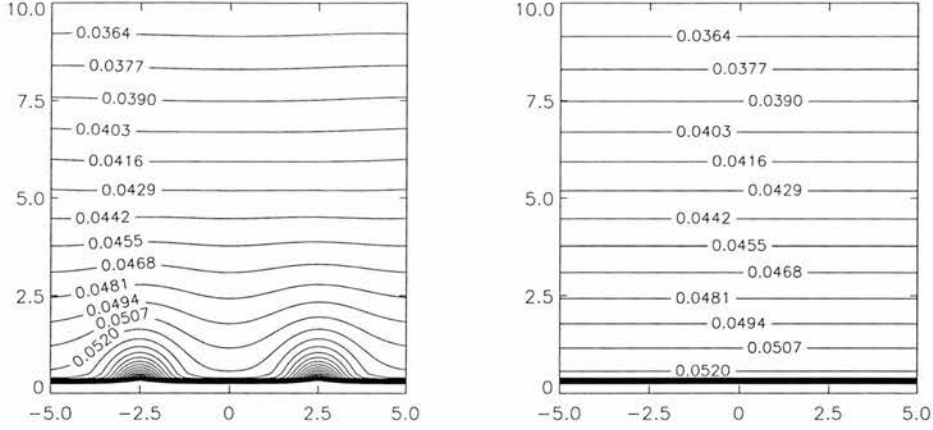


Figure 4.4: Contour plots of the pressure variation in the planes $x = y$ (left) and $x = -y$ (right). In the plane $x = -y$ the pressure does not vary significantly from the background pressure (see Figure 4.5). In the $x = y$ plane pressure deviation from background is particularly significant near the magnetic flux sources ($x = y \approx \pm 2.5$, z small) and the contours are affected to the top of the plot. Any pressure deviation from the background is an increase in this example.

currents. The three-dimensional structure of the pressure function can be seen in detail by comparing Figures 4.4 with Figure 4.5. Figure 4.6 shows a pressure isosurface which in the force-free case would be a plane parallel to the photosphere. The presence of the current especially in the regions of strong field distorts the isosurface. Two humps at the intersection of the flux tube with the surface indicate that the pressure increases inside the tube region. Referring to Equation (4.5) this is to be expected because ξ_0 is negative and therefore p increases above the background level as B_z increases. The density and temperature profiles can also be seen to be significantly different from their one-dimensional backgrounds, complicated three-dimensional structures influenced by the magnetic field configuration being clearly visible in Figures 4.7-4.11. Although, referring to Figures 4.9 and 4.11, it appears that the density has increased over the background model in the vicinity and that the temperature has decreased, it is evident in Figures 4.7 and 4.10 that regions of decreased density and regions of increased temperature also exist.

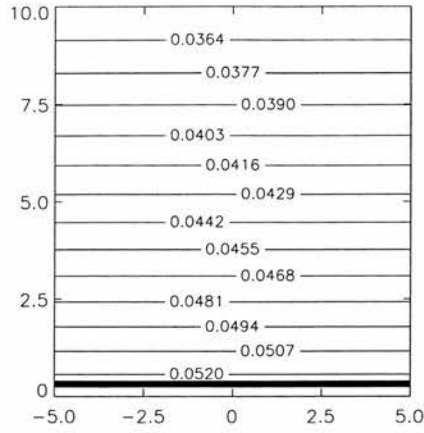


Figure 4.5: Contour plot of the background pressure variation. The background pressure varies only with z hence all contours are horizontal. This is how Figure 4.4 would appear in the force-free ($\xi_0 = 0$) case.

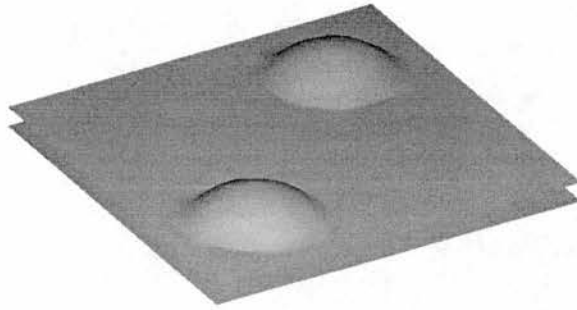


Figure 4.6: Pressure isosurface $p = 0.054$. The magnetic field influences the plasma significantly where the pressure isosurface deviates from the horizontal background profile. As indicated in Figure 4.4 pressure deviation from background is concentrated to the regions immediately above the two flux sources.

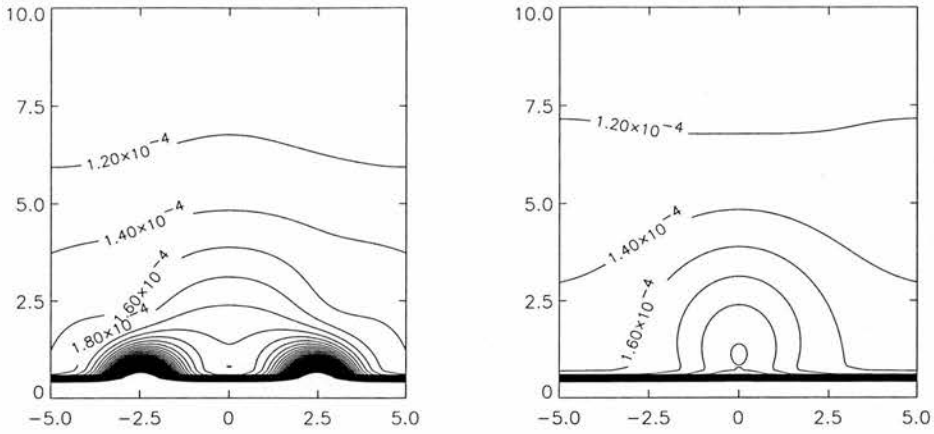


Figure 4.7: Contour plots of the density variation in the planes $x = y$ (left) and $x = -y$ (right). Comparison with Figure 4.8 shows that there is density variation from background in both planes. Density increases over background are visible in regions close to the magnetic flux sources ($x = y \approx \pm 2.5$, z small) and in a loop-like structure connecting these two regions (see Figure 4.9, bottom picture) while density depletions are to be seen around the origin and in the $x = y$ plane near the sides of the box.

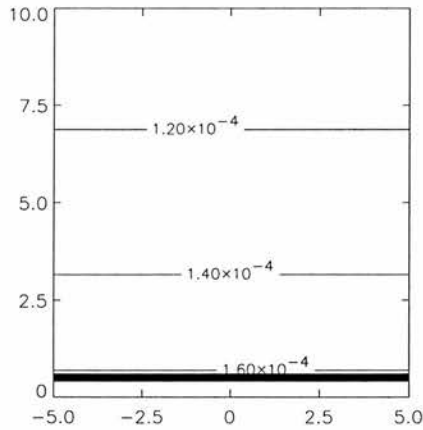


Figure 4.8: Contour plot of the background density variation. The background density varies only with z hence all contours are horizontal. This is how Figure 4.7 would appear in the force-free ($\xi_0 = 0$) case.

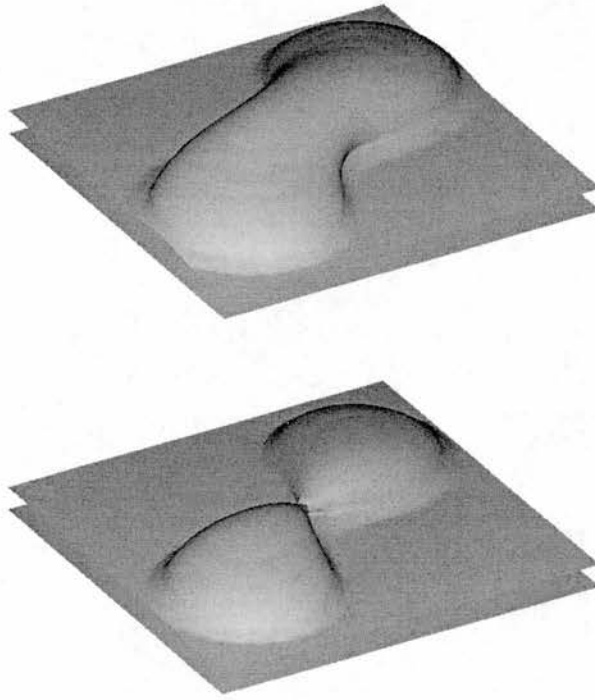


Figure 4.9: Density isosurfaces $\rho = 0.0002$ (top) and $\rho = 0.000221$ (bottom). The $\rho = 0.0002$ indicates a slight density concentration above the density sources. The $\rho = 0.00020$ isosurface hints at a loop-like structure of increased density against background which bridges the depleted region (see Figure 4.7).

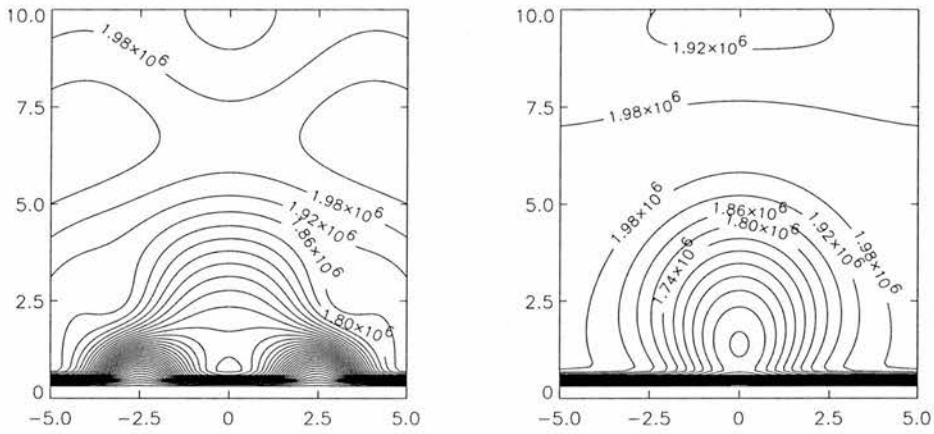


Figure 4.10: Contour plots of the temperature variation in the planes $x = y$ (left) and $x = -y$ (right). Comparison with the background temperature profile in Figure 4.1 shows that there is variation from background in both planes. There are temperature depletions from the background near the magnetic flux sources ($x = y \approx \pm 2.5$, z small) and in a loop-like structure connecting these two regions suggesting along with the density plots a structure of plasma slightly cooler and denser than the surroundings connecting the two regions above the magnetic flux sources (see Figure 4.11). The background temperature is constant except for small values of z (see Figure 4.1), where it varies only with z hence all contours would be horizontal.

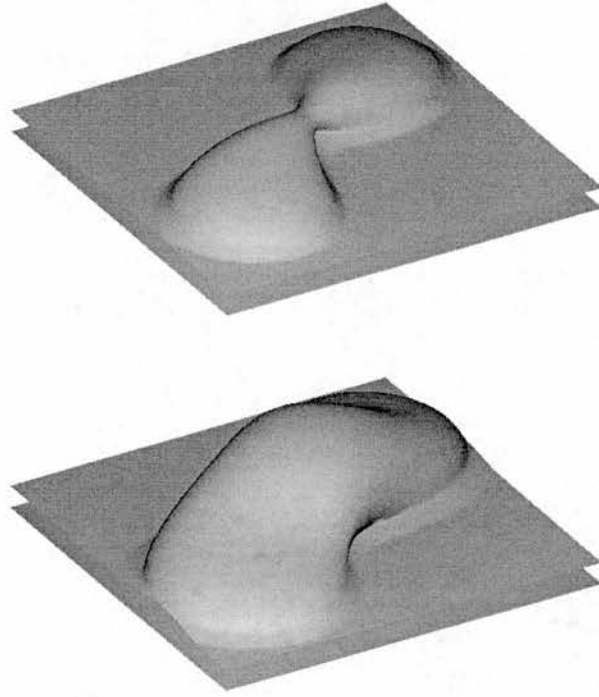


Figure 4.11: Temperature isosurfaces $T = 1.38 \times 10^6\text{K}$ (top) and $T = 1.60 \times 10^6\text{K}$ bottom. The pictures show a relatively cool loop-like structure connecting regions of low temperature, which are concentrated above the magnetic flux sources.

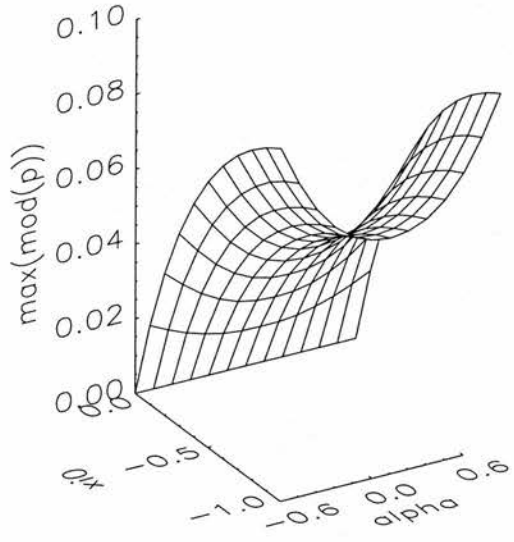
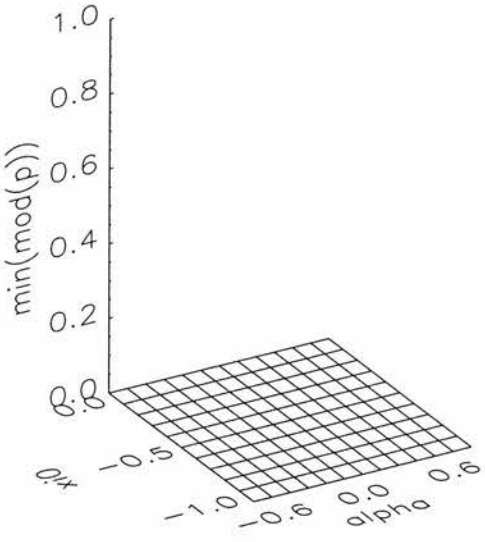
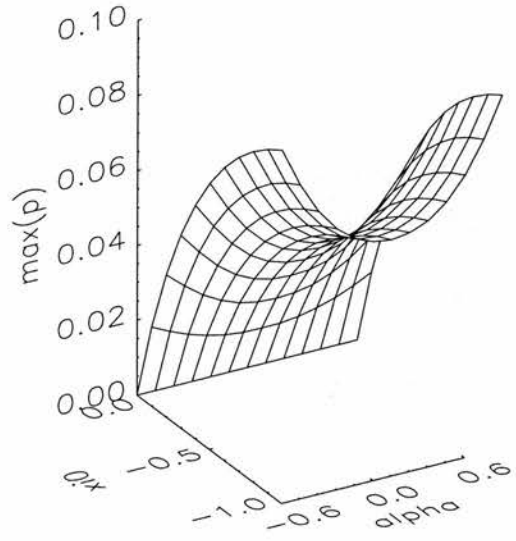
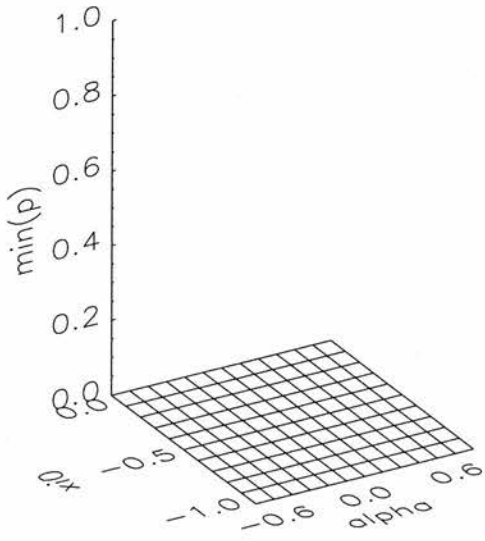


Figure 4.12: Top left: $\min(p - p_{back})$ for a range of values of α and ξ_0 . Top right: $\max(p - p_{back})$. Bottom left: $\min|p - p_{back}|$. Bottom right: $\max|p - p_{back}|$.

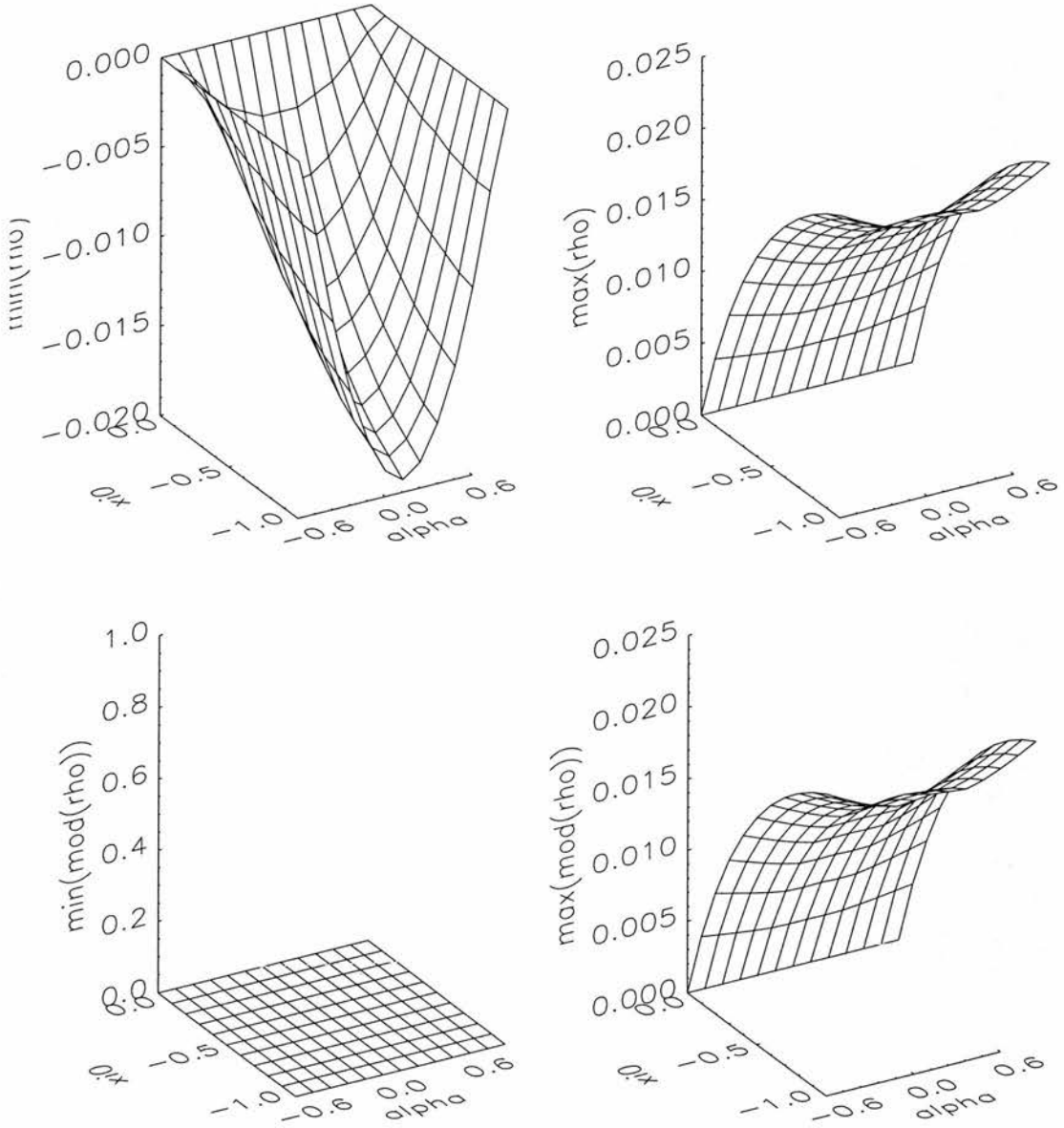


Figure 4.13: Top left: $\min(\rho - \rho_{back})$ for a range of values of α and ξ_0 . Top right: $\max(\rho - \rho_{back})$. Bottom left: $\min|\rho - \rho_{back}|$. Bottom right: $\max|\rho - \rho_{back}|$.

Figures 4.12 and 4.13 indicate how the deviation of the pressure and density parameters from the background is related to the constants α and ξ_0 . Minimum, maximum, minimum modulus and maximum modulus over the volume $(x, y, z) \in [-5.0, 5.0] \times [-5.0, 5.0] \times [0.0, 10.0]$ of $p - p_{back}$ and $\rho - \rho_{back}$ were taken in turn for discrete combinations of values of α and ξ_0 . The resulting minima and maxima for the different parameter combinations are graphed against their parameter values in Figures 4.12 and 4.13.

Many of the constant- ξ examples have some negative density in the domain. For $\xi_0 = 0$ the deviation from background hydrostatic equilibrium of all quantities is zero because this is the force-free case. For α from about -0.6 to 0.6 with ξ_0 negative the pressure and density stay non-negative as for all force-free examples but for other parameter values there are problems. The pressure graphs, Figure 4.12, are all symmetric about $\alpha = 0$ because of the B_z^2 -dependence of Equation (4.5). For all values of α and ξ_0 tested the pressure coincides with the background pressure at some point (wherever $B_z = 0$, see Equation (4.5)). In the case $\xi_0 > 0$ the pressure is less than or equal to the background pressure. For all parameter value combinations tested there is always some point where the pressure coincides with the background pressure and there is always a pressure drop against background somewhere. Meanwhile in the case $\xi_0 < 0$ the pressure is greater than or equal to the background pressure. For all parameter value combinations tested there is always some point where the pressure coincides with the background pressure (wherever $B_z = 0$) and there is always a pressure increase against background somewhere.

Referring now to Figure 4.13, for all values of α and ξ_0 tested the density coincides with the background density at some point. For $\xi_0 \neq 0$ a point where the density is less than background always exists, as does a point where the density is greater than background, indicating that mass displacement from the background density profile occurs in the volume of interest for this non-force-free case.

4.3 Applying the Method to Observational Data

In Section 4.2 we give an illustrative worked example solution where the boundary flux is generated by only two point sources below the photosphere $z = 0$ allowing us to represent the solutions for the magnetic field and the plasma pressure, density and temperature analytically. Because magnetograms are in the form of discrete two-dimensional arrays of numbers we can adapt our method by using a discrete grid of point sources below the photosphere, choosing their strength by fixing the solution at the boundary.

Recall that for chosen constants α and ξ_0 the Green's function solution for the magnetic field is given by Equation (4.1) where the components of \mathbf{G} are given in the simple closed form Equations (3.66-3.68). We further simplify the expression for the magnetic field by composing \mathbf{B} of a finite sum of source solutions (one source submerged below each boundary pixel to avoid singularities) and distributing weight among source solutions as is necessary for the solution at the boundary to match the magnetogram. This discrete form of the integral represents the boundary conditions as fully as is possible since the magnetogram is also discrete. If we number the $m \times n$ magnetogram pixels sequentially $(x_j, y_j, z_j = 0)$ where $j = 1, \dots, m \times n$ and label our source grid points in an identical manner $(x_i, y_i, z_i = a)$ where $i = 1, \dots, m \times n$ then the magnetic field is given by the lengthy but finite sum

$$\mathbf{B}(x, y, z) = \sum_i w_i \mathbf{G}(x - x_i, y - y_i, z - a) \quad (4.10)$$

and the weighting given to each source solution is calculated by solving the linear equation

$$\sum_i w_i G_z(x_j - x_i, y_j - y_i, 0 - a) = M_j \quad (4.11)$$

where $M_j, j = 1 \dots m \times n$ are the magnetogram entries also labelled sequentially. This is a large matrix equation which can be solved using a LU decomposition solver for magnetograms of up to about 3500 pixels (giving a 3500^2 matrix to invert) on the desktop workstations available. In each example of this chapter magnetogram observations

of our region of interest may be available at a higher resolution than this, and we rebin the magnetogram before applying the method. Plasma structures arising from applying the method are restricted to macroscopic length scales and so this loss of resolution does not significantly alter a result, as was verified by repeating a test case at different resolutions.

In this chapter we attempt to model a solar coronal bright point, a region in which a filament forms and a sigmoid-like structure by extrapolating from observed magnetic field data (we also attempt a simple model of an intense flux tube by supplying synthetic boundary data). Each of these features is briefly described in Section 1.2 of the introduction to this thesis. In each case the solar atmosphere is reconstructed with the method using line-of-sight magnetogram data and is then compared to available plasma emission patterns. This gives a general impression of the effectiveness of the method in modelling coronal structures and indicates what improvements may be attempted in the future.

We choose to model these features because they have simple three-dimensional macroscopic structure, some of which we can hope to reproduce using our simple method, and because the necessary magnetogram and plasma emission data files were available to us via Daniel Brown and Duncan Mackay (Univ. of St. Andrews) for the bright point and filament examples respectively and via the website of Sarah Gibson (Univ. of Cambridge; Gibson URL in references) for the sigmoid example. These data sets have all been used as the starting point for models calculated using well-known field line extrapolation techniques and so the field lines resulting from our tests can be verified against exact equivalents by Brown (1999), Mackay et al. (1997) and Gibson (web address in refs) while our self-consistent plasma patterns are the first of their kind and are to be compared only to observation. The flux tube example, however, is a simple test of the flexibility of the method. It is not based on any observational data but on a synthetically produced magnetogram. The example is designed to explore parameter regimes not successfully attempted in the other examples.

When presenting our example solutions we quote values used for the parameters α and ξ_0 . This information can only be interpreted in conjunction with details of how the problem has been scaled. For each example presented a length scale has been chosen

to keep the spatial arguments x , y and z of a reasonable size. Since in the expression for the magnetic field x , y and z are often multiplied or divided by α or $\sqrt{1 - \xi_0}$ there is a direct link between our lengthscale and the effect of α and ξ_0 on the solution. E.g. an example calculated using a large length scale would need a smaller value for α than the same example calculated with a smaller length scale to give it the same visible twist, since the values taken for x , y and z at each point are larger. For the examples presented in this chapter a length scale of 5000km has been chosen as with this scale the plasma profile figures seem to show an appropriate amount of structural detail.

4.4 Observations

Using a variety of observations of the solar atmosphere in conjunction with each other, we hope to understand better how its magnetic fields and plasma interact. We take both plasma emission and magnetic field data from instruments on the satellites Yohkoh, SoHO and TRACE as well as $H\alpha$ images from Big Bear Solar Observatory and the Ottawa River Solar Observatory and full-disc magnetograms from the Canadian National Solar Observatory.

In recent decades satellite-borne telescopes have revolutionised solar astronomy offering greater flexibility with spatial and temporal resolution and less interruption than is possible with ground-based telescopes. Solar satellites from the seventies and eighties include Skylab (1973), Solar Maximum (1980) and Spacelab 2 (1985), followed by Ulysses in 1990.

The Yohkoh (Solar-A) Mission is a Japanese solar mission with US and UK collaborators. It was launched in 1991 and carried soft and hard X-ray telescopes giving information about the hotter regions of the Sun: the corona and solar flares. Yohkoh's successor, Solar-B, is scheduled for launch in 2004 carrying optical, electromagnetic and X-ray instruments with the intention of investigating the relationship between the solar magnetic field and the corona. There may be a busy future for extrapolation techniques such as ours.

The Solar and Heliospheric Observatory (SoHO) is a cooperative mission between the

European Space Agency (ESA) and the National Aeronautics and Space Administration (NASA). SoHO was launched on December 2 1995 and was put into a halo orbit around the L1 Lagrangian point on February 14 1996. From here SoHO is able to observe the Sun from deep in its core to 32 solar radii, 24 hours a day with an angular resolution of 10 arcseconds.

The Transition Region and Coronal Explorer (TRACE) was launched on April 2 1998. Its launch was scheduled to allow joint observations with SoHO during the rise to the maximum of solar activity. TRACE is used to observe the photosphere through the transition region into the corona. These observations can be made with as little delay as a few seconds per image through the various wavelengths and with one arcsecond spatial resolution. TRACE explores the connections between the different layers of the solar atmosphere. While SoHO has the capability to produce images out to 32 solar radii, TRACE can produce images of high spatial resolution and temporal cadence. Together they allow simultaneous measurements of all the temperature regimes of the solar atmosphere. The Michelson Doppler Imager (MDI) on board SoHO gives a record of how, when and where the magnetic field emerges from or sinks below the solar surface. This record is important for understanding emission patterns from sources such as TRACE.

4.5 Green's Function Method Application: Solar Coronal Bright Point

From 13th-17th June 1998 TRACE and SoHO/MDI simultaneously observed the same quiet region of the sun. The TRACE image of an X-ray bright point and the MDI magnetogram of the same region at approximately the same time are shown in Figure 4.14 left and right respectively. As a simple example to illustrate the implementation and performance of our MHS extrapolation method we take the magnetogram and reconstruct the solar atmosphere using our solution method with this magnetogram as boundary data. We then compare the plasma structure of this solution to a near-simultaneous TRACE image. Our data set is chosen from a phase of evolution of the bright point when its structure is particularly simple and its evolution slow (its

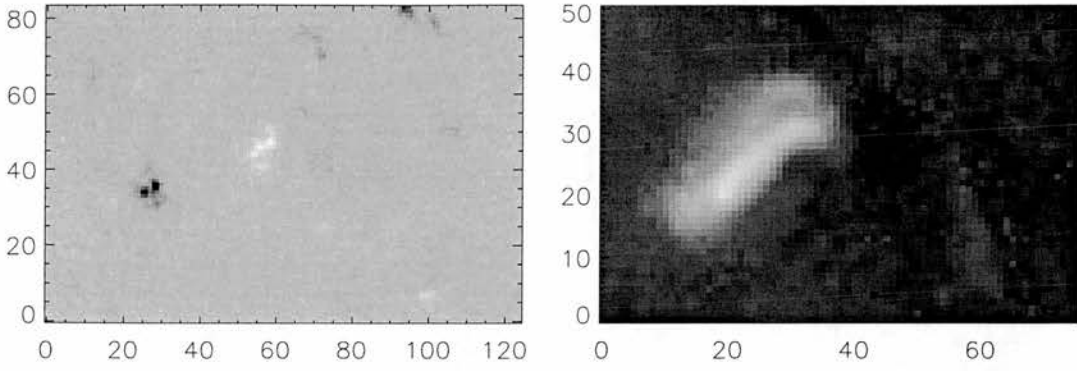


Figure 4.14: MDI magnetogram chunk (left) and near-simultaneous TRACE image (right)

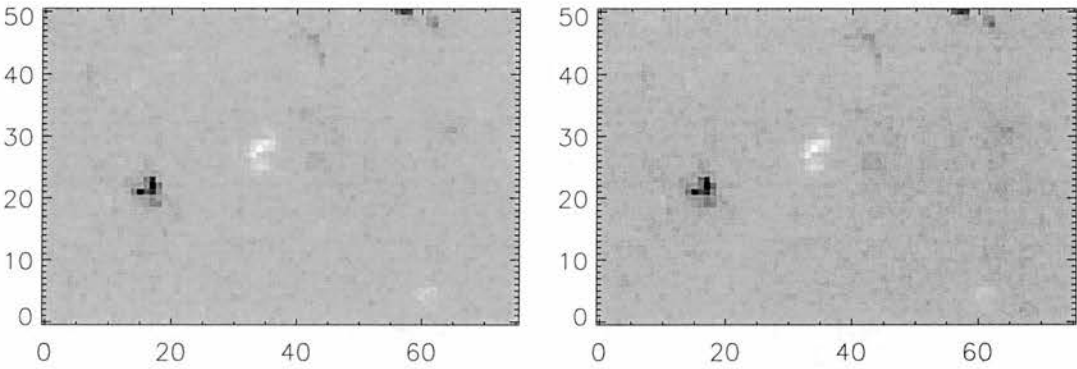


Figure 4.15: Reduced-resolution image of MDI magnetogram chunk (left) and fitted Green's function boundary profile (right)

appearance changes very little over two and a half hours) so that the system should be close to equilibrium.

Figure 4.15 shows the MDI magnetogram with resolution reduced to within the limit appropriate to the computational resources available to us (left), and the vertical component of the solution magnetic field (right). To confirm that the two pictures are nearly identical, the maximum residual between the two was calculated to be 3.04×10^{-6} kG, compared to an average field strength over all pixels of -2.936×10^{-4} kG. The reduced-resolution magnetogram now has a spatial resolution of 1arcsec^2 per pixel. The net

flux through this rectangle of photosphere calculated from the reduced-resolution magnetogram is $-5.998 \times 10^{18} \text{Mx}$ while the total flux is $2.309 \times 10^{20} \text{Mx}$ and so the flux is well-balanced.

Figure 4.16 shows field lines of our non-force-free model extrapolated from the magnetogram. Shown are field lines extrapolated from a grid above the negative flux patch (Figure 4.16, top pictures), from a grid above the positive flux patch (Figure 4.16, middle pictures) and the author's selection of field lines which best fit the shape of the bright point (Figure 4.16, bottom pictures). It is common practice when presenting an extrapolated field line model to select the field lines most closely resembling observations and to discard the rest, assuming that the plasma is structured only along these best-fitting field lines and so the modeller is only discarding those field lines that the plasma has already "discarded". This element of human intervention in the process gives us further motivation to calculate plasma models which may be more directly and completely compared to observations than is possible with a magnetic field model. Meanwhile, in future sections when presenting magnetic field models we show only the best-fitting field lines without commenting on those we prefer to ignore.

For the background model, we assume an ideal gas in hydrostatic equilibrium as in the worked example of Section 4.2 (see Equation (4.9)). We have however altered the background plasma model slightly from Section 4.2 to include a temperature minimum region. We have chosen a photospheric temperature of 6000K and a temperature minimum of 4300K at 500km (see Figure 4.17). With this new temperature profile Equation (4.9) must now be solved numerically for p_B .

On introducing the magnetic field to the model, the plasma pressure, density and temperature become three-dimensional functions of space. To show the three-dimensional structure of the data cubes we take sections in x and y through the volume of interest, designed to slice through the plasma structure we expect to form between the two flux patches (see Fig. 4.18). This three-dimensional structure can be seen in Figures 4.19-4.27.

The pressure contour plots of Figure 4.20 closely resemble the background pressure contour plot Figure 4.19 except for two small pressure maxima near the photosphere

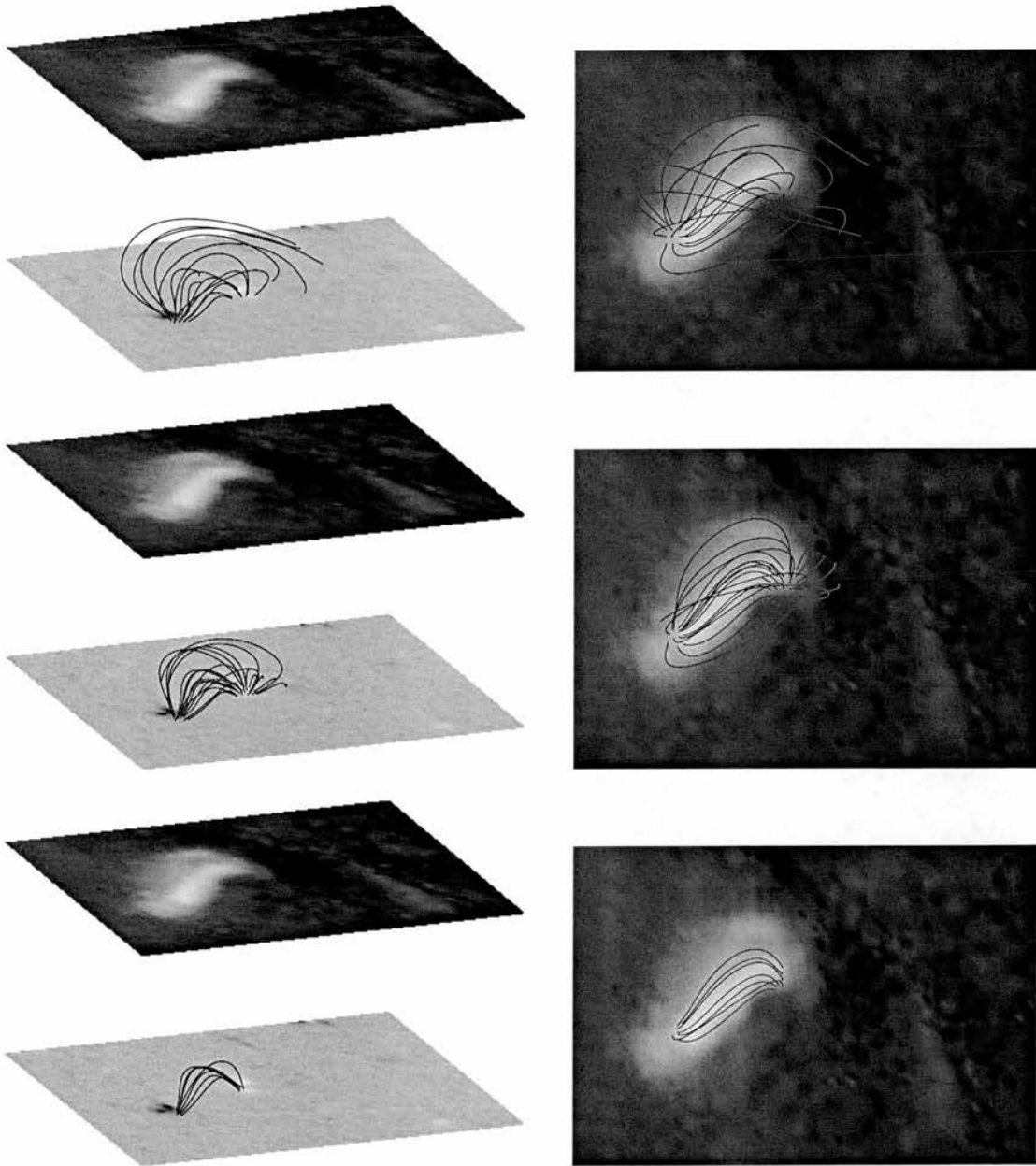


Figure 4.16: 3D field line plot on the MDI photosphere with the TRACE image drawn above for comparison (left pictures) and a view of the fieldlines from above superimposed on the TRACE image (right pictures). These pictures are intended to illustrate the process of field line selection by the modeller. The top pictures show field lines extrapolated from a grid above the negative flux patch, the middle pictures field lines from a grid above the positive patch and the bottom pictures show the best-fitting lines.

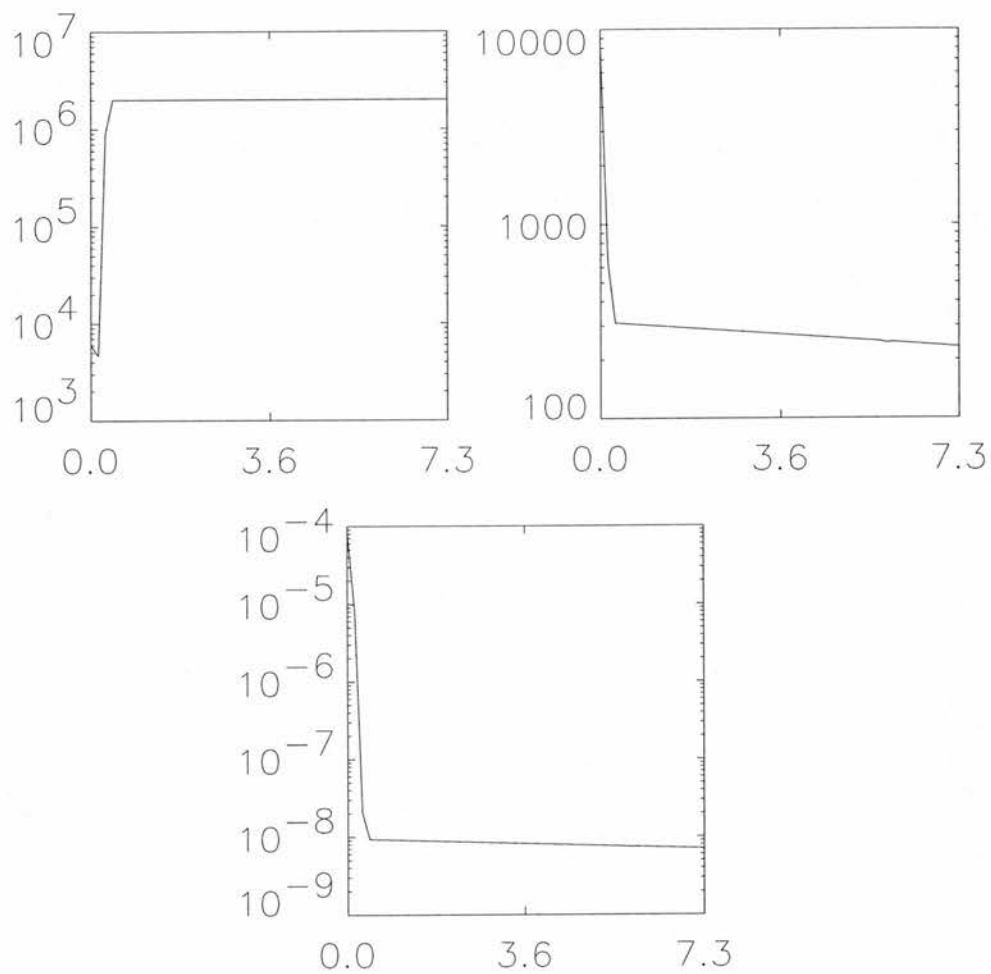


Figure 4.17: Background temperature (top left), pressure (top right) and density (bottom) (vertical axes) against height (horizontal axes). The length scale is 5000km.

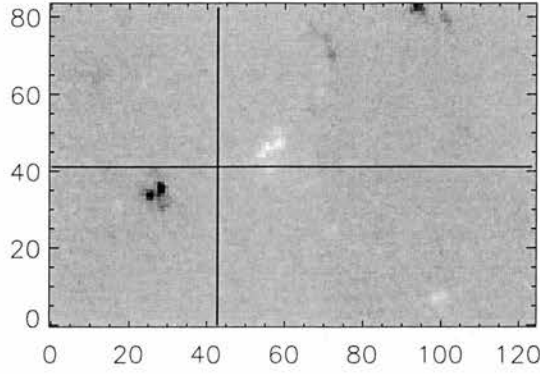


Figure 4.18: Sections $y = \text{const}$ and $x = \text{const}$ used in pressure, density and temperature contour plots (see Figs. 4.20, 4.23 and 4.26)

in the $y = \text{const}$ plot Figure 4.20 (left) where the $y = \text{const}$ section passes close to the two flux patches in Figure 4.18. These two pressure maxima can be clearly seen in the pressure isosurface Figure 4.21 where it is clear that each maximum lies directly above a flux patch. In this isosurface there is also a small pressure maximum corresponding to another flux patch at the top right of the magnetogram in Figure 4.14 (left). The pressure and density plots, Figures 4.22-4.27, show a different pattern and greater deviations from the background model. Compared to the background density plot of Figure 4.23, the density contour plots of Figure 4.23 show a single local region of maximum density in the vicinity of the flux patches as well as some smaller deviations from the background model elsewhere. The density isosurface plot of Figure 4.24 shows that this maximum density region connects the locations of the two flux patches as does the bright point in the TRACE emission pattern (Figure 4.14, right picture), although the maximum density region does not share the bright point's S-shape. Moreover the density isosurface Figure 4.24 shows another sizeable region of local maximum density and a couple of smaller ones all corresponding to flux patches in the magnetogram of Figure 4.14 (left) while there is no emission in Figure 4.14 (right) corresponding to these maxima. The temperature pattern shown in Figures 4.25-4.27 is very similar to the density pattern shown in Figures 4.22-4.24 because of the small deviation from background of the pressure, with its horizontal near-uniformity shown in Figures 4.20 and 4.21. The main difference is that the local extrema shown in Figures 4.25-4.27

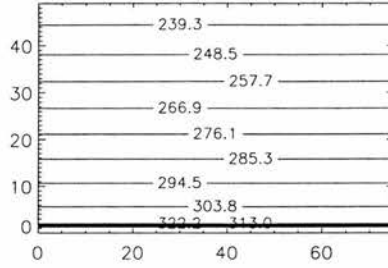


Figure 4.19: Background pressure variation

are temperature minima because, unlike the pressure and density, the background temperature model increases with height (above the temperature minimum which is very close to the photosphere - see Figure 4.17, top left).

Since the coronal pressure, density and temperature cannot be measured directly, we simulate an emission pattern to be compared directly with the TRACE image. We take as a proxy for the emission measure the expression (see Hundhausen, 1993)

$$I = \int T^{-\frac{1}{2}} \exp\left(-\frac{1}{T}\right) \rho^2 dl \quad (4.12)$$

where l is the coordinate along the line-of-sight and the integral is calculated from the photosphere to the top of the volume of interest. We calculate a two-dimensional intensity array by summing each z -direction column of the three-dimensional array

$$T^{-\frac{1}{2}} \exp\left(-\frac{1}{T}\right) \rho^2,$$

counting as zero any entries corresponding to $T < 10^6\text{K}$ or $T > 2 \times 10^6\text{K}$ since we do not expect plasma of temperature outside this range to be detected by the instrument on TRACE. Figure 4.28 shows the resulting intensity profile. Although the S-shape of the TRACE image is not emulated, there is clearly a confined region of maximum intensity

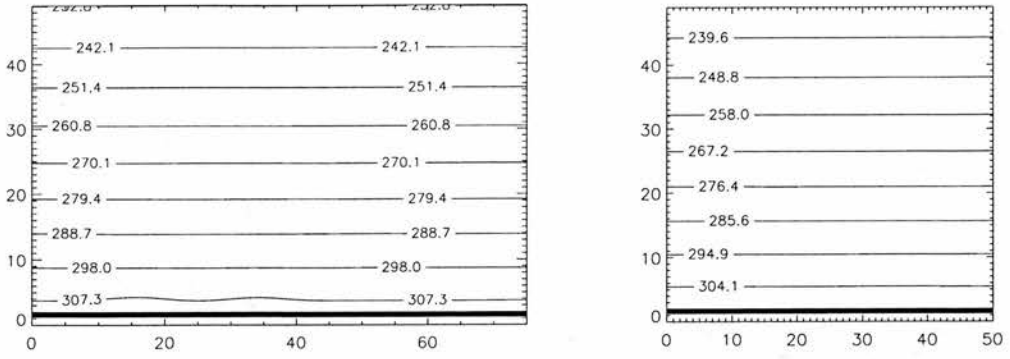


Figure 4.20: Pressure variation in plane $y = \text{const}$ (left) and $x = \text{const}$ (right).

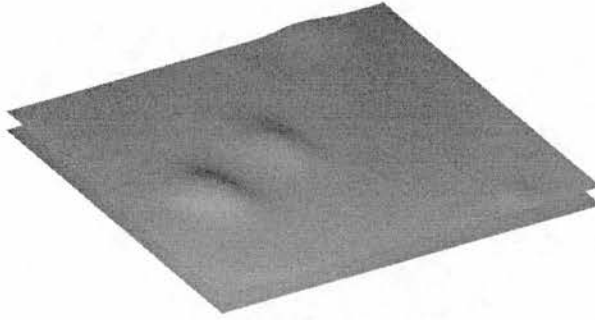


Figure 4.21: Pressure isosurface $p = 310.0 \text{ Nm}^{-2}$

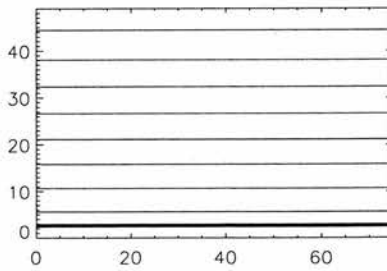


Figure 4.22: Background density variation

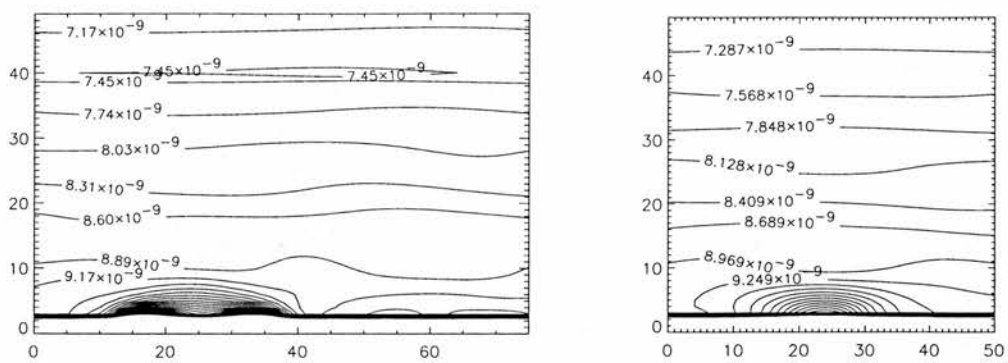


Figure 4.23: Density variation in planes $y = const$ (left) and $x = const$ (right).

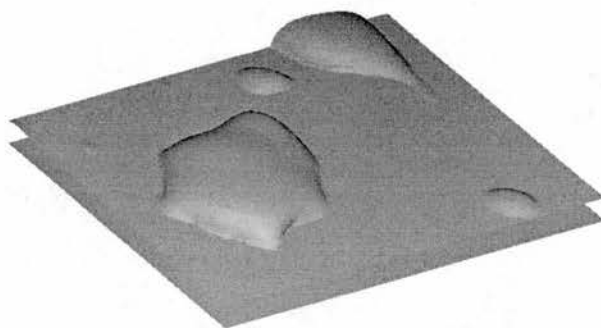


Figure 4.24: Density isosurface $\rho = 9.80 \times 10^{-9} \text{kgm}^{-3}$

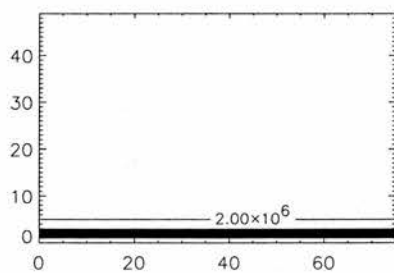


Figure 4.25: Background temperature variation

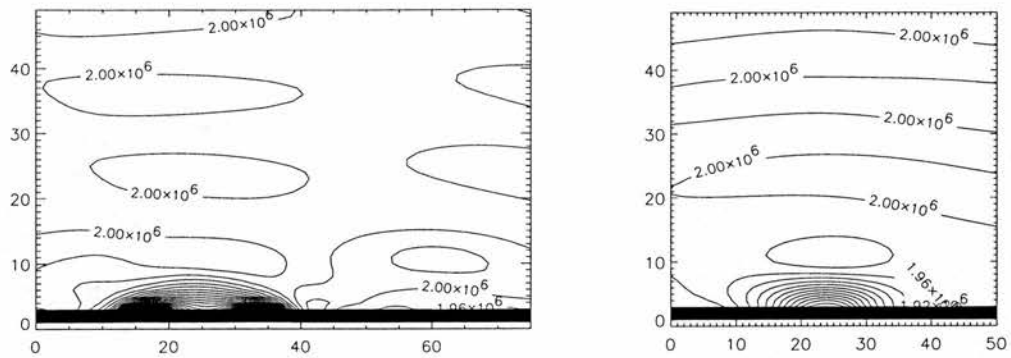


Figure 4.26: Temperature variation in planes $y = \text{const}$ (left) and $x = \text{const}$ (right).

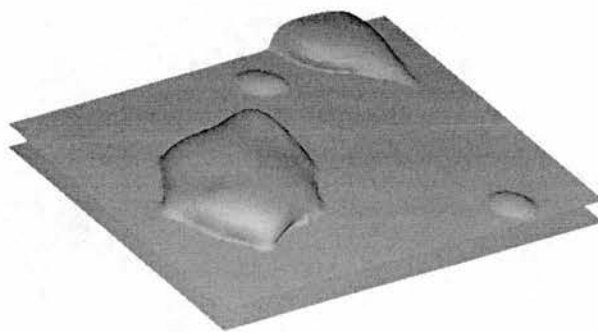


Figure 4.27: Temperature isosurface $T = 1.90 \times 10^6 \text{K}$

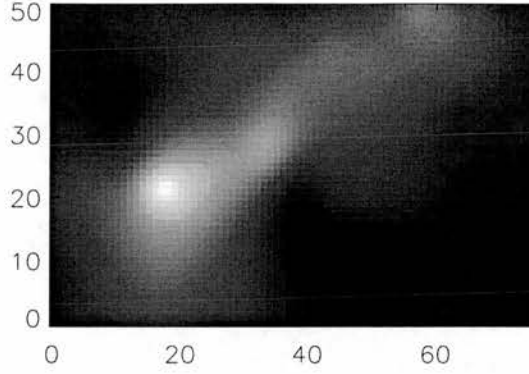


Figure 4.28: Intensity image artificially generated from calculated plasma arrays. Temperature range $1.0 - 2.0 \times 10^6 \text{K}$.

above the flux patches and the picture is not spoiled by intense region elsewhere, despite the occurrence of other local extrema in Figures 4.21, 4.24 and 4.27.

The calculated intensity is concentrated in the correct region but the S-shape of the TRACE image is not apparent. This is the best intensity image we were able to generate. Using the one-step temperature profile of Chapter 2 causes the intensity maximum region to be less clearly defined. Altering the background coronal temperature changes the intensity values but not the overall pattern. Changing α does not introduce any twisted appearance to the pattern but only makes it slightly narrower for lower α and slightly wider for higher α . We therefore use the value giving the best fit for the field-lines, $\alpha = 1.8$. We use $\xi_0 = -2.0$. A smaller value for ξ_0 confines the pattern more to the regions immediately above the flux patches, while a larger value causes the density and temperature to become negative, and the confined maximum intensity region becomes a less well-defined blob. A positive value of ξ_0 causes a local density minimum and a local temperature maximum above the flux patches and we no longer obtain a confined local intensity region. Only small positive values of ξ_0 are possible without the density becoming negative somewhere (see Equation(4.6)) and so a satisfactory model with a positive value for ξ_0 cannot be achieved.

4.6 Magnetohydrostatic Green's Function Method Application: Formation of a Solar Coronal Filament

4.6.1 Introduction

The application so far has involved a magnetogram with relatively weak field strengths. The magnetogram has been spatially averaged and does not represent the small-scale intense magnetic flux concentration believed to exist on the photosphere. The application for the method presented in this section is derived from work by Mackay et al. (1997), who modelled the formation of a filament channel between July 21 and July 25 1979 using a linear force-free extrapolation method on a magnetogram from a ground-based telescope at Kitt Peak Observatory. The magnetogram includes regions of field strength of around a kilogauss. The changes of field line connectivity over this period were assumed by the authors to be responsible for the development of the filament channel (see Figure 4.29 (bottom left)). Extrapolated fieldlines were found to match near-simultaneous $H\alpha$ images for 22 and 25 July, but for a different value of force-free parameter α on each day (3.0 and 2.3 respectively). Using the same value for α on each day made a good field line-fibril fit for both days impossible. Our aim in this section is to model the structuring of the plasma by the non-force-free magnetic field extrapolated by our Green's function method from photospheric line-of-sight magnetogram data from Kitt Peak Observatory. Although we cannot model the non-adiabatic physics of filament formation by this method, it is instructive to see how the method reconstructs the solar atmosphere from the magnetograms in the light of what is observed via $H\alpha$ to have occurred.

Figure 4.29 shows the magnetograms and the $H\alpha$ images. Figure 4.30 shows the magnetograms with their resolutions reduced to 67×44 and 76×44 pixels in preparation for applying the Green's function method, and the boundary profile of the extrapolated Green's function solution. The maximum residuals are found to be 6.74×10^{-6} kG and 4.77×10^{-6} kG compared to average field strengths of 1.23×10^{-3} kG and 3.97×10^{-3} kG. The spatial resolution of these reduced magnetograms is now 9arcsec^2 per pixel and 30.25arcsec^2 per pixel. The net magnetic flux out of the photospheric region calculated from the reduced magnetograms is -1.71×10^{20} Mx and -2.12×10^{21} Mx, compared to

a total flux of 6.14×10^{21} Mx and 9.36×10^{21} Mx. The July 22 magnetogram appears to have very good flux balance suggesting that the region is isolated, while the July 25 magnetogram has a significant imbalance implying that the region is connected by magnetic field to other regions (in their Sections 4 and 5, Mackay et al. (1997) compensate for this imbalance by placing positive sources outside the region of interest where they know some positive flux existed at the time from a synoptic magnetogram - we instead retain the flux imbalance). Our figures for the net flux through the July 22 and 25 magnetograms compare with the figures 3×10^{18} Mx and 1.74×10^{21} Mx calculated by Mackay et al. (1997) from the magnetograms at their original full resolution. The differences between our figures and theirs are likely to be due to our failure to pick up some small-scale magnetic features in our reduced-resolution magnetograms which are present in the originals. Also, in the July 22nd example we use some solar surface area not used by Mackay et al. (1997) (see their Figure 3, top).

The extrapolated solution is calculated at gridpoints of $67 \times 44 \times 50$ and $76 \times 44 \times 50$ pixel numerical boxes respectively. The reduced-resolution July 22 magnetogram has only a small flux imbalance, suggesting that we are working with an isolated system. The system is known to have emerged two days previously and perhaps has not had time to interact significantly with regions nearby. Hence following Mackay et al. (1997) a reasonable model of this region in isolation is expected and we discuss our attempt at this in Subsection 4.6.2. On 22-24 July mass is observed to accumulate at the location where the filament is to form (see Figure 4.29, bottom right) while on 23-25 July the active region of Figure 4.29 (top right) is observed to decay, although it is still visible towards the top right corner of the bottom right picture of Figure 4.29. The alignment of the fibrils which then form the filament takes place quickly on the emergence of the new active region. This all suggests that the emergence of the active region and the formation of the filament are related events and, following Mackay et al. (1997) we choose to model the situation on July 25 including the new active region, the filament and indeed all regions of flux in Figure 4.29 (bottom left). We discuss this model in Subsection 4.6.3

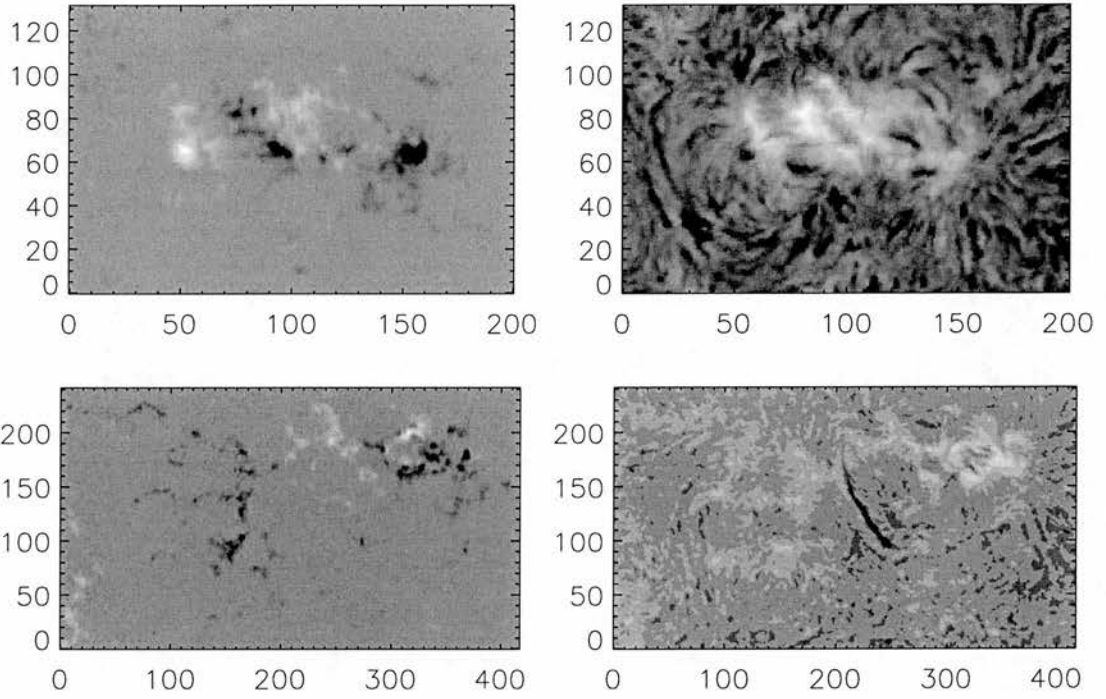


Figure 4.29: Kitt Peak magnetogram chunk from July 22 (top left), near-simultaneous H-alpha image (top right), Kitt Peak magnetogram chunk from July 25 (bottom left), near-simultaneous H-alpha image (bottom right)

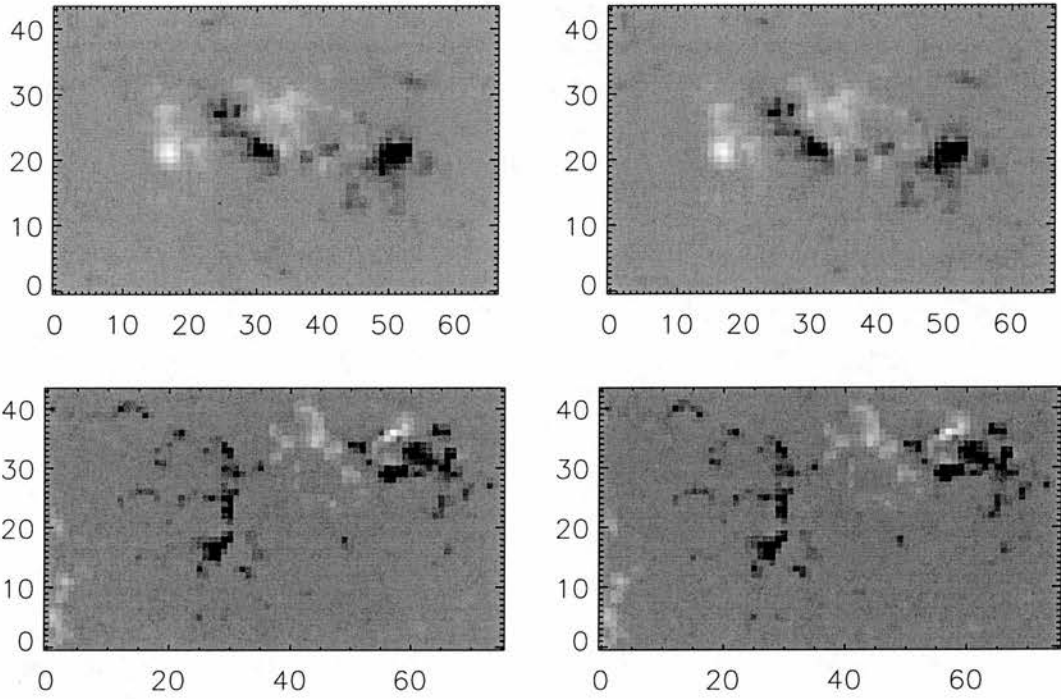


Figure 4.30: Reduced-resolution image of July 22 Kitt Peak magnetogram chunk (top left), fitted Green's function boundary profile (top right), reduced-resolution image of July 25 Kitt Peak magnetogram chunk (bottom left) and fitted Green's function boundary profile (bottom right).

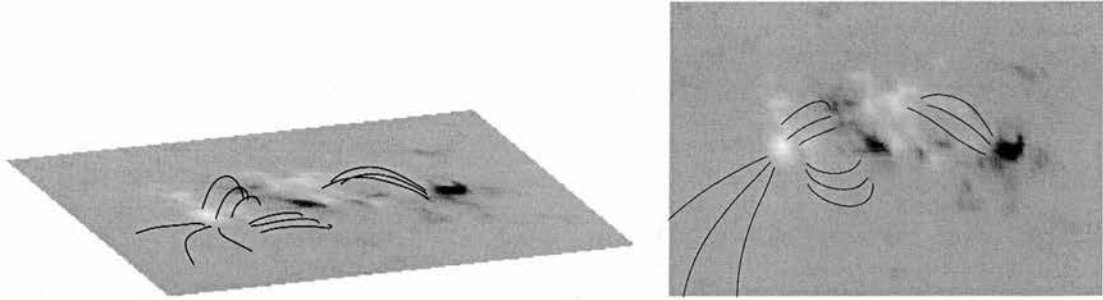


Figure 4.31: 3D potential field line plot on Kitt Peak photosphere (left) and view of potential field lines from above on magnetogram (right).

4.6.2 Model for July 22 1979

To give an idea of the coronal magnetic field structure, some extrapolated field lines are displayed in Figures 4.31, 4.32 and 4.33 for a potential, linear force-free and linear non-force-free model respectively. The potential model is found to resemble the $H\alpha$ image of Figure 4.29 most with the low-lying set of short field lines on the right, while the linear force-free and non-force-free models better mimic the curved filaments at the left edge of the $H\alpha$ image as in the force-free model of Mackay et al. (1997) for a very different value of α , 0.5 here instead of 3.0. Two possible reasons for this are that Mackay et al. (1997) fit their solution not to the magnetogram itself, but to an idealised representation of the magnetogram built up from two-dimensional Gaussian surfaces and they use a method which implements boundary conditions at the edges of their region forbidding any field lines to leave the volume directly above the magnetogram. This is the same numerical method used by Finn et al. (1994) to show that a linear force-free equilibrium's field line topology is very sensitive to the value of force-free parameter used, a result relevant to this project as will become apparent. We remark that we also find comparable field lines when we use higher values of α such as 3.0 but then the density and pressure contours and isosurfaces acquire an unrealistic vertically periodic appearance.

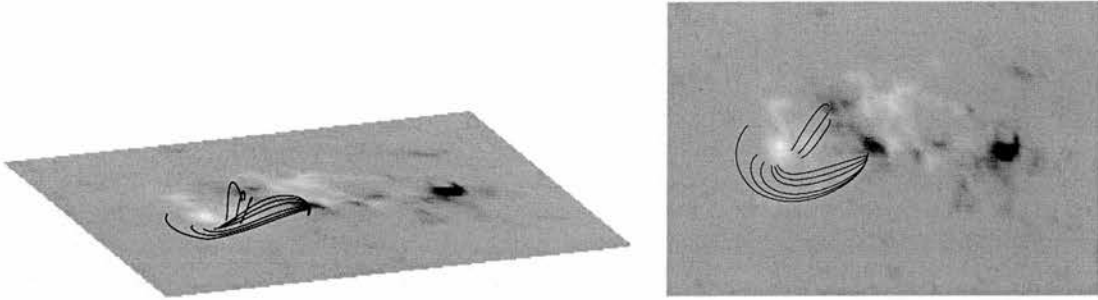


Figure 4.32: 3D linear force-free field line plot for $\alpha = 0.5$ on Kitt Peak photosphere (left) and view of linear force-free field lines from above on magnetogram (right).

The non-force-free current changes the magnetic field only negligibly because the non-force-free parameter value used ($\xi_0 = -0.1$) is small.

Figure 4.34 shows the sections taken through the volume of interest to generate the two-dimensional contour plots of Figures 4.35, 4.37 and 4.39. Figures 4.35 and 4.36 show a local pressure maximum corresponding to each of the four major areas of flux, while polarity inversion lines ($B_z = 0$) have background pressure (see Equation 4.5).

Figure 4.37 shows an increase in density over background occurring immediately above photospheric regions of large flux.

Figure 4.38 reveals two local density maxima near the photosphere dividing the quadropolar system into two bipolar regions. It may be that a high-temperature measurement would pick up such a pattern but the $H\alpha$ image of Figure 4.29 (top right) shows no such pattern.

Figure 4.39 shows a decrease in temperature from background occurring immediately above photospheric regions of large flux while Figure 4.40 shows that two local temperature minima near the photosphere divide the quadropolar system into two bipolar regions as is the case with the density. A third temperature minimum and density maximum region is visible between the two bipolar systems and above the photosphere, but this is likely to be due to a weakness in the constant- ξ Green's function method since

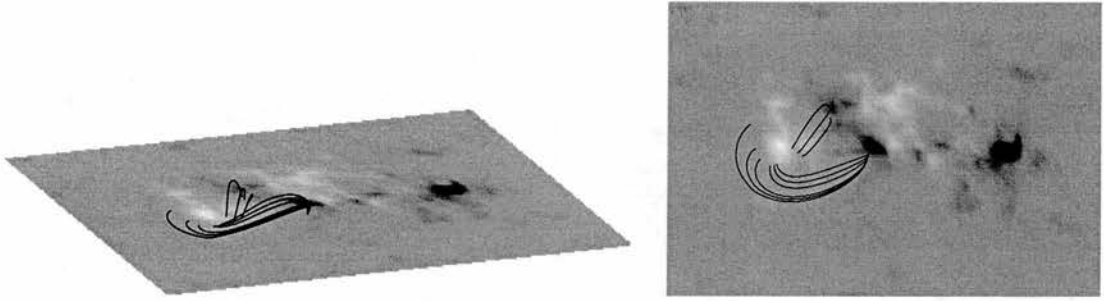


Figure 4.33: 3D linear non-force-free field line plot for $\alpha = 0.5$, $\xi_0 = -0.1$ on Kitt Peak photosphere (left) and view of field lines from above on magnetogram (right).

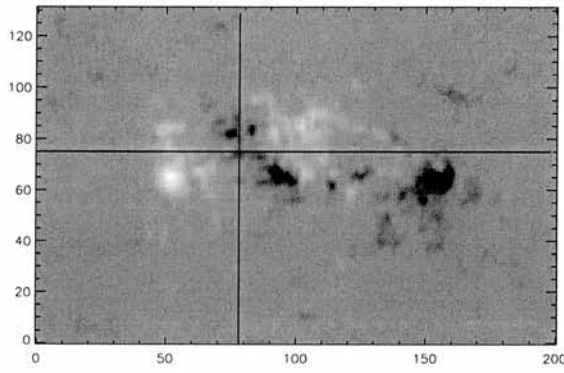


Figure 4.34: Sections $y = const$ and $x = const$ used in pressure, density and temperature contour plots (see later)

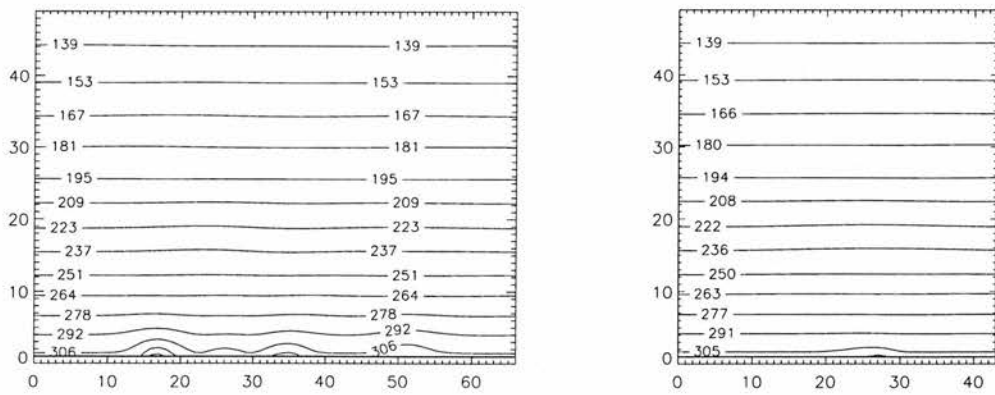


Figure 4.35: Pressure variation in plane $y = const$ (left) and $x = const$ (right).

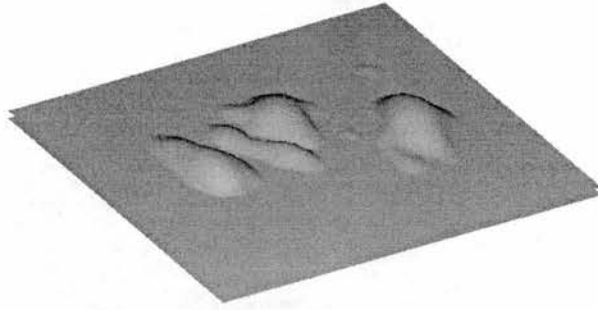


Figure 4.36: Pressure isosurface $p = 310.0\text{Nm}^{-2}$

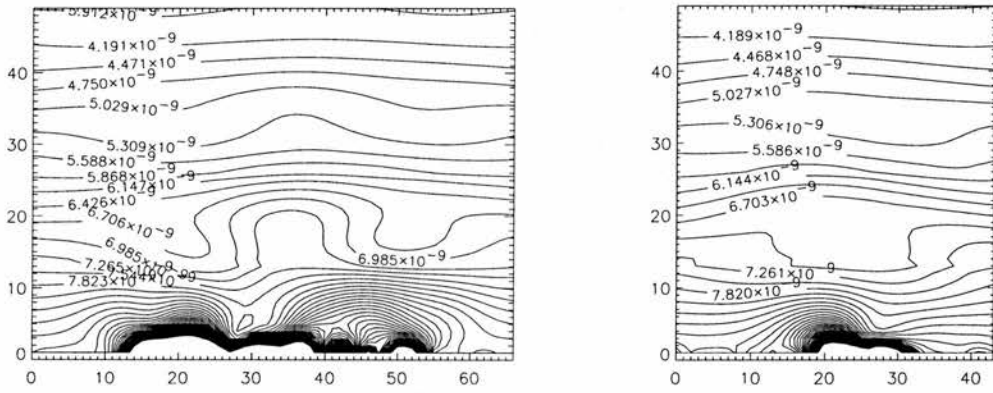


Figure 4.37: Density variation in planes $y = \text{const}$ (left) and $x = \text{const}$ (right).

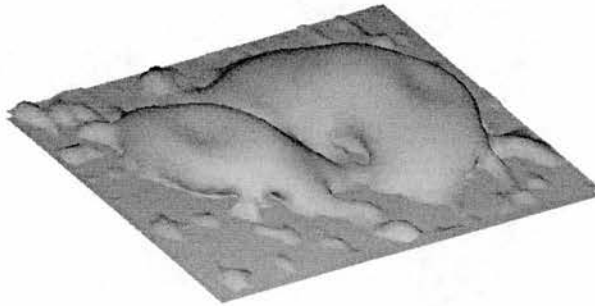


Figure 4.38: Density isosurface $\rho = 9.40 \times 10^{-9}\text{kgm}^{-3}$

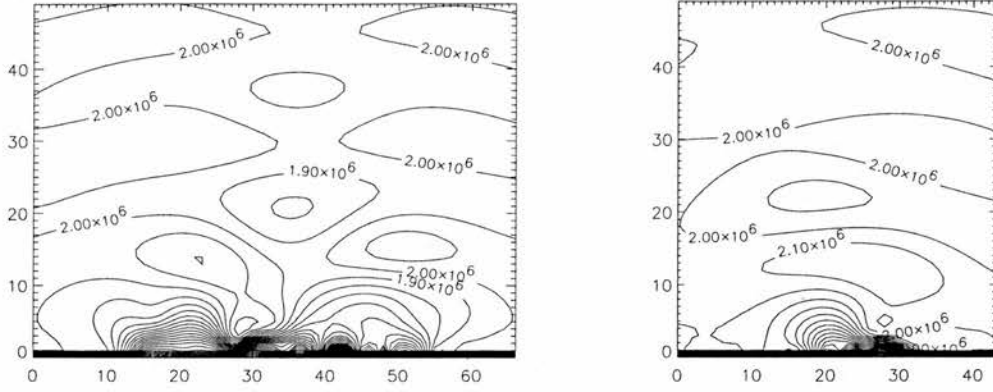


Figure 4.39: Temperature variation in planes $y = \text{const}$ (left) and $x = \text{const}$ (right).

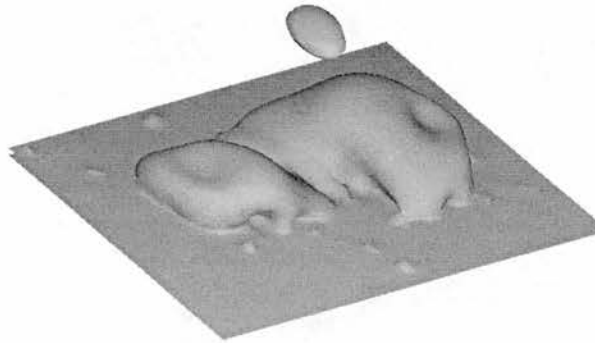


Figure 4.40: Temperature isosurface $T = 1.80 \times 10^6 \text{K}$

the equilibrium solution loses physical validity with increasing distance from the photosphere. It is likely that with the exponential- ξ Green's function we will achieve a greater disruption of the plasma close to the photosphere by the magnetic field than is possible with the constant- ξ method without negative densities or unexpectedly large deviations from the background pressure, density and temperature models appearing, and so this anomaly will be overcome.

4.6.3 Model for July 25 1979

We extrapolate a non-force-free coronal model from the large-area July 25 magnetogram of Figure 4.29 (bottom left) using parameter values $\alpha = 0.0$ and $\xi_0 = -0.5$. Figure 4.41

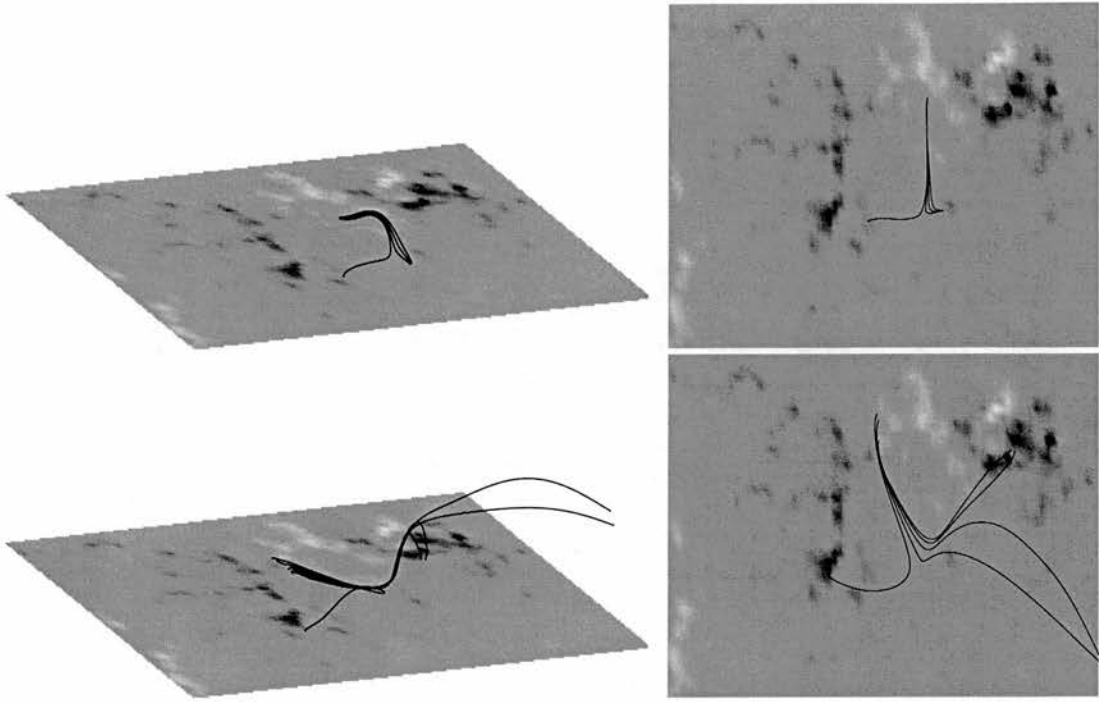


Figure 4.41: 3D field line plot on Kitt Peak photosphere (left) and view of linear force-free field lines from above on magnetogram (right) for $\alpha = \xi_0 = 0.0$ (top) and $\alpha = 0.3$, $\xi_0 = -0.5$ (bottom).

shows plots of extrapolated field lines. None of the major regions of flux is isolated. A set of long, densely packed parallel field lines where the filament should form is shown. Also shown in Figure 4.41 are field lines for the case $\alpha = 0.3$ which hint strongly at modelling the filament. There is also a strong indication of a magnetic null point beyond the bottom end of the filament. The fieldlines of Figure 4.41 (top) closely resemble those close to a potential three-dimensional radial null (see Parnell et al. (1996) Figure 5) while the field lines of Figure 4.41 (bottom) resemble a non-potential three-dimensional null with a relatively small parallel current through it (Parnell et al. (1996) Figure 6). Figures 4.43-4.48 show the non-force-free plasma structure for this case.

We display the plasma structure of the non-force-free model with $\alpha = 0.3$ and $\xi_0 = -0.5$. Figure 4.42 shows the sections taken through the volume of interest to generate the two-dimensional contour plots Figures 4.43, 4.45 and 4.47 for the pressure, density and temperature of the extrapolated coronal atmosphere. These sections are chosen to

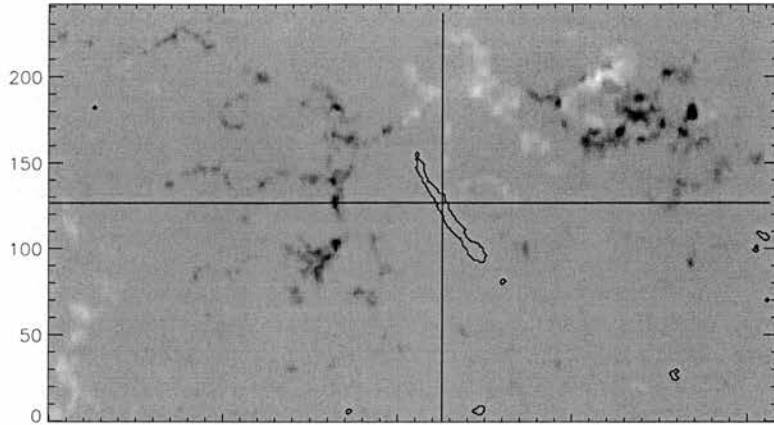


Figure 4.42: Sections $y = \text{const}$ and $x = \text{const}$ used in pressure, density and temperature contour plots (see later). Also shown is an outline of the filament of Figure 4.29, bottom right. The sections are intended to cross the location of the observed filament.

intersect at the location of the filament so that any success in modelling the filament by the plasma model may be picked up by the contour plots.

Figures 4.43 and 4.44 show that there is a weak local pressure maximum region corresponding to each of the three large flux regions.

Figures 4.45 and 4.46 show a single large local maximum density region covering all of the significant regions of flux apart from the area at the bottom left.

Because the pressure is nearly uniform horizontally, the contours and isosurfaces of Figures 4.47 and 4.48 for the temperature closely resemble those for the density, except that they indicate local temperature minima and not maxima. The density and temperature contour plots of Figures 4.45 and 4.47 do not give any clear indication of the local density maximum and temperature minimum profile of a filament where one is expected, but it is difficult to draw conclusions from these low-resolution plots where the structure near the photosphere does not appear to be well resolved.

We do not give a synthetic plasma pattern calculated from our model for direct comparison with the $H\alpha$ images of Figure 4.29. The chromospheric structures seen in $H\alpha$ as dark structures against the bright emission of the photosphere are visible in this way because they absorb the photospheric emission, and we are not yet able to model this

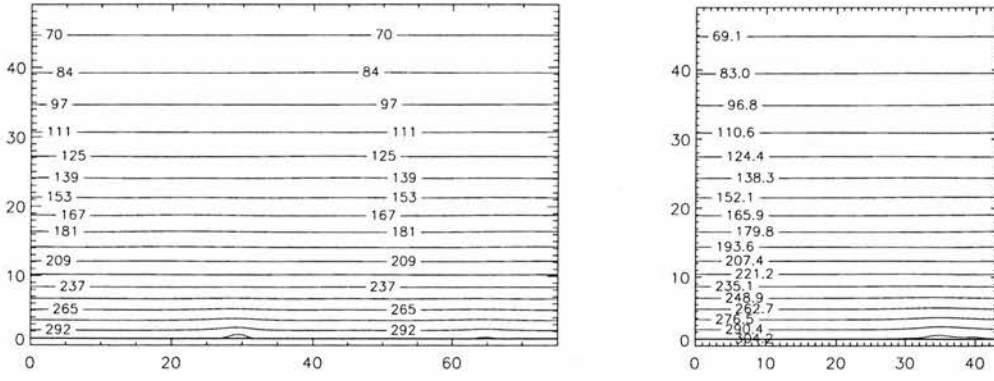


Figure 4.43: Pressure variation in plane $y = \text{const}$ (left) and $x = \text{const}$ (right).

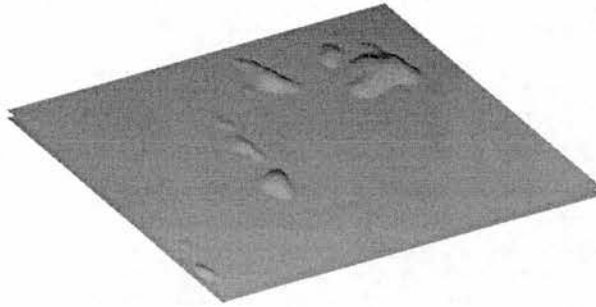


Figure 4.44: Pressure isosurface $p = 310.0 \text{Nm}^{-2}$

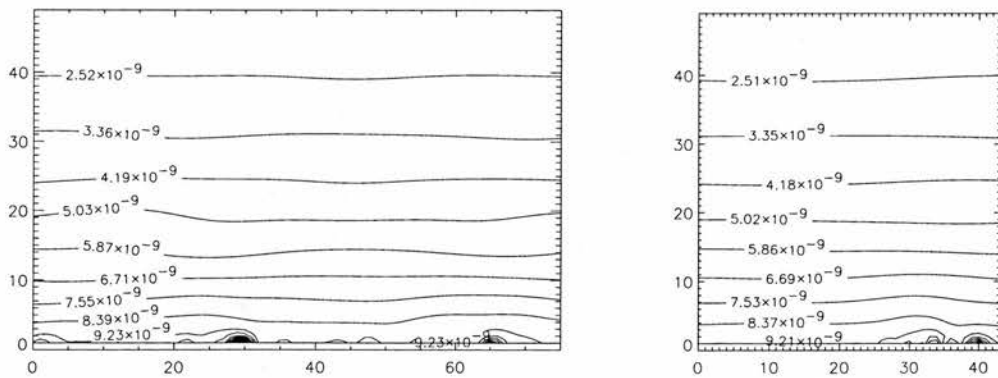


Figure 4.45: Density variation in planes $y = \text{const}$ (left) and $x = \text{const}$ (right).

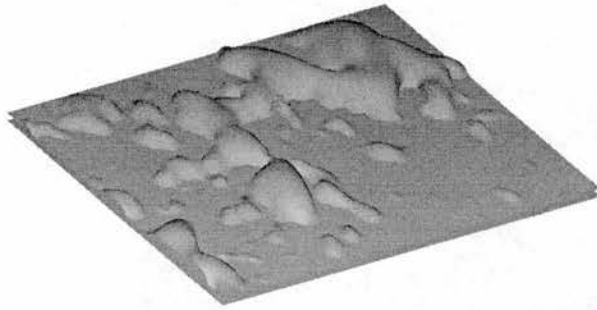


Figure 4.46: Density isosurface $\rho = 9.40 \times 10^{-9} \text{kgm}^{-3}$

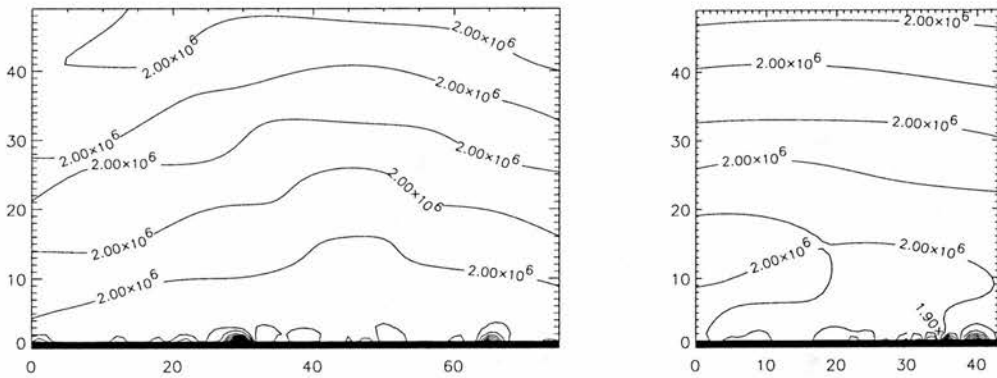


Figure 4.47: Temperature variation in planes $y = \text{const}$ (left) and $x = \text{const}$ (right).

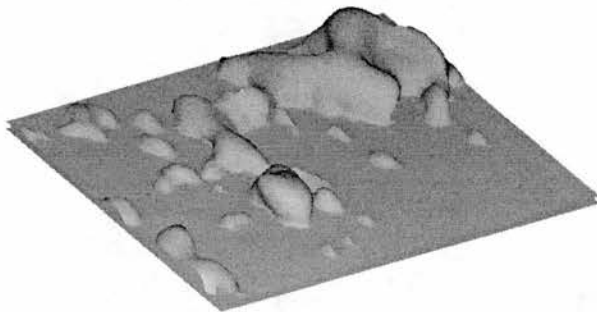


Figure 4.48: Temperature isosurface $T = 1.90 \times 10^6 \text{K}$

process. Attempts have been made to find signatures of a filament in our density and temperature arrays corresponding to the filament in Figure 4.29 (bottom right), but no significant deviation from the background model was found there. We hope that a future model with higher resolution and a more sophisticated Green's function will be more successful in picking up the filament. In this example the resolution of the magnetogram is reduced by a factor of 5.5 in each direction. This may have spoilt our chances of picking up from the magnetogram such a long, thin structure as a filament. Although the field line model did adequately model the filament, the technique in its present form is only suitable for modelling macroscopic structure and a run at a higher resolution would have more chance of modelling the filament. Furthermore a technique using a more sophisticated Green's function, e.g. that given by Equations (3.75-3.77) with an exponential form for ξ would allow more non-force-free effects in the lower atmosphere without becoming unphysical elsewhere. It may be that this increased flexibility will enable us to model the filament.

4.6.4 Discussion

Direct comparison of Figures 4.35-4.40 with Figures 4.43-4.48 reveals a significant change in the relationship between the flux regions involved. In Figures 4.35-4.40 the quadrupolar region appears to be divided into two distinct bipolar regions while in 4.43-4.48 the same quadrupolar region is undivided and indeed is connected with most of the other major flux regions in the larger solar surface area encompassed by this model. This pattern is also evident in the field line plots where there appears to be more interconnectivity between regions of flux in Figure 4.41 than in Figure 4.33. Some change in the connectivity may be attributed to the different value of α used for the two examples, 0.5 compared with 0.3. As Hudson and Wheatland (1999) demonstrate, altering the force-free parameter in a system may significantly change its magnetic field connectivity while Finn et al. (1994) describe how changing this parameter may change the kinkedness or even the knottedness of a fieldline. Since we have achieved successful field line-fibril fits for 22 and 25 July at the location of the filament's formation for different values of the force-free parameter and by isolating the recently-emerged active region for 22 July while including broader interaction between

regions on 25 July, we conclude that between 22 and 25 July the newly emerged region interacts with neighbouring regions generating the straight filament-like fieldlines seen in Figure 4.41 (bottom) changing both the kink and connectivity properties of the magnetic field. We have therefore been able to find a change in the relationship among flux regions occurring between July 22 and July 25 as did Mackay et al. (1997), by applying our non-force-free Green's function method directly to the magnetograms. We were unable to model the filament itself having tried many combinations of values for the parameters α and ξ_0 . A future attempt without reducing the resolution of the magnetogram and using a more sophisticated Green's function (see Chapter 3) may be more successful.

4.7 Green's Function Method Application: Sigmoid-like Structure

On 19th August 1999 Yohkoh SXT observed a sigmoid structure for which near-simultaneous MDI data are available. Some effort has been put into reconstructing the solar atmosphere from magnetogram data using potential, linear force-free, nonlinear force-free and linear non-force-free field extrapolation methods (see Gibson, URL in references). Liu, Zhao & Hoeksema have calculated potential, linear force-free and linear non-force-free models using line-of-sight SoHO/MDI magnetogram data which we go on to use in this section, as well as a nonlinear force-free model using a vector magnetogram from Huairou Solar Observing Station. Meanwhile Mandrini & Schmieder have calculated potential and linear force-free models. These models can be viewed at Gibson (URL in references).

Figure 4.49 shows the SXT image from August 19 (left) extracted from a full-disk image, showing the sigmoid-shape structure. Also shown (right) is a near-simultaneous magnetogram extracted from a full-disk magnetogram from SoHO/MDI. This displays the measured line-of sight magnetic field component on the photospheric region under the sigmoid-like structure. There is a large, strong magnetic flux patch near the centre of the magnetogram chunk with smaller patches scattered around.

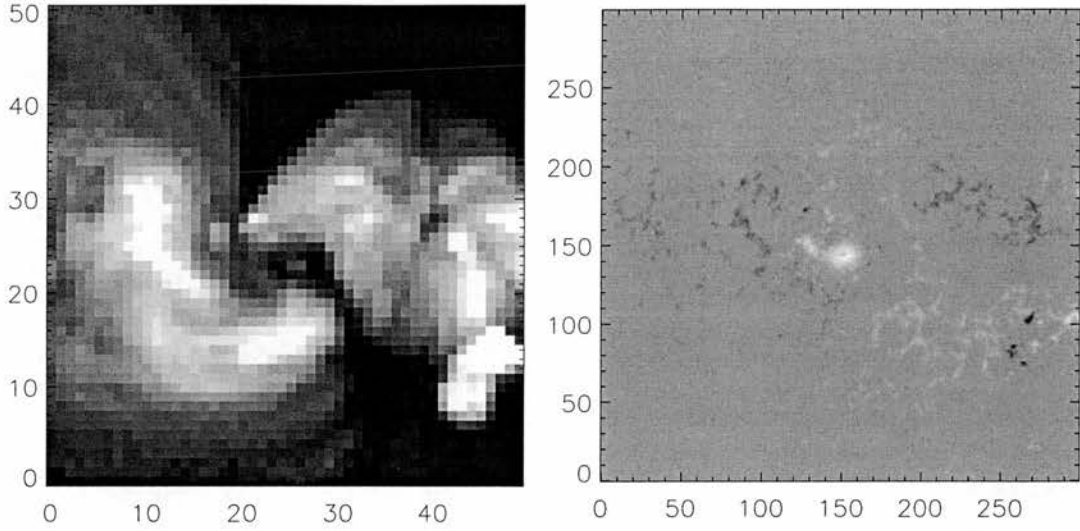


Figure 4.49: Yohkoh SXT image (left) and near-simultaneous MDI magnetogram chunk (right)

We reconstruct the magnetic field as a potential field, a linear force-free field and a linear non-force-free field respectively using the MDI line-of-sight magnetogram. Figure 4.50 shows the magnetogram with resolution reduced from 300×300 pixels to 60×60 pixels (left) and the vertical component of the extrapolated non-force-free solution over $z = 0$ for direct comparison (right). The maximum residual between the two was calculated to be 1.56×10^{-5} kG, compared to an average field strength over all pixels of 6.50×10^{-3} kG. The reduced-resolution magnetogram has a spatial resolution of 25arcsec^2 per pixel. The net flux through this rectangle of photosphere calculated from the reduced-resolution magnetogram is 6.17×10^{20} Mx while the total flux is 2.37×10^{21} Mx and so there is a significant positive flux imbalance and it will not be surprising if some extrapolated field lines leave the region.

The coronal atmosphere is extrapolated into a numerical box of $60 \times 60 \times 60$ pixels. Figures 4.51, 4.52 and 4.53 show illustrative field lines from the potential, linear force-free and linear non-force-free extrapolations respectively. The fieldline plots resemble those extrapolated by Liu, Zhao & Hoeksema and Mandrini & Schmieder (see Gibson, URL in references) from the same set of data using different fieldline extrapolation codes. The potential field lines can be seen to be less tightly packed together than the

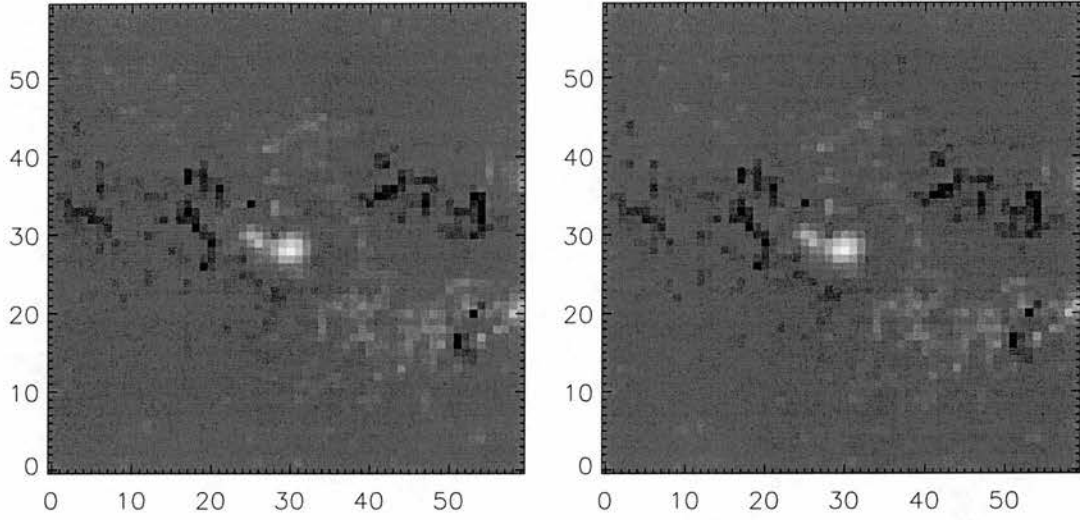


Figure 4.50: Reduced-resolution image of MDI magnetogram chunk (left) and fitted Green's function boundary profile (right)

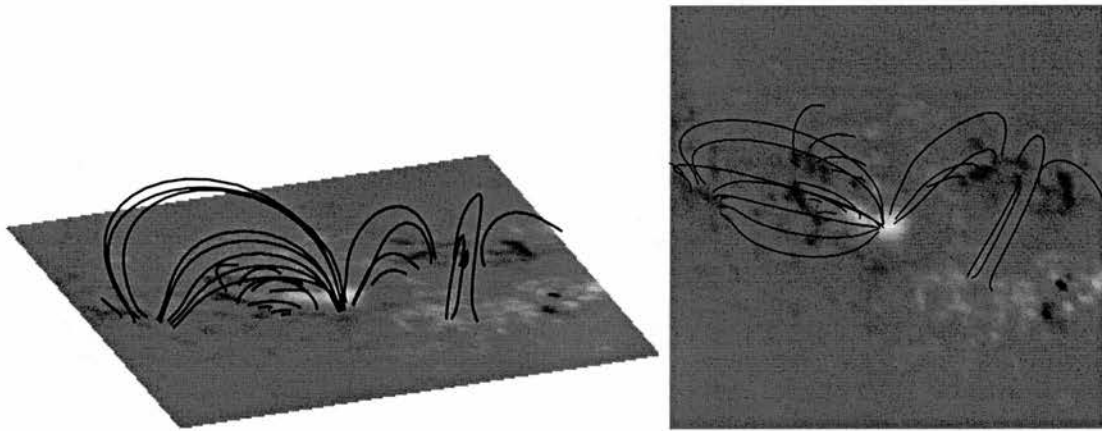


Figure 4.51: 3D potential field line plot on MDI photosphere with BBSO H alpha image drawn above for comparison (left), and view of field lines from above on MDI magnetogram (right).

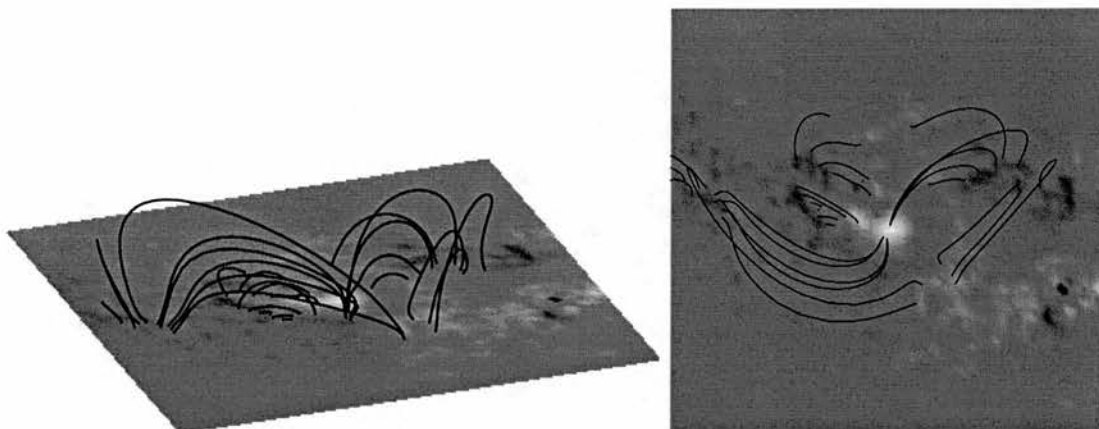


Figure 4.52: 3D linear force-free field line plot ($\alpha = -0.03$) on MDI photosphere with BBSO H alpha image drawn above for comparison (left), and view of field lines from above on MDI magnetogram (right).

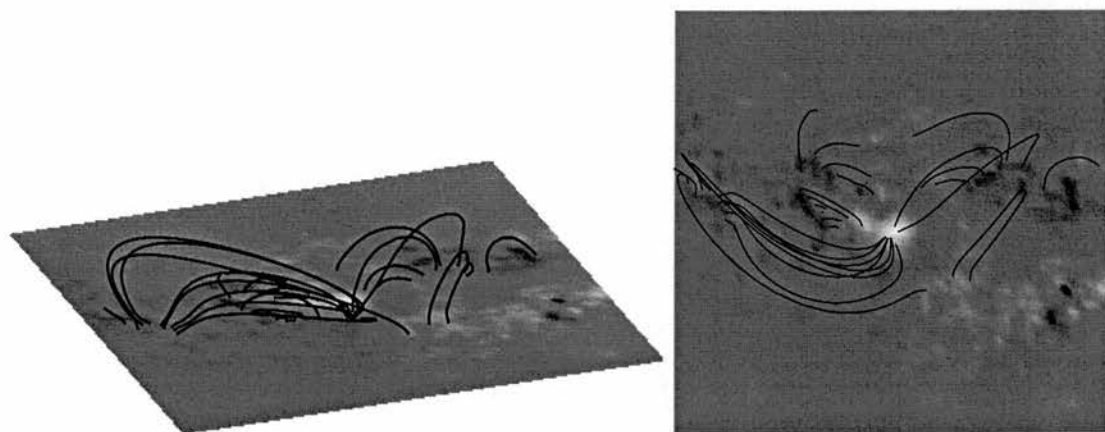


Figure 4.53: 3D linear non-force-free field line plot ($\alpha = -0.04$, $\xi_0 = -0.16$) on MDI photosphere with BBSO H alpha image drawn above for comparison (left), and view of field lines from above on MDI magnetogram (right).

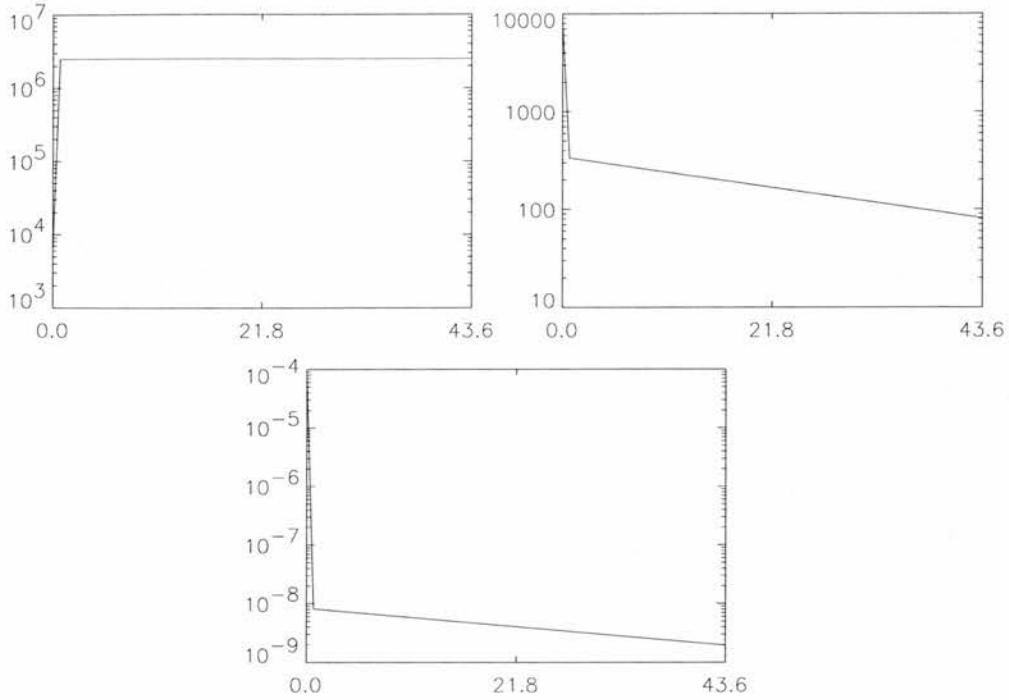


Figure 4.54: Background temperature (top left), pressure (top right) and density (bottom) (vertical axes) against height (horizontal axes). The length scale is 5000km.

linear force-free and linear non-force-free field lines. The potential field lines do not follow the curves of the sigmoid shape of Figure 4.49 (left) while the linear force-free and linear non-force-free lines roughly follow part of the structure. Comparing Figures 4.52 and 4.53 the best-fitting linear force-free and linear non-force-free models are obtained for different values of α , -0.03 and -0.04 respectively, owing to the relatively large value for ξ_0 , -0.16 , possible in the non-force-free model. The effect of this large value for the non-force-free parameter can be seen by comparing the left pictures of Figures 4.52 and 4.53 where gravity can be seen to have pushed the non-force-free field lines significantly lower than the force-free field lines.

We have altered the background plasma from the previous models in this chapter in fixing the coronal temperature at the higher value of 2.5×10^6 K (as opposed to 2×10^6 K) since we are modelling a hot active region emitting soft X-rays. We have again chosen a photospheric temperature of 6000K and a temperature minimum of 4300K at 500km (see Figure 4.54).

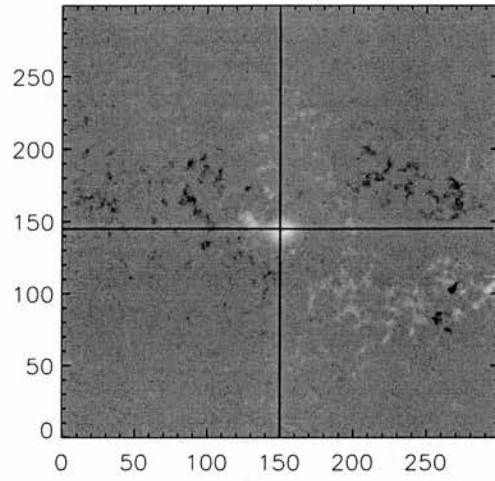


Figure 4.55: Sections $y = \text{const}$ and $x = \text{const}$ used in pressure, density and temperature contour plots (see later)

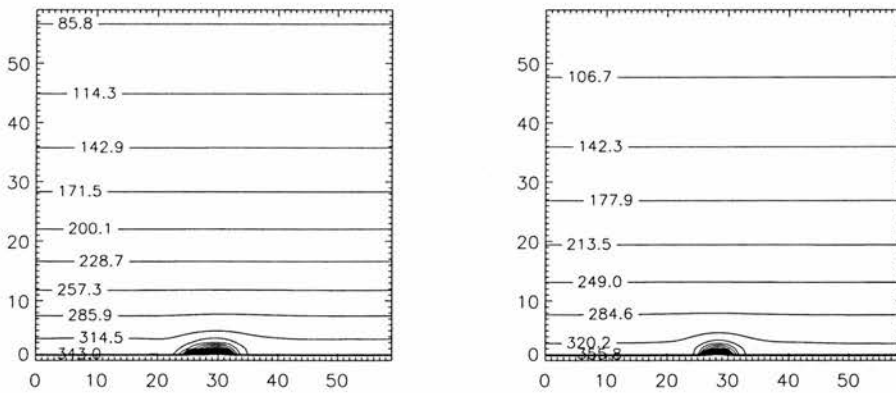


Figure 4.56: Pressure variation in planes $y = \text{const}$ (left) and $x = \text{const}$ (right)

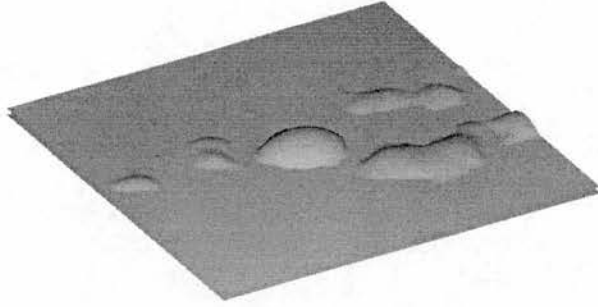


Figure 4.57: Pressure isosurface $p = 343.1\text{Nm}^{-2}$

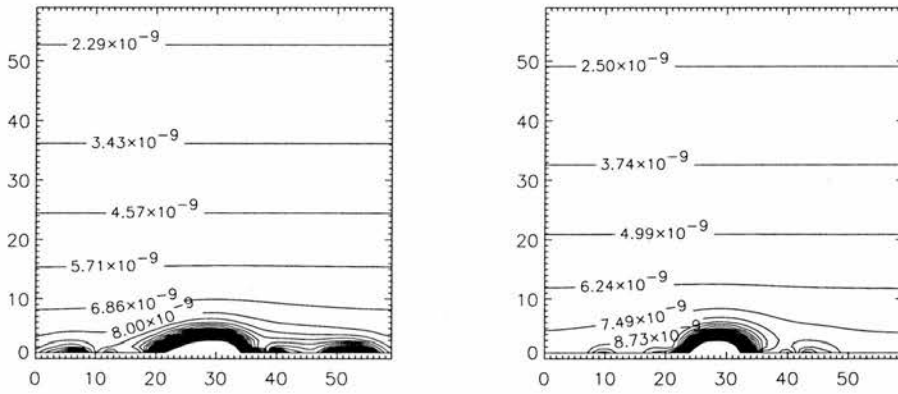


Figure 4.58: Density variation in planes $y = \text{const}$ (left) and $x = \text{const}$ (right)

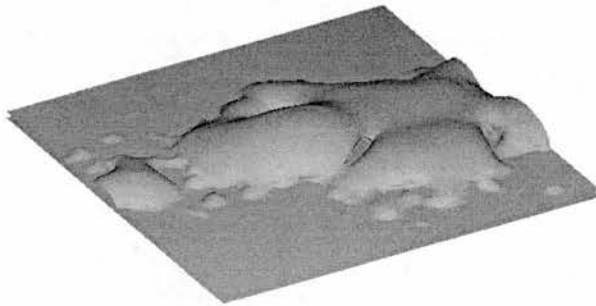


Figure 4.59: Density isosurface $\rho = 9.40 \times 10^{-9}\text{kgm}^{-3}$

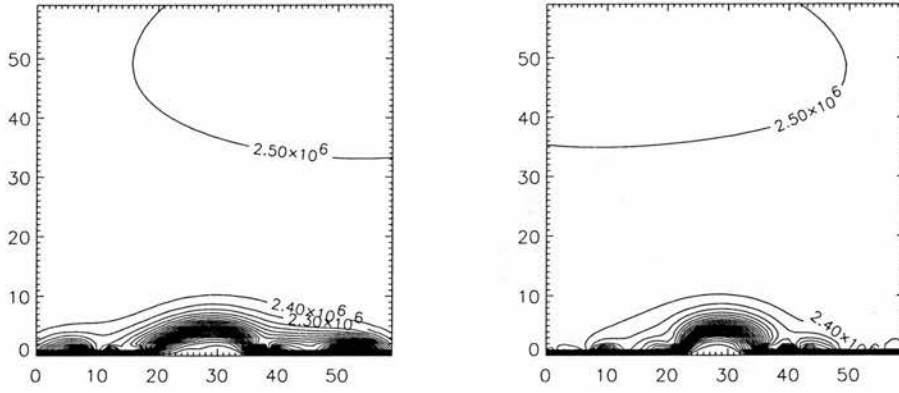


Figure 4.60: Temperature variation in planes $y = \text{const}$ (left) and $x = \text{const}$ (right)

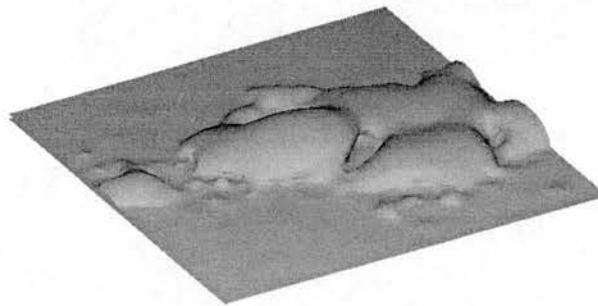


Figure 4.61: Temperature isosurface $T = 1.90 \times 10^6 \text{K}$

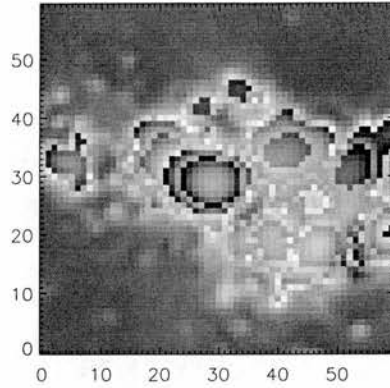


Figure 4.62: Intensity image artificially generated from calculated plasma arrays. Temperature range $1.3 - 2.5 \times 10^6 \text{K}$

Figures 4.56-4.62 show how the non-force-free extrapolated magnetic field structures the plasma. The background plasma model is as in the previous section. In the presence of the non-force-free magnetic field the plasma pressure, density and temperature become three-dimensional, and we represent them graphically by generating contour plots of sections of the pressure, density and temperature data cubes (Figures 4.56, 4.58 and 4.60), where the sections are shown in Figure 4.55. Figure 4.56 shows a large local pressure maximum at the centre of the region above the large flux patch while Figure 4.57 shows other local maxima corresponding to regions dotted with flux, particularly on the right half of the magnetogram Figure 4.49 (right). Figure 4.58 shows that the density has a larger maximum at the centre of the region with some smaller high-density regions further away from the centre, mostly towards the right of the region (i.e. large x). Figure 4.59 shows that the density profile has two arms as does the sigmoid structure of Figure 4.49 (left), although the correspondence of the density isosurface to the SXT image is not perfect. Because of the horizontal near-uniformity of the plasma pressure, the temperature plots in Figures 4.60 and 4.61 are very similar to the density plots of 4.58 and 4.59.

Figure 4.62 shows a synthetic plasma emission pattern generated from the density and temperature profiles of our sigmoid model using Equation (4.12). The minimum

temperature cutoff is $1.3 \times 10^6 \text{K}$ and the maximum cutoff $2.5 \times 10^6 \text{K}$. The pattern shows that emission is restricted approximately to where the sigmoid structure is visible in the SXT image of Figure 4.49 (left) although the sigmoid shape is not reproduced in the intensity image. Using a higher minimum cutoff temperature more appropriate for modelling X-ray structures causes the image to reverse, i.e. we obtain a dark structure in bright surroundings. This is because most of the sigmoid model is cooler than its atmosphere. The density and temperature profile of a real sigmoid structure are not as yet known. Our model, calculated using a negative value for ξ_0 , gives a structure cooler and denser than its surrounding atmosphere. A satisfactory model with a positive value for ξ_0 cannot be obtained without negative densities appearing. It is hoped that such a model will be possible on applying a more versatile method using the exponential- ξ Green's function Equations (3.75-3.77) where we expect larger values of ξ_0 to be possible without the plasma pressure, density or temperature becoming unphysical. Alternatively, assuming an even higher ambient coronal temperature would yield a higher temperature profile and therefore a reasonable intensity image for higher temperature cutoff values.

4.8 Intense flux tube

In every application of our extrapolation attempted so far, the most satisfactory results have been found using a negative value for the non-force-free parameter ξ_0 . This has the effect that, from Equation (4.5), the gas pressure must be greater in a region of high magnetic field strength than in a region of low strength. In the case of intense magnetic flux tubes, however, the gas pressure is believed to be relatively low where the field strength is high, approximately according to the relation

$$p_i + \frac{|\mathbf{B}|^2}{2\mu_0} = p_o \quad (4.13)$$

where p_i and p_o are the pressure values inside and outside the tube respectively. This could only be achieved with our method by using a positive value for ξ_0 (see Equation (4.5), which we attempt to do in this section.

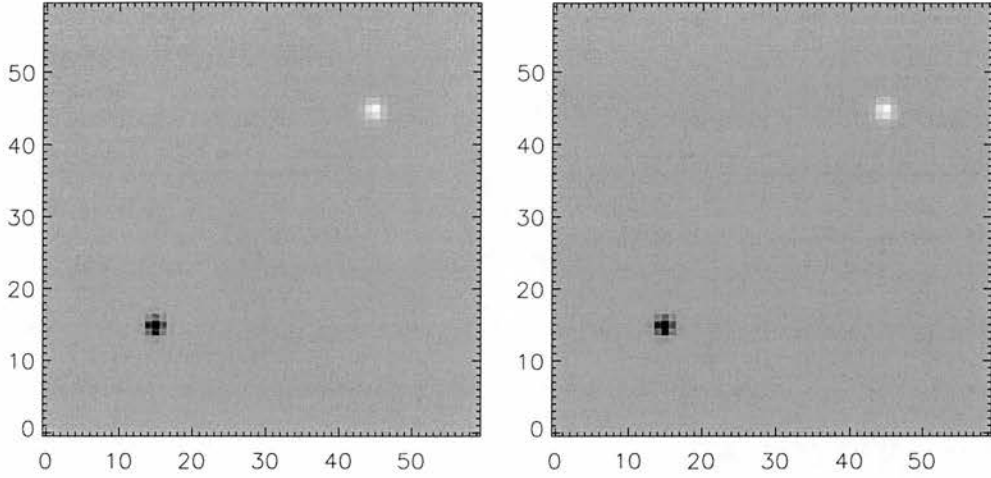


Figure 4.63: Synthetic flux-element magnetogram (left) and fitted Green's function boundary profile (right)

We simulate intense magnetic flux tube footprints by forming a magnetogram of zero flux except for two concentrated spots of intense magnetic flux, one negative and one positive, whose field strength profiles are two-dimensional Gaussians. We generate these Gaussians using formulae of the form

$$B_{z0} = B_z^{max} \exp\left(-\frac{r^2}{l^2}\right) \quad (4.14)$$

where $r^2 = (x-x_0)^2 + (y-y_0)^2$. In the example we take $B_z^{max} = \pm 1000\text{G}$ and $l = 1\text{Mm}$. The resulting “magnetogram” is shown in Figure 4.63 (left panel). We extrapolate the coronal atmosphere using our method with $\alpha = 0$ and ξ_0 as large as possible without the density becoming negative at some point, $\xi_0 = 0.002$. We have already seen in Sections 4.5, 4.6 and 4.7 that a negative value of ξ_0 generally results in a structure cooler and denser than the background model. Here with a positive value for ξ_0 , necessary for a drop in pressure inside the flux tube, we expect the tube to be hotter and less dense than the background model. However, in the corona the background density is so small that it takes only a small value of ξ_0 for negative densities to appear. We have to be satisfied for the moment with our very small value $\xi_0 = 0.002$. The boundary profile of the resulting solution is shown in Figure 4.63 (right panel).

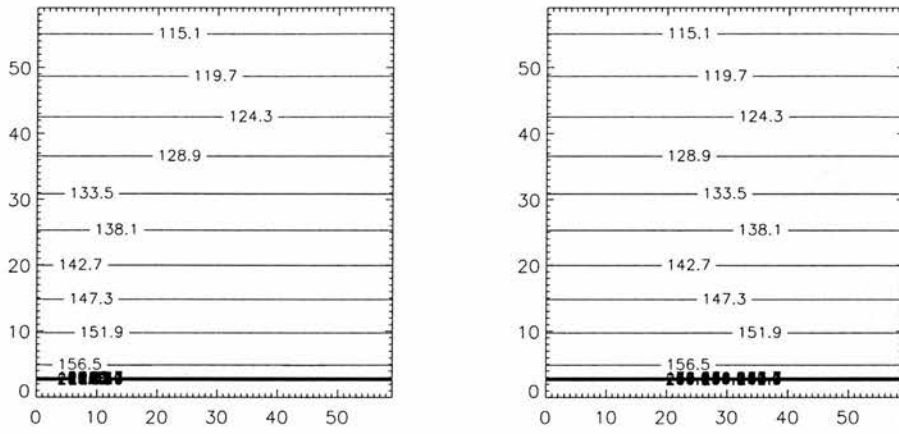


Figure 4.64: Pressure variation in planes $y = \text{const}$ (left) and $x = \text{const}$ (right)

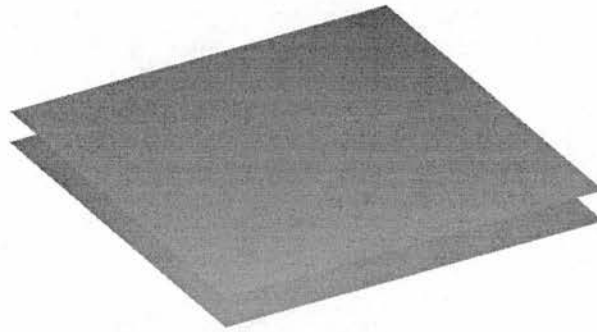


Figure 4.65: Pressure isosurface $p = 156.5 \text{ Nm}^{-2}$

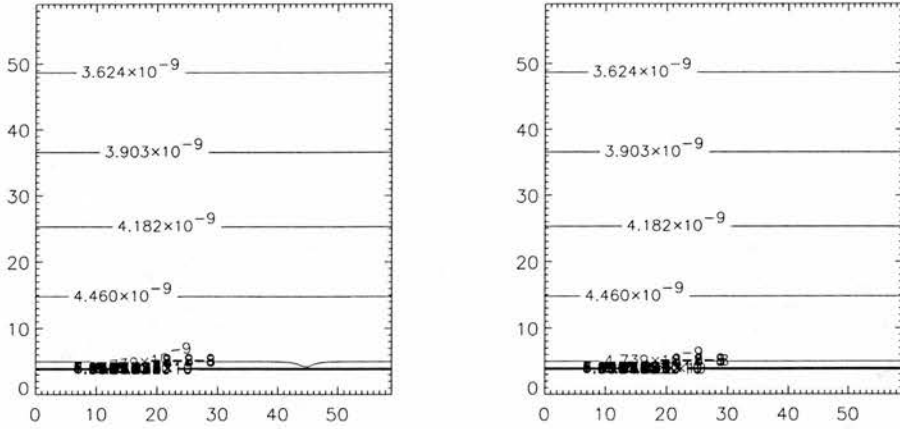


Figure 4.66: Density variation in planes $y = const$ (left) and $x = const$ (right)

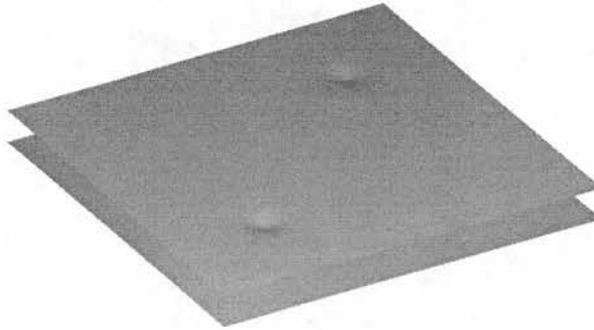


Figure 4.67: Density isosurface $\rho = 4.740 \times 10^{-9} \text{kgm}^{-3}$

Not surprisingly given the very small value for ξ_0 used, Figures 4.64 and 4.65 show that the gas pressure is not significantly different from the background - a very disappointing but inevitable result. As anticipated, Figures 4.66 and 4.67 show that the density is less in regions of strong magnetic field than elsewhere while Figures 4.68 and 4.69 show that the temperature is higher in regions of strong magnetic field than elsewhere although here as in the pressure profile the non-force-free effects are much weaker than in the models of Sections 4.5, 4.6 and 4.7.

Our main hope for this model, like other models in this chapter, is that on adopting the exponential- ξ Green's function of Equations (3.75-3.77) we will be able to concentrate the non-force-free effects close to the photosphere so that a hotter, less dense flux

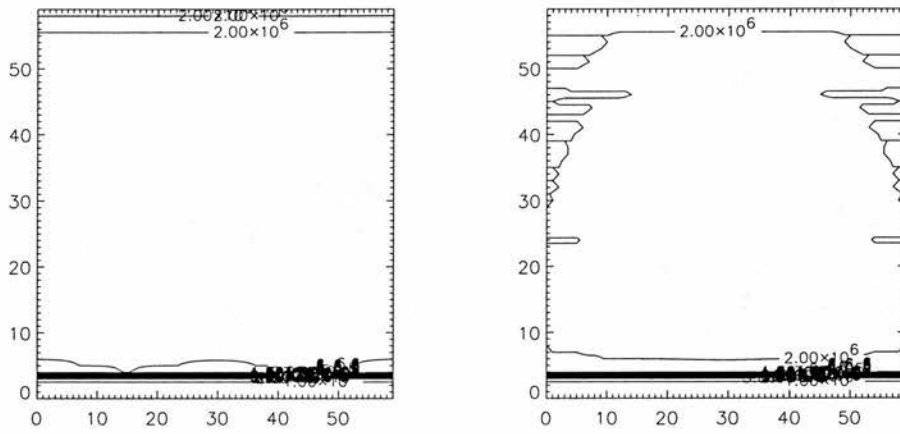


Figure 4.68: Temperature variation in planes $y = \text{const}$ (left) and $x = \text{const}$ (right)

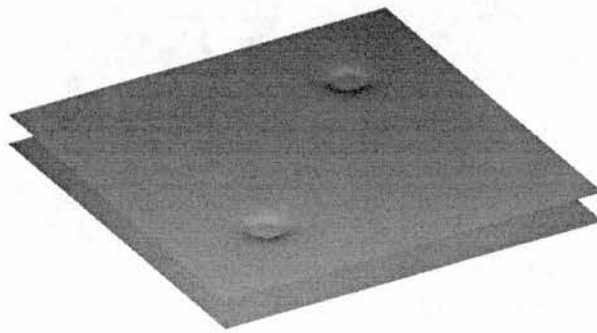


Figure 4.69: Temperature isosurface $T = 1.98 \times 10^6$ K

tube will be possible without unwanted non-force-free effects in the corona causing the density to become unphysical. Because of the complicated nature of the Green's function described in Subsection 3.5.3 and the possible difficulties in implementing a method using this function, this work is beyond the scope of this thesis.

4.9 Discussion

We have implemented the constant- ξ non-force-free Green's function method of Chapter 3 to some genuine observed magnetograms and we have described the resulting solutions for coronal magnetic field and plasma structure in comparison with existing extrapolated magnetic field solutions and any near-simultaneous observed plasma emission patterns available. It is unrealistic to expect a static solution with a restricted current structure to give a detailed reconstruction of the physics of such a complicated system as the solar atmosphere, and the mixed success of the extrapolated solutions in imitating observation is not surprising but encouraging. In the coronal bright point and sigmoid-like examples there was a macroscopic resemblance between a density profile or simulated intensity profile and its corresponding observed emission pattern, while our field line extrapolation produced results very much like those given by other authors working on the same data sets (see Brown, 1999; Gibson URL). In the example of the region with the filament such a resemblance was not possible because the only observed emission pattern is $H\alpha$ and our magnetohydrostatic equilibria are not adequate for modelling the complicated physical processes of filament formation and other structural features observable in $H\alpha$. We were, however, able to find evidence of a changing relationship among the major regions of flux over the period 22-25 July 1979 in broad agreement with Mackay et al. (1997). This was to be found in both the changed structure of the plasma parameter plots and differences in connectivity in the field line plots.

It is significant, however, that relatively successful reconstructions were only possible for negative values of the non-force-free parameter ξ_0 , so that in regions of strong magnetic field the gas pressure is higher than the background according to Equation (4.5). This means that the possibility of using the method to model a structure such

as an intense flux tube where the gas pressure is believed to be significantly lower than background in regions of strong field is very limited, as is illustrated above.

The situation may be improved by increasing the magnetic field-plasma interaction near the photosphere by increasing the value of ξ there. This is impossible at present without ρ becoming negative but a possible solution may be to try the more sophisticated Green's function with $\xi(z) = ae^{-\kappa z}$ (see Chapter 3). This Green's function method is more difficult to implement but in principle possible, the most difficult obstacle to overcome being the numerical calculation of the Green's function components Equations (3.75-3.77). However, any inaccuracy of the reconstructed solar atmosphere compared to the observed emission pattern could be due to an unacknowledged time-dependence of the system. Even if a system seems to be evolving slowly, time-dependent effects may still be significant. Another possible cause of inaccuracy is the special form of Ampère's Law which we assume for practical reasons without physical justification. For slowly-evolving highly-structured systems, we hope that the method gives a fair description and offers a useful alternative to the extrapolation methods currently in use.

Chapter 5

Conclusion

In this thesis analytical methods are used to solve the magnetohydrodynamic equations and the resulting solutions are used to give simple steady or static qualitative models of the macroscopic structure of some magnetic features in the solar atmosphere including a steady flow model of Evershed flow in the fluted penumbra of a sunspot, steady flows in coronal loops and arcades, a solar coronal bright point, a sigmoid-like structure and a filament in the low corona. Although these models cannot be described as physically rigorous, it is clear that analytical solutions of the MHD equations have been applied to modelling the solar atmosphere with a flexibility not seen before. Chapter 2 describes new classes of three-dimensional MHD equilibria with steady field-aligned incompressible flow which model sunspots, coronal loops and arcades more adequately than has been possible with MHD equilibria in the past. Chapter 3 describes a new method for applying a well-known class of three-dimensional MHS equilibria to solving Cartesian photospheric boundary value problems in solar physics and Chapter 4 demonstrates that this method is readily applicable to magnetogram data and that the resulting magnetohydrostatic structures do bear comparison with observed emission patterns, albeit in an approximate manner. These results are striking in view of the fact that Parker (1979) proved that three-dimensional equilibria do not exist (see Parker, 1979, Chapter 14). Although this proof assumed a domain consisting of all of R^3 and finiteness everywhere, assumptions not used in calculating the equilibria discussed in this thesis, three-dimensional equilibrium research was believed to be of very limited use

and the weight of equilibrium research was concentrated on symmetric equilibria for some time.

Recently, however, progress has been steady and there is cause to believe that this situation will continue. There are clear weaknesses in the models presented in this thesis, many of which derive from the assumptions we made towards simplifying the mathematics and making analytical progress possible. Some of these are being examined closely in the hope that certain assumptions can be relaxed without putting analytical treatment of the problem out of our reach. Relaxing the time-independent assumption, for example, is not a viable prospect in the near future because of the mathematical complications that would ensue, but certain other limitations may be easier to address. In the case of the equilibria given in Chapter 2, work is under way to try to include gravity and compressible flow. Hope for progress here is based on an extension from two-dimensional equilibria with incompressible flow to such equilibria with compressible flow achieved by Webb et al. (1994) based on an analogy between field-aligned compressible MHD flows and compressible irrotational steady flow in ordinary fluid dynamics. The plan is to translate this extension to our three-dimensional situation as far as possible and to calculate three-dimensional MHD equilibria with compressible flow. Referring now to the Green's function method of Chapter 3 the most immediate improvement we can implement is a switch from the Green's function used throughout the example sections of Chapters 3 and 4 where the free function $\xi(z)$ is assumed to be constant to the more sophisticated Green's function of Subsection 3.5.3. This will entail substituting the Green's function expressions (3.75-3.77) for (3.66-3.68), the main obstacle being the integration of some non-standard Bessel functions. With this adjustment will come greater flexibility in the possible interaction between the magnetic field and the plasma via $\xi(z)$. A stronger coupling will be possible near the photosphere along with a consistent near-force-free description of the upper corona. If the code can be run on a more powerful machine than those used at present then the method could be implemented at a higher resolution, perhaps at the resolution of the original magnetograms (one pixel per arcsecond or better) and more detailed calculated plasma structures may be possible. The limitations inevitably deriving from our special choice for the form of Ampère's Law (3.4) probably cannot be overcome without tackling the

problem numerically from the outset and until such a numerical treatment is carried out we will not know how limiting this assumption is to the success of the method. Having made the method as effective and flexible as possible within this limitation we intend to apply it in gaining physical insight into features the solar atmosphere recorded as magnetogram data and to present MHS models of these features.

A further possible extension to the work is to investigate the stability properties of the equilibria in this thesis. An attempt at this was made for the static case of one of the equilibria of Chapter 2, borrowing from the successful investigation of a different three-dimensional MHS equilibrium by Chou et al. (1993) (despite mathematical errors) and by Longbottom et al. (1994) using a general technique by Longbottom et al. (1993). Although some progress has been achieved, this work suggests that an analytical treatment using an energy method may be intractable, but further simplifications to the energy integral would increase the likelihood of success and generalising to the steady incompressible flow case is possible using an appropriate energy method (see e.g. Hameiri, 1998). Alternatively a numerical approach may be an option, and perhaps such a treatment could be extended to the equilibria of Chapters 3 and 4 and their successors.

Appendix A

Extensions to the Transformation Method

A.1 Transforming from static 3D MHD without gravity to 3D MHD with steady field-aligned incompressible flow and gravity

For MHD with steady field-aligned incompressible flow the momentum balance equation

$$\rho(\mathbf{v} \cdot \nabla)\mathbf{v} = -\nabla p + \mathbf{j} \times \mathbf{B} - \rho \nabla \psi, \quad (\text{A.1})$$

where ψ is the gravitational potential, can be written with $\mathbf{B} = \nabla\alpha \times \nabla\beta$ exactly as Equations (2.22) except that here $\Pi = p + \frac{1}{2}\rho v^2 + \rho\psi$. In this scheme the flow problem with gravity is described by two equations in the $\nabla\alpha - \nabla\beta$ plane. The effect of $\nabla\psi$, which is in general linearly independent of $\nabla\alpha$ and $\nabla\beta$ has been absorbed into $\nabla\Pi$, which is perpendicular to $\nabla\alpha \times \nabla\beta$ as in the no-gravity flow problem. We can perform the transformation from the static Equations (2.4-2.6) by identifying Equation (2.4)'s gas pressure function Π with $\Pi = p + \frac{1}{2}\rho v^2 + \rho\psi$ and distributing this Π among p , $\frac{1}{2}\rho v^2$ and $\rho\psi$ bearing in mind the constraints $\rho = \rho(\alpha, \beta)$, $\mathbf{v} = \sigma(\alpha, \beta)\mathbf{B}$ and $\nabla\psi$ is a uniform gravitational field. The presence of the $\rho\psi$ term in Π requires us to borrow from p to

compensate.

A.2 Transforming from static 3D MHD with gravity to 3D MHD with steady incompressible field-aligned flow and gravity

The equations of MHD with steady incompressible field-aligned incompressible flow and gravity can be written as

$$\begin{aligned}
(1 - M^2)\nabla\beta \cdot \nabla \times (\nabla\alpha \times \nabla\beta) \\
-\frac{1}{2}\frac{\partial}{\partial\alpha}(1 - M^2)|\nabla\alpha \times \nabla\beta|^2 &= \mu_0 \left(\frac{\partial(\Pi + \rho\psi)}{\partial\alpha} \right)_{\beta,\psi} \\
(1 - M^2)\nabla\alpha \cdot \nabla \times (\nabla\alpha \times \nabla\beta) \\
+\frac{1}{2}\frac{\partial}{\partial\beta}(1 - M^2)|\nabla\alpha \times \nabla\beta|^2 &= -\mu_0 \left(\frac{\partial(\Pi + \rho\psi)}{\partial\beta} \right)_{\alpha,\psi} \\
\left(\frac{\partial\Pi}{\partial\psi} \right)_{\alpha,\beta} &= -\rho.
\end{aligned} \tag{A.2}$$

resolved in the $\nabla\alpha$, $\nabla\beta$ and $\nabla\psi$ directions respectively. The $\nabla\psi$ -component of Equation (A.2) with $\rho = \rho(\alpha, \beta)$ has solution

$$\Pi(\alpha, \beta, \psi) = -\rho(\alpha, \beta)\psi + \Pi_0(\alpha, \beta) \tag{A.3}$$

so that in the right-hand-sides of the $\nabla\alpha$ - and $\nabla\beta$ -components of Equation (A.2), $\Pi + \rho\psi = \Pi_0(\alpha, \beta)$.

The equations of static MHD with gravity can be written as

$$\begin{aligned}
& ([f, g]_{a,b})^2 \nabla b \cdot \nabla \times (\nabla a \times \nabla b) \\
& - \frac{1}{2} \frac{\partial}{\partial a} ([f, g]_{a,b})^2 (\nabla a \times \nabla b)^2 = \mu_0 \left(\frac{\partial(p + \rho\psi)}{\partial a} \right)_{b,\psi} \\
& ([f, g]_{a,b})^2 \nabla a \cdot \nabla \times (\nabla a \times \nabla b) \\
& + \frac{1}{2} \frac{\partial}{\partial b} ([f, g]_{a,b})^2 (\nabla a \times \nabla b)^2 = -\mu_0 \left(\frac{\partial(p + \rho\psi)}{\partial b} \right)_{a,\psi} \tag{A.4} \\
& \left(\frac{\partial p}{\partial \psi} \right)_{a,b} = -\rho.
\end{aligned}$$

By solving the $\nabla\psi$ -component of Equation (A.4), we can write $p + \rho\psi = p_0(\alpha, \beta)$ in the right-hand-sides of the $\nabla\alpha$ - and $\nabla\beta$ -components of Equation (A.4).

Thus the two sets of Equations (A.2) and (A.4) become two pairs of equations just as in Section 2.3 so that a steady MHD solution with incompressible field-aligned flow can be found using a known MHS solution by identifying the quantities

$$[f, g]_{\alpha,\beta} = \sqrt{1 - M^2(\alpha, \beta)} \tag{A.5}$$

and this time

$$\Pi_0(\alpha(\mathbf{x}), \beta(\mathbf{x})) = p_0[f(\alpha(\mathbf{x}), \beta(\mathbf{x})), g(\alpha(\mathbf{x}), \beta(\mathbf{x}))]. \tag{A.6}$$

We do not apply this transformation here because equilibria of this form could not be found.

Appendix B

Textbook Green's Function Method for the Linear Force-free Case

We include this approach here to show that standard textbook Green's function method is equivalent to the non-standard approach based on the P -representation where both are applicable. The z -component of curl of Ampère's law is Helmholtz's equation

$$\Delta B_z + \alpha^2 B_z = 0 \quad (\text{B.1})$$

We follow the established Green's function theory for Helmholtz's equation as described in Morse & Feshbach (1953), Vol. 2. The Green's function G_z for the homogeneous Helmholtz equation for B_z with (e.g.) Dirichlet boundary conditions satisfies the equation

$$\Delta G_z(\mathbf{r}, \mathbf{r}') + \alpha^2 G_z(\mathbf{r}, \mathbf{r}') = -\delta(\mathbf{r} - \mathbf{r}') \quad (\text{B.2})$$

for a unit point source at \mathbf{r}' with homogeneous boundary conditions. Exchanging the roles of \mathbf{r} and \mathbf{r}' , Equation (B.1) $\times G_z(\mathbf{r}, \mathbf{r}')$ – Equation (B.2) $\times B_z$ is

$$G_z(\mathbf{r}', \mathbf{r})\Delta' B_z(\mathbf{r}') - B_z(\mathbf{r}')\Delta' G_z(\mathbf{r}', \mathbf{r}) = B_z(\mathbf{r}')\delta(\mathbf{r} - \mathbf{r}') \quad (\text{B.3})$$

where Δ' is over the source coordinates. Integration over $d\mathbf{r}'$ gives

$$B_z(\mathbf{r}) = \int G_z(\mathbf{r}, \mathbf{r}')\Delta' B_z(\mathbf{r}') - B_z(\mathbf{r}')\Delta' G_z(\mathbf{r}, \mathbf{r}')d\mathbf{r}' \quad (\text{B.4})$$

$$= \int G_z(\mathbf{r}, \mathbf{r}')\nabla' B_z(\mathbf{r}') - B_z(\mathbf{r}')\nabla' G_z(\mathbf{r}, \mathbf{r}') \cdot d\mathbf{n} \quad (\text{B.5})$$

by Green's theorem, where $d\mathbf{n}$ is the surface element. We follow Chui & Hilton (1977) and Lothian & Browning (1995) in assuming that $\nabla' B_z \cdot \mathbf{n} = 0$ and use the solution

$$B_z(\mathbf{r}) = - \int B_z(\mathbf{r}')\nabla' G_z(\mathbf{r}, \mathbf{r}') \cdot d\mathbf{n} \quad (\text{B.6})$$

which puts a layer of sources on the surface. Fourier transforming Equation (B.1) we obtain

$$(\alpha^2 + k^2)\tilde{G}_z(\mathbf{k}, \mathbf{r}') = -e^{i\mathbf{k}\cdot\mathbf{r}'} \quad (\text{B.7})$$

where $\mathbf{k} = (k_x, k_y, k_z)$, which gives on performing the inverse Fourier transform

$$\begin{aligned} G_z(\mathbf{r}, \mathbf{r}') &= \int \frac{e^{-i\mathbf{k}\cdot(\mathbf{r}-\mathbf{r}')}}{\alpha^2 - k^2} d\mathbf{k} \\ &= \int \frac{e^{-ikr \cos \gamma}}{\alpha^2 - k^2} kr \sin \gamma dk d\gamma d\phi_N \end{aligned} \quad (\text{B.8})$$

where $k = |\mathbf{k}|$ and $r = |\mathbf{r} - \mathbf{r}'|$. After integrating out the angles and calculating a complex integral we obtain

$$G_z(\mathbf{r}, \mathbf{r}') = g_z(r) = \frac{\cos(\alpha r)}{r} \quad (\text{B.9})$$

Solving for the homogeneous solution of Eq. (B.7) assuming that $G_z(\mathbf{r}, \mathbf{r}') = g_z(r)$ we have

$$g_z''(r) + \frac{2}{r}g_z'(r) + \alpha^2 g_z(r) = 0. \quad (\text{B.10})$$

The transformation $h(r) = \sqrt{r}g_z(r)$ gives a Bessel equation with general solution $h(r) = aJ_{\frac{1}{2}}(\alpha r) + bJ_{-\frac{1}{2}}(\alpha r)$, i.e.

$$g_z = \frac{a' \cos \alpha r}{r} + \frac{b' \sin \alpha r}{r} \quad (\text{B.11})$$

but from Eq. (B.9) only $\frac{\cos(\alpha r)}{r}$ gives the desired delta-function behaviour at $r = |\mathbf{r} - \mathbf{r}'| = 0$. The second term of Eq. (B.11) corresponds to the complementary Green's function described by Chui & Hilton (1977) and has no contribution to the magnetic field at $z = 0$. We therefore do not have sufficient observational data to determine b' uniquely, e.g. horizontal magnetic field components on the boundary, and so we follow Chui & Hilton (1977) and concentrate on the first term of Eq. (B.11) with $a' = 1$. Taking $G_z(\mathbf{r}, \mathbf{r}') = \frac{\cos(\alpha r)}{r}$ we get

$$\begin{aligned} B_z(x, y, z) &= - \int_{z=0} B_z(\mathbf{r}') \nabla' G_z(\mathbf{r}, \mathbf{r}') \cdot d\mathbf{n} \\ &= \int_{z=0} \frac{\partial G_z}{\partial z}(x, y, z, x', y', 0) B_z(x', y', 0) dx' dy' \end{aligned}$$

where

$$\frac{\partial G_z}{\partial z} = \left(\frac{\alpha}{r} \sin(\alpha r) + \frac{1}{r^2} \cos(\alpha r) \right) \frac{z}{r} \quad (\text{B.12})$$

This is of the same form as Eq. (3.58) but with $(\mathbf{n} \cdot \nabla) \mathbf{G}$ playing the role of \mathbf{G} . Note that the point-source solution Equation (B.9) is spherically symmetric until we include the Cartesian half-space boundary condition giving Equation (B.12).

It remains to calculate B_x and B_y , and here it is most convenient to fall back on the P -representation of the field. Recalling the structure of the Green's function Eqs. (3.47-3.49), we need

$$\frac{\partial}{\partial R}(R\bar{\Gamma}) = -R\frac{\partial G_z}{\partial z} \quad (\text{B.13})$$

giving for $\bar{\Gamma}$ on applying Eq. (3.29)

$$\bar{\Gamma} = \frac{z}{Rr} \cos(\alpha r) - \frac{1}{R} \cos(\alpha z). \quad (\text{B.14})$$

We have recovered Chui & Hilton's solution for \mathbf{B} , complete with its “ P ”-structure without assuming it at the beginning.

Bibliography

- [1] Agim, Y.Z. & Tataronis, J.A. "General Two-Dimensional Magnetohydrodynamic Equilibria with Mass Flow" *J. Plasma Phys.* **34** 337 (1985)
- [2] Alissandrakis, C.E. "On the Computation of Constant- α Force-free Magnetic Field", *Astron. Astrophys.* **100**, 197 (1981)
- [3] Altschuler, M.D. and Newkirk, G.Jr. "Magnetic Fields and the Structure of the Solar Corona", *Solar Phys.* **9**, 131 (1969)
- [4] Altschuler M.D., Trotter D.E., Newkirk G., Howard R. "The Large-scale Solar Magnetic Field", *Solar Phys.* **39**, 3 (1974)
- [5] Altschuler M.D., Levine R.H., Stix M. & Harvey J. "High Resolution Mapping of the Magnetic Field of the Solar Corona", *Solar Phys.* **51**, 345 (1977)
- [6] Aly, J.J. "On the Reconstruction of the Nonlinear Force-free Coronal Magnetic Field from Boundary Data", *Solar Phys.* **120**, 19 (1989)
- [7] Amari, T. & Démoulin, P. 1992, in Proceedings of Workshop "Méthodes de Détermination des Champs Magnétiques Solaires et Stellaires", Observatoire de Paris, p. 187
- [8] Amari, T., Aly, J.J., Luciani, J.F., Boulmezaoud, T.Z. & Mikic, Z. "Reconstructing the Solar Coronal Magnetic Field as a Force-free Magnetic Field", *Solar Phys.* **174**, 129 (1997)
- [9] Amari, T., Boulmezaoud, T.Z. & Mikic, Z. "An Iterative Method for the Reconstruction of the Solar Coronal Magnetic Field", *Astron. Astrophys.* **350**, 1051 (1999)

- [10] Aulanier, G., Démoulin, P., Schmeider, B., Fang, C. & Tang, Y.H. “Magnetohydrostatic Model of a Bald-patch Flare”, *Solar Phys.* **183**, 369 (1998)
- [11] Aulanier, G., Démoulin, P., van Driel-Gesztelyi, L., Mein, P. & DeForest, C. “3-D Magnetic Configurations Supporting Prominences”, *Astron. Astrophys.* **342**, 864 (1999)
- [12] Bagenal, F. & Gibson, S. “Modeling the Large-scale Structure of the Solar Corona”, *J. Geophys. Res.* **96**, 17663 (1991)
- [13] Balescu, R. “Plasma Transport Theory” Vol. 1, North-Holland (1988)
- [14] Barbosa, D.D. “Linear Force-free Fields in the Lower Corona”, *Solar Phys.* **56**, 55 (1977)
- [15] Beckers, J.M. & Schröter, E.M. “The Intensity, Velocity and Magnetic Structure of a Sunspot Region IV: Properties of a Unipolar Sunspot” *Solar Phys.* **10**, 384 (1969)
- [16] Birn, J. “Quasi-steady Current Sheet Structures with Field-aligned Flow” *J. Geophys. Res.* **97**, 16817 (1992)
- [17] Bogdan, T.J. & Low, B.C. “Three-dimensional Structures of Magnetic Atmospheres. II. Modeling the Large-scale Corona”, *Astrophys. J.* **306**, 271 (1986)
- [18] Bray, R.J., Cram, L.E., Durrant, C.J. & Loughhead, R.E. *Plasma Loops in the Solar Corona*, Cambridge UP, Cambridge (1991)
- [19] Bray, R.J. & Loughhead, R.E. *Sunspots*, Chapman and Hall, London (1964)
- [20] Brekke, P., Kjeldseth-Moe, O. & Harrison, R.A. “High-velocity Flows in an Active Region Loop System Observed with the Coronal Diagnostic Spectrometer (CDS)” *Solar Phys.* **175**, 511 (1997)
- [21] Brown, D.S. “Three-dimensional Topology of Solar Coronal Magnetic Fields”, Ph.D. Thesis, University of St. Andrews (1999)
- [22] Chandrasekhar, S. *Hydrodynamic and Hydromagnetic Stability*, Oxford UP, Oxford, 157 (1961)

- [23] Chou, Y.P., Low, B.C. & Bhattacharjee, A. "A Class of Three-dimensional Laminated Equilibria and their Stability" *Ap.J.* **416**, 379 (1993)
- [24] Chiu, Y.T. & Hilton, H.H. "Exact Green's Function Method of Solar Force-free Magnetic-field Computations with Constant α ", *Astrophys. J.* **212**, 873 (1977)
- [25] Degenhardt, D. & Wiehr, E. "Spatial Variation of the Magnetic Field Inclination in a Sunspot Penumbra" *Astron. Astrophys.* **252**, 821 (1991)
- [26] Del Zanna, L. & Chiuderi, C. "Exact Solutions for Symmetric Magnetohydrodynamic Equilibria with Mass Flow" *Astron. Astrophys.* **310**, 341 (1996)
- [27] Démoulin, P., Hénoux, J.C., Mandrini, C.H., Priest, E.R. "Can We Extrapolate a Magnetic Field when its Topology is Complex?", *Solar Phys.* **174**, 73 (1997)
- [28] de Ville, A. & Priest, E.R. "Steady Flows in Solar Magnetic Structures - A Class of Exact MHD Solutions" *Geophys. Astrophys. Fluid Dyn.* **59**, 253 (1991a)
- [29] de Ville, A. & Priest, E.R. "Steady Flows in Magnetic Arcades - A Class of Exact MHD Solutions" *Geophys. Astrophys. Fluid Dyn.* **61**, 225 (1991b)
- [30] Evershed, G.E. "Radial Movement in Sun-spots" *MNRAS* **69**, 454 (1909)
- [31] Finn, J.M., Guzdar, P.N. & Usikov, D. "Three-dimensional Force-free Looplike Magnetohydrodynamic Equilibria" *Astrophys. J.* **427**, 475 (1994)
- [32] Fleck, B. "First Results from SoHO" *Rev. Mod. Astron.* **10**, 273 (1997)
- [33] Gary, G.A. "Linear Force-free Magnetic Fields for Solar Extrapolation and Interpretation", *Astrophys. J. Supp.* **69**, 323 (1989)
- [34] Gary, G.A. "Rendering Three-dimensional Solar Coronal Structures", *Solar Phys.* **174**, 241 (1997)
- [35] Gary, G.A. & Alexander, D. "Constructing the Coronal Magnetic Field by Correlating Parametrized Magnetic Field Lines with Observed Coronal Plasma Structures", *Solar Phys.* **186**, 123 (1999)
- [36] Gebhardt, U. & Kiessling, M. "The Structure of Ideal Magnetohydrodynamics with Incompressible Steady Flow" *Phys. Fluids* **B4**, 1689 (1992)

- [37] Gibson, S. www.damtp.cam.ac.uk/user/sg273/WSM3/workshop/workgroup.html
- [38] Gibson, S. & Bagenal, F. "Large-scale Magnetic Field and Density Distribution in the Solar Minimum Corona", *J. Geophys. Res.* **100**, 19865 (1995)
- [39] Goedbloed, J.P. & Lifschitz, A. "Stationary Symmetric Magnetohydrodynamic Flows" *Phys. Plasmas* **4**, 3544 (1997)
- [40] Grad, H. "Reducible Problems in Magneto-fluid Dynamic Steady Flows" *Rev. Mod. Phys.* **32**, 830 (1960)
- [41] Hameiri, E. "Variational Principles for Equilibrium States with Plasma Flow" *Phys. Plasmas* **5**, 3270 (1998)
- [42] Heinemann, M. & Olbert, S. "Axisymmetric Ideal MHD Stellar Wind Flow" *J. Geophys. Res.* **83**, 2457 (1978)
- [43] Hudson, T.S. & Wheatland, M.S. "Topological Differences Between Force-free Field Models" *Solar Phys.* **186**, 301 (1999)
- [44] Hundhausen, J.R. "Coronal Diagnostics (and some Dynamics)" preprint unpublished (1993)
- [45] Imai, I. "On Flows of Conducting Fluids Past Bodies" *Rev. Mod. Phys.* **32**, 992 (1960)
- [46] Kaiser, R. & Salat, A. "New Classes of Three-Dimensional Ideal-MHD Equilibria" *J. Plasma Phys.* **57**, 425. (1997)
- [47] Lee, J., White, S.M., Kundu, M.R., Mikic, Z. & McClymont, A.N. "A Test for Coronal Magnetic Field Extrapolations", *Astrophys. J.* **510**, 413 (1999)
- [48] Lifschitz, A.E. *Magnetohydrodynamics and Spectral Theory*, Kluwer, Dordrecht (1989)
- [49] Lifschitz, A. & Goedbloed, J.P. "Transonic Magnetohydrodynamic Flows" *J. Plasma Phys.* **58**, 101 (1997)

- [50] Lites, B.W., Low, B.C., Martinez Pillet, V., Seagraves, P., Skumanich, A., Frank, Z.A., Shine, R.A. & Tsuneta, S. "The Possible Ascent of a Closed Magnetic System Through the Photosphere", *Astrophys. J.* **446**, 877 (1995)
- [51] Longbottom, A.W., Melville, J.P. & Hood, A.W. "Bounds on the Stability of 3D Magnetic Equilibria in the Solar Corona" *Solar Phys.* **146**, 93 (1993)
- [52] Longbottom, A.W., Melville, J.P. & Hood, A.W. "A Necessary Condition for the Stability of a Class of Three-dimensional Laminated Equilibria" *Astrophys. J.* **423**, 496 (1994)
- [53] Lothian, R.M. & Browning, P.K. "Coronal Magnetic Field Equilibrium with Discrete Flux Sources", *Solar Phys.* **161**, 289 (1995)
- [54] Low, B.C. "Magnetic Atmospheres with Variations in Three Dimensions" *Astrophys. J.* **263**, 952 (1982)
- [55] Low, B.C. "Three-dimensional Magnetostatic Atmospheres: Magnetic Field with Vertically Oriented Tension Force" *Astrophys. J.* **277**, 415 (1984)
- [56] Low, B.C. "Three-dimensional Structures of Magnetic Atmospheres. I. Theory", *Astrophys. J.* **293**, 31 (1985)
- [57] Low, B.C. "On the Hydromagnetic Stability of a Class of Laminated Force-Free Magnetic Fields" *Astrophys. J.* **330**, 992 (1988)
- [58] Low, B.C. "Three-dimensional Structures of Magnetic Atmospheres. III. A General Formulation", *Astrophys. J.* **370**, 427 (1991)
- [59] Low, B.C. "Three-dimensional Structures of Magnetic Atmospheres. IV. Magnetic Structures over a Solar Active Region", *Astrophys. J.* **399**, 300 (1992)
- [60] Low, B.C. "Three-dimensional Structures of Magnetic Atmospheres. V. Coupled Electric Current Systems", *Astrophys. J.* **408**, 689 (1993a)
- [61] Low, B.C. "Three-dimensional Structures of Magnetic Atmospheres. VI. Examples of Coupled Electric Current Systems", *Astrophys. J.* **408**, 693 (1993b)

- [62] Mackay, D.H., Gaizauskas, V., Rickard, G.J. & Priest, E.R. "Force-free and Potential Models of a Filament Channel in which a Filament Forms", *Astrophys. J.* **486**, 534 (1997)
- [63] Martens, P.C.H., Hurlburt, N.E., Title, A.M. & Acton, L.W. "An Analytical Model for Fluted Sunspots and a New Interpretation of Evershed Flow and X-Ray Anenomes" *Astrophys. J.* **463**, 372 (1996)
- [64] McClymont, A.N. & Mikic, Z. "Thickness Variations Along Coronal Loops Inferred from Vector Magnetograph Data", *Astrophys. J.* **422**, 899 (1994)
- [65] McClymont, A.N., Jiao, L. & Mikic, Z. "Problems and Progress in Computing Three-dimensional Coronal Active Region Magnetic Fields from Boundary Data", *Solar Phys.* **174**, 191 (1997)
- [66] Maschke, E.K. & Perrin, H. "Exact Solutions of the Stationary MHD Equations for a Rotating Toroidal Plasma" *Plasma Phys.* **22**, 579 (1980)
- [67] Morse, P.M. & Feshbach, H. *Methods of Theoretical Physics* (2 Vols.), McGraw-Hill, New York (1953)
- [68] Nakagawa, Y. and Raadu, M.A. "On Practical Representation of Magnetic Field", *Solar Phys.* **25**, 127 (1972)
- [69] Neukirch, T. "On Self-Consistent Three-dimensional Analytic Solutions of the Magnetohydrostatic Equations" *Astron. Astrophys.* **301**, 628 (1995)
- [70] Neukirch, T. "Nonlinear Self-consistent Three-dimensional Arcade-like Solutions of the Magnetohydrostatic Equations" *Astron. Astrophys.* **325**, 847 (1997a)
- [71] Neukirch, T. "3D Solar Magnetohydrostatic Structures", *Phys. Chem. Earth* **22**, 405 (1997b)
- [72] Neukirch, T. "Introduction to the Theory of MHD Equilibria" Seminar Notes (1999)
<http://www-solar.mcs.st-andrews.ac.uk/thomas/teaching/mhdlect.ps.gz>
- [73] Neukirch T. & Martens, P.C.H. "An Approximate Self-consistent Theory of the Magnetic Field of Sunspot Penumbrae" *Astron. Astrophys.* **332**, 1075 (1998)

- [74] Neukirch, T. & Rastätter L. "A New Method for Calculating a Special Class of Self-consistent Three-dimensional Magnetohydrostatic equilibria", *Astron. Astrophys.* **348**, 1000 (1999)
- [75] Parker, E.N. *Cosmical Magnetic Fields*, Oxford University Press, England (1979)
- [76] Parnell, C.E., Smith, J.M., Neukirch, T. & Priest, E.R. "The Structure of Three-dimensional Magnetic Neutral Points" *Phys. Plasmas* **3** (3), 759 (1996)
- [77] Petrie, G.J.D. & Neukirch, T. "Self-consistent Three-dimensional Steady-state Solutions of the MHD Equations with Field-aligned Incompressible Flow" *Geophys. Astrophys. Fluid Dyn.* **91**, 269 (1999)
- [78] Petrie, G.J.D. & Neukirch, T. "The Green's Function Method for a Special Class of Linear Three-dimensional Magnetohydrostatic Equilibria" *Astron. Astrophys.* **356**, 735 (2000)
- [79] Priest, E.R. *Solar Magnetohydrodynamics*, D. Reidel Publishing Company, Dordrecht, Holland (1982)
- [80] Roberts, P.H. *An Introduction to Magnetohydrodynamics*, Longmans, London (1967)
- [81] Rimmele, T.R. "On the Temporal Behaviour of the Evershed Effect" *Astron. Astrophys.* **290**, 972 (1994)
- [82] Rimmele, T.R. "Sun Center Observations of the Evershed Effect" *Astrophys. J.* **445**, 511 (1995)
- [83] Rosner, R., Low, B.C., Tsinganos, K. & Berger, M.A. "On The Relationship Between the Topology of Magnetic Field Lines and Flux Surfaces" *Geophys. Astrophys. Fluid Dyn.* **48**, 251 (1989)
- [84] Roumeliotis, G. "The 'Stress-and-relax' Method for Reconstructing the Coronal Magnetic Field from Vector Magnetograph Data", *Astrophys. J.* **473**, 1095 (1996)
- [85] Sakurai, T. "Calculation of Force-Free Magnetic Field with Non Constant Alpha", *Solar Phys.* **69**, 343 (1981)

- [86] Sakurai, T. "Green's Function Methods for Potential Magnetic Fields", *Solar Phys.* **76**, 301 (1982)
- [87] Salat, A. & Kaiser, R. "Three-dimensional Closed Field Line Magnetohydrodynamic Equilibria Without Symmetries" *Phys. Plasmas* **2**, 3777 (1995)
- [88] Schatten, K.H., Wilcox, J.M. & Ness, N.F. "A Model of Interplanetary and Coronal Magnetic Fields", *Solar Phys.* **6**, 442 (1969)
- [89] Schindler, K. & Birn, J. "Magnetospheric Physics", *Physics Reports* **47**, 2 (1978)
- [90] Schindler, K. & Birn, J. "Magnetotail Theory", *Space Science Reviews* **44** 307 (1986)
- [91] Schmidt, H.V. "On the Observable Effects of Magnetic Energy Storage and Release Connected with Solar Flares", in *ASS-NASA Symposium on the Physics of Solar Flares*, ed. W.N. Ness (NASA SP-50), p. 107 (1964)
- [92] Semel, M. "Contribution à l'Etude des Champs Magnétiques dans les Regions Actives Solaires", *Ann. Astrophys.* **30**, 513 (1967)
- [93] Semel, M. "Extrapolation Functions for Constant- α Force-free Fields. Green's Method for the Oblique Boundary Value.", *Astron. Astrophys.* **198**, 293 (1988)
- [94] Shine, R.A., Title, A.M., Tarbell, T.D., Smith, K., Frank, Z.A. & Scharmer, G. "High-resolution Observations of the Evershed Effect in Sunspots" *Astrophys. J.* **430**, 410 (1994)
- [95] Shivamoggi, B.K. "Generalized Magnetohydrostatic Equilibria" *Quart. Appl. Math.* **44**, 487 (1985)
- [96] Solov'ev, L.S. "Symmetric Magnetohydrodynamic Flow and Helical Waves in a Circular Plasma Cylinder" *Rev. Plasma Phys.* **3**, 277 (1967)
- [97] Stanchfield II, D.C., Thomas, J.H. & Lites, B.W. "The Vector Magnetic Field, Evershed Flow, and Intensity in a Sunspot" *Astrophys. J.* **477**, 485 (1997)
- [98] Stern, D.P. "Euler Potentials" *American J. Phys.* **38**, 494 (1970)

- [99] Tasso, H. & Throumoulopoulos, G.N. "Axisymmetric Ideal Magnetohydrodynamic Equilibria with Incompressible Flows" *Phys. Plasmas* **5**, 2378 (1998)
- [100] Thomas J.H. in *Solar and Astrophysical MHD Flows* ed. K.C. Tsinganos, Kluwer, Dordrecht, 39 (1996)
- [101] Throumoulopoulos, G.N. "Nonlinear Axisymmetric Resistive Magnetohydrodynamic Equilibria with Toroidal Flow" *J. Plasma Phys.* **59**, 303 (1998)
- [102] Throumoulopoulos, G.N. & Pantis, G. "Magnetohydrodynamic Equilibria of a Cylindrical plasma with Poloidal Mass Flow and Arbitrary Cross-Sectional Shape" *Plasma Phys. Control. Fusion* **38**, 1817 (1996)
- [103] Throumoulopoulos, G.N. & Tasso, H. "Cylindrical Ideal Magnetohydrodynamic Equilibria with Incompressible Flow" *Phys. Plasmas* **4**, 1492 (1997)
- [104] Title, A.M., Frank, Z.A., Shine, R.A., Tarbell, T.D., Topka, K.P., Scharmer, G & Schmidt, W. "On the Magnetic and Velocity Field Geometry of Simple Sunspots" *Astrophys. J.* **403** 780 (1993)
- [105] Tsinganos, K. (ed.) *Solar and Astrophysical MHD Flows*, Kluwer, Dordrecht (1996)
- [106] Tsinganos, K. & Surlantzis, G. "MHD Equilibria with Flows in Uniform Gravity I. 1-D Prominence- and Arcade-Type Solutions" *Astron. Astrophys.* **259**, 585 (1992)
- [107] Tsinganos, K., Surlantzis, G. & Priest, E.R. "MHD Equilibria with Flows in Uniform Gravity II. A Class of Exact 2-D Loop-like Solutions" *Astron. Astrophys.* **275**, 613 (1993)
- [108] Webb, G.M., Brio, M. & Zank, G.P. "Steady MHD Flows with an Ignorable Coordinate and the Potential Transonic Flow Equation" *J. Plasma Phys.* **52**, 141 (1994)
- [109] Westendorp-Plaza, C., del Toro Iniesta, J.C., Ruiz-Cobo, R. Mart'nez Pillet, V., Lites, B.W. & Skumanich, A. "Evidence for a Downward Mass Flux in the Penumbra Region of a Sunspot" *Nature* **389**, 47 (1997)

- [110] Wheatland, M.S. "A Better Linear Force-free Field", *Astrophys. J.* **518**, 948 (1999)
- [111] Woolley, M.L. "Three-Dimensional Equilibria in the Magnetohydrodynamic Approximation" *J. Plasma Phys.* **15**, 423 (1976)
- [112] Woolley, M.L. "Generalized Elliptic Equilibria in the Magnetohydrodynamic Approximation" *J. Plasma Phys.* **17**, 259 (1977)
- [113] Wu, S.T., Chang, H.M. & Hagyard, M.J. 1985, in *Measurements of Solar magnetic Fields*, ed. M.J. Hagyard (NASA CP-2374), 17
- [114] Zehrfeld, H.P. & Green, B.J. "Stationary Toroidal Equilibria at Finite Beta" *Nucl. Fusion* **12**, 569 (1972)
- [115] Zhao, X. & Hoeksema, J.T. "Unique Determination of Model Coronal Magnetic Fields Using Photospheric Observations" *Solar Phys.* **143**, 41 (1993)
- [116] Zhao, X. & Hoeksema, J.T. "A Coronal Magnetic Field Model with Horizontal Volume and Sheet Currents" *Solar Phys.* **151**, 91 (1994)
- [117] Zwingmann, W. "Quasistationäre Entwicklung und Einsatz eruptiver Prozesse von Plasmastrukturen im Magnetfeld mit Anwendung auf die Sonnenatmosphäre" Dissertation, Ruhr-Universität Bochum (1984)